TU Delft

Delft University of Technology

Ionic electroactive polymer for organs-on-chip applications

Motreuil-Ragot, P.A.

DOI
10.4233/uuid:5f72b863-c05f-4bfb-82e6-b75dc63923cd

Publication date
2023

Document Version
Final published version

Citation (APA)
Motreuil-Ragot, P. A. (2023). *Ionic electroactive polymer for organs-on-chip applications*. [Dissertation (TU Delft), Delft University of Technology]. https://doi.org/10.4233/uuid:5f72b863-c05f-4bfb-82e6-b75dc63923cd

Important note
To cite this publication, please use the final published version (if applicable).
Please check the document version above.

Copyright
Other than for strictly personal use, it is not permitted to download, forward or distribute the text or part of it, without the consent of the author(s) and/or copyright holder(s), unless the work is under an open content license such as Creative Commons.

Takedown policy
Please contact us and provide details if you believe this document breaches copyrights.
We will remove access to the work immediately and investigate your claim.

This work is downloaded from Delft University of Technology.
For technical reasons the number of authors shown on this cover page is limited to a maximum of 10.

Ionic electroactive polymer for organs-on-chip applications

Ionic electroactive polymer for organs-on-chip applications

Proefschrift

ter verkrijging van de graad van doctor
aan de Technische Universiteit Delft,
op gezag van de Rector Magnificus Prof. dr. ir. T.H.J.J. van der Hagen,
voorzitter van het College voor Promoties,
in het openbaar te verdedigen op dinsdag 4 juli 2023 om 12:30 uur

door

Paul Alexandre

MOTREUIL-RAGOT

Master of Science in Micro and Nano electronics,
Strasbourg University, Strasbourg, France,
geboren te Le Mans, France.

Dit proefschrift is goedgekeurd door de

promotor: Prof. dr. ir. P. M. Sarro
copromotor: Dr. M. Mastrangeli

Samenstelling promotiecommissie:

Rector Magnificus,	voorzitter
Prof. dr. ir. P. M. Sarro,	Technische Universiteit Delft
Dr. M. Mastrangeli,	Technische Universiteit Delft

Onafhankelijke leden:

Prof. dr. X. Gidrol,	CEA Grenoble
Prof. dr. ir. M. Odjik,	Technische Universiteit Twente
Dr. P. Boukany,	Technische Universiteit Delft
Prof. dr. P. J. French,	Technische Universiteit Delft
Dr. A. Hunt,	Technische Universiteit Delft
Prof. dr. ir. R. Dekker,	Technische Universiteit Delft, reservelid

Keywords: Ionic polymer metal composite, transducer, microfluidics, organ-on-chip, electroless deposition
Printed by: *Proefschrift specialist*
Front & Back: *Louise Dumeige*

Copyright © 2023 by P. Motreuil Ragot

An electronic version of this dissertation is available at
http://repository.tudelft.nl/.

L'étoile a pleuré rose au coeur de tes oreilles,
L'infini roulé blanc de ta nuque à tes reins ;
La mer a perlé rousse à tes mammes vermeilles
Et l'Homme saigné noir à ton flanc souverain.

Arthur Rimbaud

Contents

Summary

An organ-on-chip (OoC) is a microelectromechanical (MEMS) device that aims to recapitulate in-vitro the physiology of the smallest functional unit of an organ in order to perform drug analysis or study disease models. OoCs are very complex systems that require actuation and sensing capabilities within controlled and delicate environment. The research presented in this thesis focuses on a transductive material that offers promising properties for organ-on-chip. The objective of the thesis is to demonstrate the potential of using ion-based electroactive materials to tackle current OoC limitations. An ionic electroactive material, called ionic polymer metal composite (IPMC) is proposed, characterized and developed in order to increase the ease of use, integrability, and scalability of OoC. The IPMC consists of a soft polymer, doped with ions naturally present in standard culture media, flanked by platinum electrodes on opposite sides. This biocompatible material shows good actuation and sensing capabilities, requires low driving voltage and has been herein investigated as a potential transducer for several organ-on-chip applications. A first version of the IPMC with a thickness of 180 μm (called thick IPMC) showing good actuation capabilities has been adopted to implement a micropump and a tissue stretcher. The cells strecher could exhibit biologically relevant strain (0.1 %) while showing no toxicity, and the micropump achieved biologically relevant wall shear stress (0.008 Pa) through liquid flow within microchannels. Furthermore, in this thesis, this moisture-sensitive material has been investigated in the context of wafer-level process flow using state-of-the-art microfabrication tools to demonstrate its compatibility with silicon-based technology. A second version of the IPMC has been developed based on a thinner polymer (50 μm, called thin IPMC), as well as an adjusted manufacturing recipe in order to explore the material potential as a sensor for OoC. A comparative study has been performed between the manufacturing of thick and thin IPMC, evidencing different dynamics of the electroless deposition reaction depending on the thickness of the polymer used. The developed thin IPMC shows superior sensing capabilities by virtue of lower flexural rigidity and higher electrodes conductivity. The applications explored with the thin IPMC are microfluidics flow sensing and strain sensing. The microfluidic flow sensor exhibits good sensing capabilities with a sensitivity of 4.78 mV/(uL/s) and a linear behavior in the studied range. In addition, soft lithography and patterning of hydrogel have been investigated on top of the thin IPMC, to further assess the material as a smart substrate for tissue engineering. The present thesis anticipates a potentially significant impact of smart materials as a new tool to engineer multi-functional culture substrates for OoC as well as develop electronically-controllable flexible membranes for micro pumping.

Samenvatting

Een orgaanchip, of organ-on-chip (OoC), is een micro-elektromechanisch (MEMS) systeem dat in-vitro de fysiologie van de kleinste functionele eenheid van een orgaan nabootst met als doel het bestuderen en analyseren van medicijnen of pathologische modellen. OoC zijn zeer complexe systemen die bedieningen en detectiemogelijkheden vereisen in een gecontroleerde en delicate omgeving. Het in deze scriptie beschreven onderzoek beschouwt een transductief materiaal dat veelbelovende eigenschappen vertoont voor orgaanchips. Het doel van dit proefschrift is om het potentieel aan te tonen van het gebruik van op ionische gebaseerde elektroactieve materialen om de huidige OoC-beperkingen aan te pakken. Een ionisch elektroactief materiaal, ook wel een ionisch polymeer-metaal composiet genoemd (IPMC) wordt geïntroduceerd, gekarakteriseerd en ontwikkeld met het oog op verbeterde gebruiksvriendelijkheid, integratiemogelijkheid en opschaalbaarheid van OoCs. De composiet bestaat uit een zacht polymeer met daarin ionen die men terugvindt in standaard kweekmedium. Dit polymeer is aan weerszijden omvat door Platina elektrodes. Deze biocompatibele composiet heeft goede actuerings- en sensoreigenschappen en vereist een lage werkingsspanning. Derhalve is zijn toepassing als potentiaalomvormer onderzocht in verschillende orgaanchiptoepassingen. Een eerste versie van de IPMC met een dikte van 180 µm (dik IPMC genoemd) heeft goede actueringseigenschappen en is getest in twee toepassingen: een micropomp en een mechanische weefselstimulator. Als mechanische weefselstimulator was het materiaal in staat biologisch relevante rek uit te oefenen (0.1 Een tweede dunnere polymeer versie van de IPMC (50 µm, dun IPMC) evenals een aangepast fabricatieproces zijn ontwikkeld. Het doel hiervan was om te verkennen of het materiaal zou kunnen dienen als sensor voor orgaanchips. Een comparatief onderzoek is uitgevoerd tussen dik en dun IPMC. Dit onderzoek toonde aan dat het gedrag van de elektrovrije depositiereactie verschilt afhankelijk van het substraatmateriaal. Dun IPMC is superieur in sensorcapaciteit vanwege zijn lagere buigstijfheid en hogere geleidbaarheid. Microfluidische stromingsmetingen en rekmetingen zijn getest als toepassingen van dun IPMC. Het materiaal heeft een goede sensorgevoeligheid als microfluidische stromingsmeter (4.78 mV/(µl/s)) en een lineair gedrag in het bestudeerde bereik. Daarnaast zijn zachte lithographie en patronering van hydrogels getest op dun IPMC om te beoordelen of het materiaal geschikt is als intelligent substraat voor weefselengineering. Naast het ontwikkelen van elektronisch bestuurbare flexibele membranen voor micropompen anticipeert deze scriptie een mogelijk significante invloed van intelligente materialen als middel in het ontwikkelen van multifunctionele kweeksubstraten voor OoCs.

1

Organ-on-chip and the role of actuation

Deus Sive Natura.

René Descartes

1

In this introductory Chapter, the drug development process is reviewed, and concepts of drug dilemma and organ-on-chip are introduced. In particular, the role of actuation in organ-on-chip is emphasized. Current limitations of existing materials and techniques used for actuation purposes are also discussed. Finally, ionic electroactive polymers are introduced and the scope and outline of the thesis are presented.

1.1. Pharmaceutical needs and drug dilemma

Drug development is a complex, expensive, and time-consuming process. Drug development goes through different stages, starting with the discovery of potential candidates for new drugs, then going through increasingly realistic and restrictive screening of drugs toward regulatory approval, and finally to commercialization.

1.1.1. Drug development process

Drug development cumulatively costs around $ 314 million to $ 2.8 billion per drug, and takes an average of a decade to be completed from research to a commercially available drug [1]. As reported by Marx *et al.* the amount of money spent over the decades has increased while the number of approved drug candidates has remained essentially the same (Table 1.1). During the past decades, some drugs even had to be withdrawn from the market because of potentially damaging side effects, such as Thalidomide which has led to more than 10 000 in utero abnormalities in the '60s and '70s. The phenomenon of investing more and more money over time for little to no outcome has been referred to as the drug "dilemma".

Decade	Average money spent	Number of drugs approved
1970-1980	179M$	165
1980-1990	413M$	212
1990-2000	1B$	303
2000-2010	2.6B$	226

Table 1.1: Spending of the members of the Pharmaceutical Research and Manufacturers of America (PhRMA, 2015) over the last decades with respect to the number of drugs approved. Adapted from [2]. The presented cost has to be indexed to the inflation at the time of the study.

Also because of those tragic side effects, drugs currently undergo a long, complex, and precise process before approval for patients. It starts with the discovery of potential drug candidates out of thousands and the use of in-vitro 2D cultures (petri dish and well-plate) and animal testing before going through tests in humans. The pre-clinical testing requires animals, which are known to poorly reproduce human metabolism in addition to being ethically controversial [3]. Developing and testing drugs on animals also might lead to missing potentially deadly side effects, as mammal biology still differs from human biology despite many similarities in

metabolism [4]. The clinical test begins with healthy volunteers (phase 1) then continues with cohorts of hundreds of patients (phase 2) and finally thousands of patients (phase 3). The results of the last remaining drug candidate after the full screening process can be submitted to the drug approval organization (Figure 1.1). Therefore as it currently stands the drug development process is time-consuming, non-mechanisms specific, and expensive. However, this drug screening approach is still fundamental to drug development and its inherent complexity reflects the staggering complexity of human physiology.

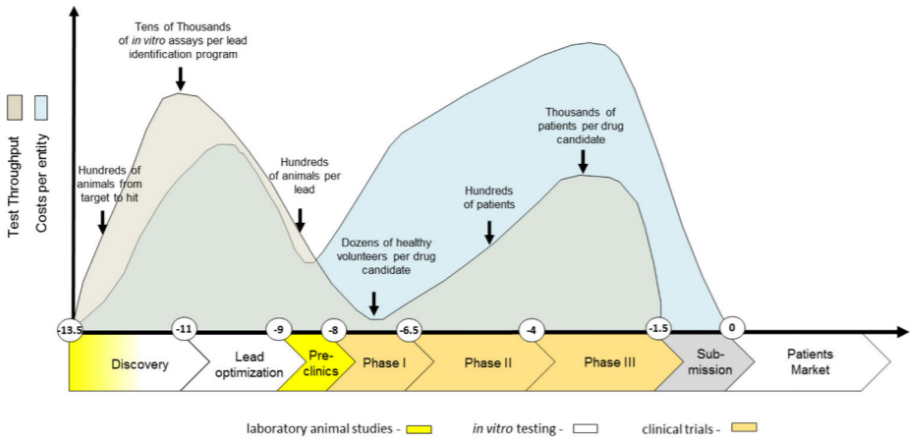

Figure 1.1: The drug development process. Extracted from [2].

As reported by Marx *et al.* emerging technologies such as organ-on-chip have been reported as being a potential cornerstone in the process of drug development as they can help researchers and scientists to unravel possible side effects in the early stage. Organ-on-chip can even help to better understand disease mechanisms to individuate potential drug candidates and better analyze the impact of drugs on cells and eventually organisms. Developing such a technology could be decisive to help reduce costs and delay during the development of new drugs [2].

1.2. Organ-on-chip

An organ-on-chip (OoC) is a microelectromechanical (MEMS) device that aims to recapitulate in-vitro the physiology of the smallest functional unit of an organ in order to perform drug analysis or study disease models. As reported by Zhang and Radisic [5], organ-on-chip technology is rising more and more interest as it promises to deeply change the way drugs are being developed. Hence more and more publications have been produced during the past decades (Figure 1.2). Other reports found that organ-on-chips could have a very positive impact on the pharmaceutical industry [6].

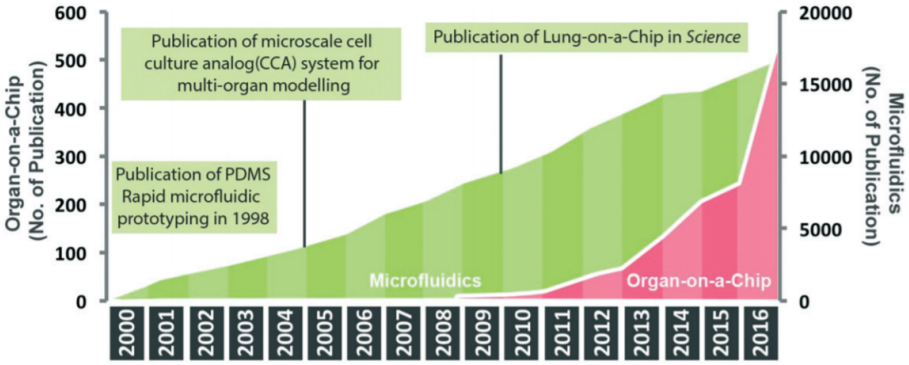

Figure 1.2: Numbers of publications in the organ-on-chip and microfluidics domain. Extracted from [5].

1.2.1. Role of actuation in organ-on-chip

Mechanobiology is the branch of biology studying the impact of mechanical cues on cells and tissues. Mechanobiology is crucial to obtain biologically relevant models. Therefore the core of organ-on-chip technology is mechanobiology, where MEMS-based devices aim at reproducing a more relevant micro-environment for cell constructs such as tissues and organoids than standard 2D culture systems such as well-plates. The microenvironment in the OoC is improved in comparison to standard cell culture by means of mechanical cues such as topographical structures, direct mechanical inputs, and control of fluidics (gradient of molecules of interest and shear stress). The organ-on-chip field is 2 decades old, it started in the late '90s with the improvement of soft lithography and the utilization of Polydimethylsiloxane (PDMS), a soft biocompatible, and transparent polymer. This means cells were able to be cultured in an environment that could be mechanically stimulated and optically monitored. In the early 2000's the microscale cell culture analog (CCA) [7, 8] paved the way for the publication of the so-called lung-on-chip device in 2010, which first integrated mechanical stimuli in a PDMS-based device to mimic a breathing pulmonary alveoli (Figure 1.3) [9]. Briefly, the lung-on-chip device works as follows: a porous membrane is inserted in between 2 PDMS channels, therefore the porous membrane can allow the co-culture of different cells type on each side of the membrane. Additionally, chambers are designed on each side of the membrane, and repetitive pneumatic changes in internal pressure are set in order to stretch the membrane and mimic a breathing lung.

As shown by J. Polacheck *et al.* [10] the mechanical inputs can be very different depending on the tissue which is studied (Figure 1.4). In addition, cells are known to experience mechanotransduction, an intrinsic mechanism that changes the phenotype of the cultured cells because of mechanical inputs, resulting in feedback [10]. Mechanical cues are crucial for the control of different biological mechanisms in the human body such as embryological development, morphogenesis, vasculogenesis, tissue patterning, and ultimately cells' fate [11].

Nowadays microphysiological systems (MPS) can either integrate a microfluidic

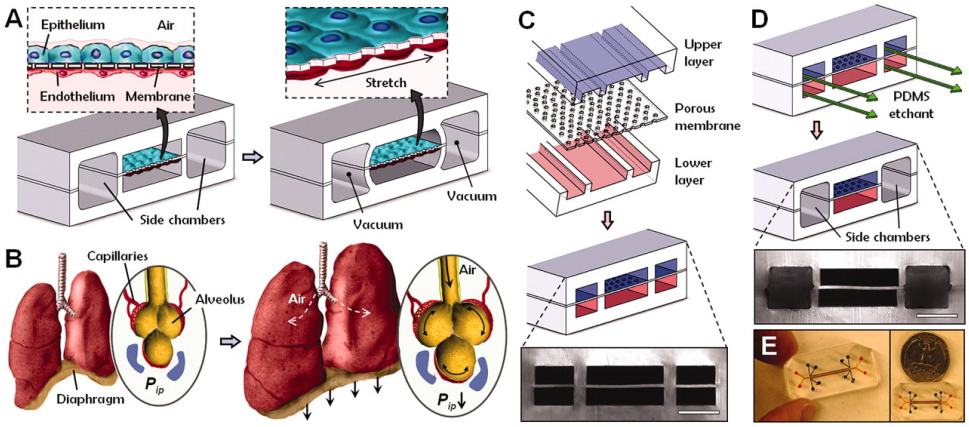

Figure 1.3: First generation of organ-on-chip, mostly using pneumatic actuation and PDMS. Extracted from [9].

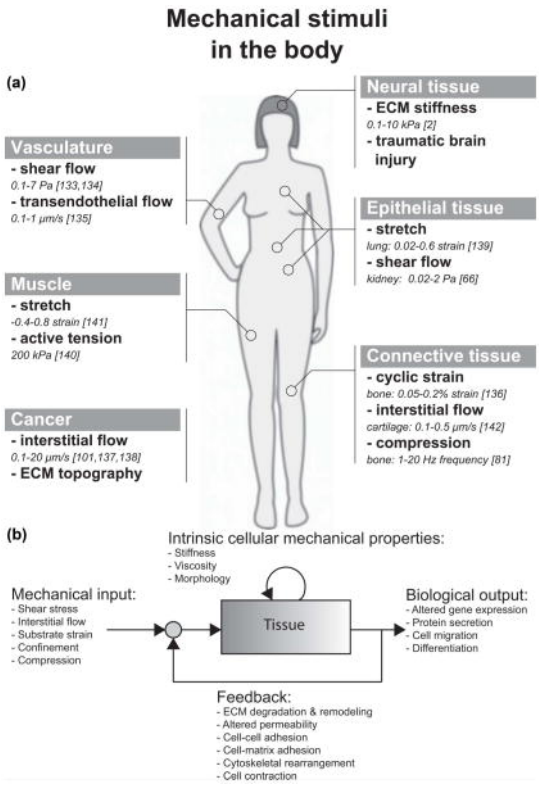

Figure 1.4: Illustration of mechanical stimuli found in various tissues inside the body. Extracted from [10].

circuitry to induce shear stress and metabolites renewal (organ-on-chip) or can be free of microfluidics but integrate topological clues (pillars, thin film platform, microgrooves...) [12–14]. MPS can also integrate complex chemistry for 3D culture or self-organization of the tissue (organoids, hydrogel...) (Figure 1.5) [15, 16].

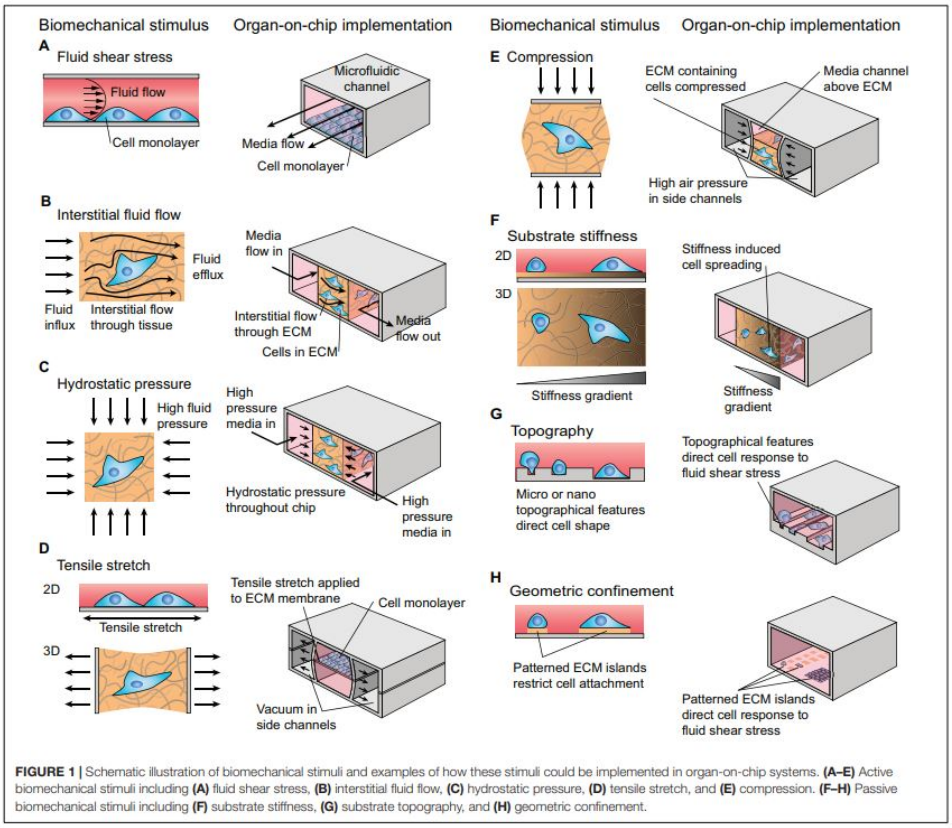

FIGURE 1 | Schematic illustration of biomechanical stimuli and examples of how these stimuli could be implemented in organ-on-chip systems. **(A–E)** Active biomechanical stimuli including **(A)** fluid shear stress, **(B)** interstitial fluid flow, **(C)** hydrostatic pressure, **(D)** tensile stretch, and **(E)** compression. **(F–H)** Passive biomechanical stimuli including **(F)** substrate stiffness, **(G)** substrate topography, and **(H)** geometric confinement.

Figure 1.5: Examples of biomechanical inputs and their implementation in organ-on-chip technology. Extracted from [17].

1.2.2. Impact and current limitation of OoC

Actuation methods

The first generation of organ-on-chip used to be a cell culture embedded in a microfluidic circuit in order to induce shear stress (Figure 1.3). Most of the OoC devices are pneumatically actuated as we can find in the pioneering work on the lung-on-chip device coming from Ingber's group [9] (Figure 1.3), or the multi-OoC platform from Marx's group [18]. Pneumatic actuation is a very simple method to control flow rate or mechanically stress cells. Unfortunately, it requires a complex setup which still limits the scalability of the OoC technology as it requires a flow pressure controller out of the incubator. Microfabricated integrated actuators for

cell stimulation and driving fluidics within an OoC would allow a more user-friendly device (no microfluidic tubings and pressure controller) and a more reproducible OoC. Furthermore finding a new way to actuate membranes or scaffolds where cells are growing would be of great interest for some devices in order to induce controlled mechanical inputs to the tissue. For instance, the so-called "Cytostrech" leaves the basal membrane side free of cells to be able to apply pressure imbalance while the other side of the membrane is dedicated to cell culture [19] (Figure 1.6). Finding a new way to actuate porous membranes using integrated meams would allow co-culture on each side of the membrane leading to more complex biological models (blood-brain barrier, gut, lung, neural vascular unit, vascularized heart...). Therefore, among different hurdles, the lack of integrated transducers within the moving diaphragm limits the relevance of the biological model and ease of use. Those hurdles are currently the biggest limitations of organs-on-chip [20].

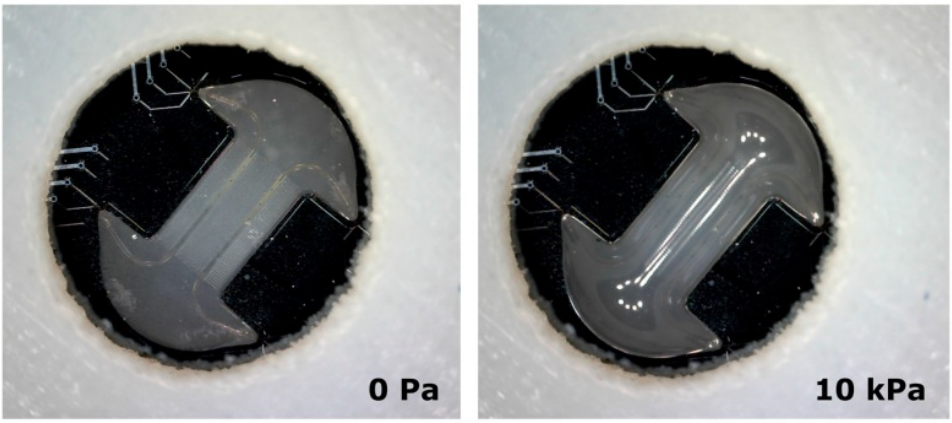

Figure 1.6: Top view of a PDMS-based membrane actuated using pressure controller. The membrane (a) can be inflated (b) in order to exert mechanical cues to the tissue. Extracted from [19].

Fabrication techniques and materials

In addition to actuation techniques, another limitation of OoC is the fabrication techniques that hamper scalability, as well as the material used that presents limiting effects for a drug study. Most organs-on-chip use polydimethylsiloxane (PDMS) and soft lithography to manufacture the device. Soft lithography, despite its ease of use which helped the development of OoC in the beginning, requires manual handling (peeling off) and is hardly scalable to mass production. Therefore high-volume production techniques such as wafer-scale microfabrication techniques as well as new methods such as hot embossing might be a way to ease the manufacturing of organ-on-chip and scale up the production. By scaling the production one could imagine reducing the cost of chips and developing high-throughput drug screening similar to the already existing early-stage development in drug candidate screening.

In addition, PDMS also shows side effects. The material is known to absorb small molecules of interest such as drugs or metabolites. This disadvantage is extremely damaging for drug screening as the PDMS will absorb the injected drug, making it barely possible to estimate precisely what is the amount of drugs reaching the studied tissue. The use of materials such as silicon and glass or nonpermeable printable resin could avoid this issue. One could for instance imagine developing an organ-on-chip where the flexible substrate where cells are growing and experiencing shear stress is made of tetrafluoroethylene-propylene (FEPM) elastomers while the rest of the chip could be made of non-permeable materials [21]. It should be pointed out also that the integration of sensors has been reported as a current limitation of OoC, as the field is urgently requiring tools to precisely assess the tissue in situ. While developing a device, the choice of the material is of crucial importance as it will determine the techniques that could be used in order to integrate sensors within the device. For instance by using silicon one can think about standard, patternable metal. Also using materials that could present inherent sensing capabilities, unlike PDMS, could be a way to overcome the limitation of sensor integration.

These findings regarding actuation means, fabrication techniques, and sensor integration are also in line with the literature. It has been reported that OoC technology has strongly been driven by academic research, and a few companies and start-ups are leading the market, most of them being funded by former academic researchers with scarce industrial backgrounds, using mostly PDMS and standard fabrication techniques. A fact that could explain the lack of scalability and ease of use of the final devices. Other authors also found that the limitations and needs of the field are to scale up production of organ-on-chip, standardization, lack of acceptance and procedures by government agencies, ease of use, and automation [20]. Nevertheless, the FDA Modernization Act has been accepted recently (late 2022), paving the way for broader acceptance of OoC Technology by government agencies.

1.3. Scope and outline of this thesis

1.3.1. Ionic electroactive polymer for next-generation organ-on-chip

The research presented in this thesis focuses on a transductive material that offers promising properties for organ-on-chip. An ionic electroactive polymer has been proposed and experimented with for different applications in the organ-on-chip field in order to increase the ease of use, integrability, and scalability of OoC. The material presented in this thesis is called ionic polymer metal composite (IPMC) and consists of a soft polymer enriched with ions flanked by platinum electrodes on opposite sides of the polymer. As it will be shown, this biocompatible material exhibits good combination of properties (strains, softness, two-way transduction), close to muscles. Additionally, it requires low driving voltages and has been herein investigated as a potential transducer for several organ-on-chip applications: a micropump, a cells stretcher, a microfluidic flow sensor, and a strain sensor, respectively. Furthermore, the integration of this material in a wafer-scale process

flow is investigated using state-of-the-art microfabrication tools to demonstrate the compatibility of IPMC within silicon-based technology as well as stereolithography techniques.

1.3.2. Outline

The thesis is structured in seven chapters. This first chapter introduced organ-on-chip technology, its concept, recent improvements, and current limitations. Chapter 2 describes the first proof of concept of using an ionic polymer metal composite for mechanical stimulation of a smooth muscle cell culture as well as the potential to use this material for a strain sensor. In Chapter 3 the standard, thick IPMC is integrated into a PDMS membrane for micropumping application in order to mimic a vascular channel. The actuated flexible membrane has been integrated into the design in order to drive fluid within a microfluidic system for vessel-on-chip applications. A first attempt also has been made to manufacture the micropump by means of a wafer-scale process flow by using glass-silicon-based microfabrication techniques. The material used in Chapter 2 and Chapter 3 is 180 μm-thick and shows some limitations for sensing applications because of its inherent thickness that leads to high flexural rigidity. Therefore, a thinner version of the material has been developed (50 μm-thick) in order to explore sensing applications for OoC. For the first time, in Chapter 4, a precise comparative study has been performed on the electroless deposition of platinum on thin Nafion compared to thick Nafion, and an explanation proposed of the dynamics of the reaction. The thin version of the material has been improved and the material characterized. The developed material could be further used as a sensor for microscale applications. In Chapter 5 techniques used to actually embed a 2D cell culture with topological cues on top of the thin IPMC described in Chapter 4 are depicted. Soft lithography approaches, as well as new techniques to print biologically relevant cues (grooves) on a SU8 substrate, are discussed together with hydrogel-based approaches. In Chapter 6 the thin version of the IPMC is used as the core of a flow sensor for organ-on-chip application, and the flow sensor capabilities are characterized. In the last chapter (7) a conclusion is given regarding the potential of using IPMC for organ-on-chip as well as recommendations for future work regarding the development of ionic electroactive polymers for transducer applications in organs-on-chip.

References

[1] O. J. Wouters, M. McKee, and J. Luyten, *Estimated Research and Development Investment Needed to Bring a New Medicine to Market, 2009-2018,* JAMA **323**, 844 (2020).

[2] U. Marx, T. B. Andersson, A. Bahinski, M. Beilmann, S. Beken, F. R. Cassee, M. Cirit, M. Daneshian, S. Fitzpatrick, O. Frey, C. Gaertner, C. Giese, L. Griffith, T. Hartung, M. B. Heringa, J. Hoeng, W. H. de Jong, H. Kojima, J. Kuehnl, M. Leist, A. Luch, I. Maschmeyer, D. Sakharov, A. J. A. M. Sips, T. Steger-Hartmann, D. A. Tagle, A. Tonevitsky, T. Tralau, S. Tsyb, A. van de Stolpe, R. Vandebriel, P. Vulto, J. Wang, J. Wiest, M. Rodenburg, and A. Roth, *Biology*

inspired microphysiological system approaches to solve the prediction dilemma of substance testing, ALTEX **33**, 272 (2016).

[3] D. E. Ingber, *Human organs-on-chips for disease modelling, drug development and personalized medicine,* Nature Reviews. Genetics **23**, 467 (2022).

[4] J. Mestas and C. C. W. Hughes, *Of mice and not men: differences between mouse and human immunology,* Journal of Immunology (Baltimore, Md.: 1950) **172**, 2731 (2004).

[5] B. Zhang and M. Radisic, *Organ on a chip devices advance to market,* Lab on a Chip **17**, 2395 (2017).

[6] N. Franzen, W. H. van Harten, V. P. Retèl, P. Loskill, J. van den Eijnden-van Raaij, and M. IJzerman, *Impact of organ-on-a-chip technology on pharmaceutical R D costs,* Drug Discovery Today **24**, 1720 (2019).

[7] K. Viravaidya, A. Sin, and M. L. Shuler, *Development of a Microscale Cell Culture Analog To Probe Naphthalene Toxicity,* Biotechnology Progress **20**, 316 (2004), _eprint: https://onlinelibrary.wiley.com/doi/pdf/10.1021/bp0341996.

[8] A. Sin, K. C. Chin, M. F. Jamil, Y. Kostov, G. Rao, and M. L. Shuler, *The Design and Fabrication of Three-Chamber Microscale Cell Culture Analog Devices with Integrated Dissolved Oxygen Sensors,* Biotechnology Progress **20**, 338 (2004), _eprint: https://onlinelibrary.wiley.com/doi/pdf/10.1021/bp034077d.

[9] D. Huh, B. D. Matthews, A. Mammoto, M. Montoya-Zavala, H. Y. Hsin, and D. E. Ingber, *Reconstituting Organ-Level Lung Functions on a Chip,* Science **328**, 1662 (2010).

[10] W. J. Polacheck, R. Li, S. G. M. Uzel, and R. D. Kamm, *Microfluidic platforms for mechanobiology,* Lab on a Chip **13**, 2252 (2013).

[11] T. Mammoto and D. E. Ingber, *Mechanical control of tissue and organ development,* Development (Cambridge, England) **137**, 1407 (2010).

[12] M.-H. Wu, S.-B. Huang, and G.-B. Lee, *Microfluidic cell culture systems for drug research,* Lab on a Chip **10**, 939 (2010).

[13] J. U. Lind, M. Yadid, I. Perkins, B. B. O'Connor, F. Eweje, C. O. Chantre, M. A. Hemphill, H. Yuan, P. H. Campbell, J. J. Vlassak, and K. K. Parker, *Cardiac Microphysiological Devices with Flexible Thin-Film Sensors for Higher-Throughput Drug Screening,* Lab on a chip **17**, 3692 (2017).

[14] A. M. Greiner, B. Richter, and M. Bastmeyer, *Micro-Engineered 3D Scaffolds for Cell Culture Studies,* Macromolecular Bioscience **12**, 1301 (2012), _eprint: https://onlinelibrary.wiley.com/doi/pdf/10.1002/mabi.201200132.

[15] M. Hofer and M. P. Lutolf, *Engineering organoids,* Nature Reviews Materials **6**, 402 (2021), number: 5 Publisher: Nature Publishing Group.

[16] M. Verhulsel, M. Vignes, S. Descroix, L. Malaquin, D. M. Vignjevic, and J.-L. Viovy, *A review of microfabrication and hydrogel engineering for micro-organs on chips,* Biomaterials **35**, 1816 (2014).

[17] C. L. Thompson, S. Fu, H. K. Heywood, M. M. Knight, and S. D. Thorpe, *Mechanical Stimulation: A Crucial Element of Organ-on-Chip Models,* Frontiers in Bioengineering and Biotechnology **8**, 1426 (2020).

[18] B. Ataç, I. Wagner, R. Horland, R. Lauster, U. Marx, A. G. Tonevitsky, R. P. Azar, and G. Lindner, *Skin and hair on-a-chip: in vitro skin models versus ex vivo tissue maintenance with dynamic perfusion,* Lab on a Chip **13**, 3555 (2013).

[19] N. Gaio, B. van Meer, W. Quirós Solano, L. Bergers, A. van de Stolpe, C. Mummery, P. M. Sarro, and R. Dekker, *Cytostretch, an Organ-on-Chip Platform,* Micromachines **7** (2016), 10.3390/mi7070120.

[20] M. Mastrangeli, S. Millet, t. O. Partners, and J. v. d. E.-v. Raaij, *Organ-on-Chip In Development:Towards a roadmap for Organs-on-Chip,* (2019), 10.20944/preprints201903.0031.v1.

[21] S. B. Campbell, Q. Wu, J. Yazbeck, C. Liu, S. Okhovatian, and M. Radisic, *Beyond Polydimethylsiloxane: Alternative Materials for Fabrication of Organ-on-a-Chip Devices and Microphysiological Systems,* ACS Biomaterials Science & Engineering **7**, 2880 (2021), publisher: American Chemical Society.

2

An electroactive polymer for organs-on-chip: the ionic polymer metal composite (IPMC)

Beauty will save the world.

Dostoevsky

Parts of this chapter have been published in IEEE International Conference on Soft Robotics (RoboSoft) (2020) pp 530-535, April 2020, Yale, USA. [1].

In this Chapter ionic electroactive polymer is used for the first time as an actuator for smooth muscle cells, the platform show no side effects on the tissue with biologically relevant strain achieved (0.1 %).

2.1. Introduction

Organs-on-chip mostly rely on techniques such as pneumatic actuation and rocking platform to induce the very important mechanical inputs required to precisely mimic a biologically relevant microenvironment. As seen in the previous chapter, those methods are primarily used in the OoC field because of their ease of use and implementation. The early users of OoC were biologists and they legitimately first focused on easy-to-implement solutions that could give high enough strain (pneumatic actuation). To overcome the downsides of pneumatic actuation as a mechanical stimulation on cell culture, many other actuation mechanisms can be considered, and every one of them has some advantages and limitations. The following Table 2.1 gives a non-exhaustive view of the field. The discussion is still open concerning other techniques or materials. According to Desmaële *et al.* we can highlight the fact that some techniques shouldn't be considered because of known pernicious side effects and cytotoxicity (electrothermal, electrostatic). In addition, regarding the actuation mechanisms for cell stimulation, some other parameters have to be considered such as ease of implementation, cell medium compatibility and actuator size (Figure 2.1). Some other materials such as shape memory alloys also have been proposed for actuation [3], however, the mechanism is based on thermal contraction of the material. Heat might lead to potential side effects as cells are known to experience apoptosis above 40 °C. In addition, thermal contraction has a long response time. We can also mention piezoelectric materials however the most common piezoelectric materials are based on lead, a well-known dangerous and cytotoxic chemical [4]. In addition, piezoelectric actuation requires high voltage. It only gives a small displacement despite the fact that piezo actuation is very well controlled and can respond within a wide range of frequencies. We can also mention moving stages [5], this technique despite its ease of implementation offers limited control in the small range of displacement with delicate mechanical input. In addition, this technique often requires bulky equipment hampering its integrability in an already existing system. Magnetic actuation can also be considered as a technique to actuate cell tissue, however, it requires a bulky magnet as well as the thick magnetically-doped-membrane required to have enough actuation capability, limiting its ease of use and integrability [6, 7].

Desmaële *et al.* reviewed the parameters that ideal actuators should show in order to meet requirements (Figure 2.1), it can be seen that dimension of the area that need to be actuated is also important as single cell actuation or tissue actuation doesn't require the same amount of energy.

As reported in the previous chapter, finding ways to integrate electronically controllable substrate is a crucial need for Organ-on-chip in order to overcome the drug dilemma. From the different approaches reported above, and Table 2.1 it is clear

Table 2.1: Advantages and limitations of current techniques used to actuate cell culture.

Actuation mechanism	Advantages	Limitation
Piezoelectric	high controllability	potentially cytotoxic [4]
Thermal contraction	no charges involved	potentially cytotoxic, long response time [3]
Magnetic	non cytotoxic	require magnets and bulk for enough displacement [6, 7]
Moving stage	high controllability	precision, integrability [5]

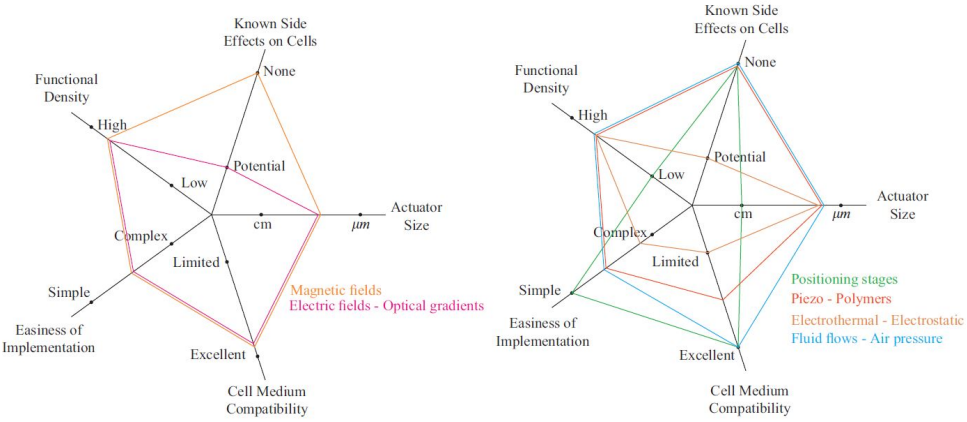

Figure 2.1: Criteria considered for further comparison of the actuation means found in MEMS dedicated to cell stimulation. Extracted from [2].

that new actuations mechanisms and materials are required. Therefore the focus should be on promising new materials that can show good actuation capabilities, such as conductive polymers. Balint *et al.* focus on conductive polymers for different applications in tissue engineering [8]. As reported by Balint *et al.* the key parameter is the dopants type and concentration regarding conductive polymers. Interestingly Jager *et al.* reported the use of conjugated microfabricated conductive polymer for mechanotransduction application and cell handling [9]. Jager *et al.* developed microactuators based on conductive polymer for single cells manipulation [9]. Taccola *et al.* fabricated and patterned free-standing poly(3,4-ethylenedioxythiophene) polystyrene sulfonate PEDOT:PSS with SU8 bilayer microactuators in the form of microfingers of a variety of lengths for single cell handling [10]. Electroactive polymers (EAP) can be divided in different subtypes, one can distinguish the ionic electroactive polymer (iEAP) and the electronic active polymer (EAP). The actuation mechanism of the first one is based on the diffusion of ions while the second one is based on Coulomb forces. The dielectric elastomer actuators (DEA) which have been used for cell culture consist of a polymer doped with carbon black, upon the application of high voltage the charges distributed along the polymer will attract or

repeal depending on the polarity, the polymer will therefore bend accordingly. DEA has been used for mechanical stimulation of living tissue [11]. Despite the elegant approach dielectric elastomers are a dangerous option as they require high voltage that can lead to cytotoxicity.

2.2. Ionic electroactive polymer

Choosing the right materials for actuation purposes is a crucial point. Interestingly ionic electroactive polymers present inherent good properties that could be used in order to actuate human cell tissues. Bhandari *et al.* compared the ionic electroactive polymer versus the electronic electroactive polymer (Table 2.2) [12]. What can be found is that the ionic-based polymers are inherently working better in wet environments, which could be interesting for OoC as the culture media standardly used in OoC are water-based compounds doped with ions in order to keep the osmotic pressure.

Table 2.2: Comparison of properties between electronic and ionic EAPs. Adapted from [12].

Parameter	Electronic (EAP)	Ionic (iEAP)
Actuation Voltage	Large	Small
Controllability	Easy	Difficult
Energy Density	Good	Poor
Mechanism	Coulomb forces	Mobility or diffusion of ions
Electrolyte	Absent (dry)	Present (wet)
Displacement	Change shape or dimensions	Bending

2.2.1. Ionic polymer metal composites

One of the transductive materials which might rise interest is ionic polymer metal composites (IPMC). It has already been studied for cells applications, for instance, Hitsumoto *et al.* reported for the first time the use of IPMC in order to actuate cells [13]. In the work of Miriyev *et al.*, IPMC actuation capabilities: actuation stress vs strain and actuation strain vs efficiency have been plotted with respect to other materials (Figure 2.2). What can be found is that the IPMC shows very good actuation capabilities, close to the human muscle (Figure 2.2 [14]). We can mention also the dielectric elastomer actuator (DEA) and high-strain fluidic elastomer actuators (FEA), and pneumatic artificial muscle (PAM). However as reported previously, DEA relies on high voltage which might hamper the cell phenotype, while FEA and PAM rely on pneumatic system. Liang *et al.* also compared different i-EAP with muscle (Figure 2.3), one can see that the strain achieved by IPMC is close to the one achieved by natural muscle, actually, IPMC is also called artificial muscle in the soft robotics field [16]. In this chapter, we will introduce the IPMC as a substrate for cell culture with actuation and sensing capabilities. We designed and fabricated a well-plate compatible and electronically controllable substrate, and we successfully demonstrated the viability of the concept by culturing cells under dynamic loading

conditions.

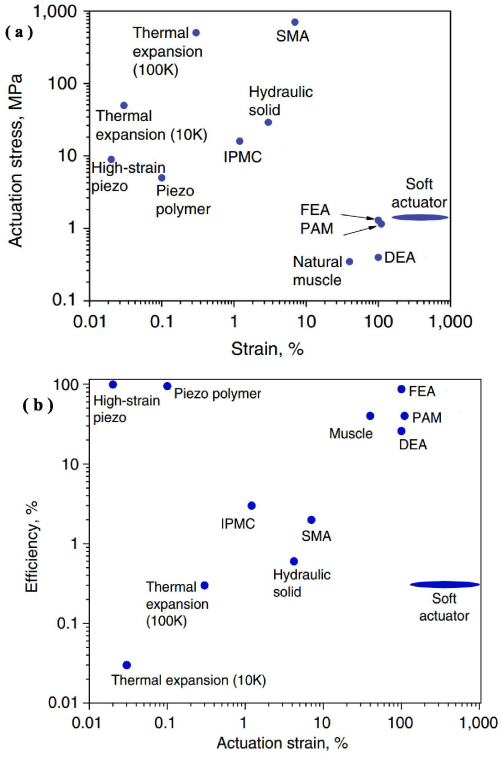

Figure 2.2: IPMC vs. other actuators (a) Actuation stress plotted against strain. (b) Maximal efficiency plotted versus actuation strain. (DEA: dielectric elastomer actuator, FEA: fluidic elastomer actuator, PAM: pneumatic artificial muscle, SMA: shape memory alloy). IPMC exhibit high strain and actuation stress while using low voltage and being compatible with water-based environments. Extracted from [14].

2.3. An IPMC-based platform for actuation and sensing

IPMCs are typically made of a perfluorinated sulfonic acid (PFSA) ion-conductive polymer known under the brand name of Nafion and chemically coated with platinum [17]. The PFSA is composed of a chemically-stable fluoropolymer-copolymer covalently bonded with anions (sulfonate). The material is water-permeable and absorbs cations, which can freely move in the polymer backbone. Nemat-Nasser gives an explanation of the mechanisms involved during the actuation of an IPMC. Upon application of an electrical field, the moving cations drift towards the cathode, and the rearrangement of charged species within the polymer will locally lead to the reorganization of the polymer backbone. This reorganization will induce an expansion of the polymer at the cathode and a contraction at the anode, leading

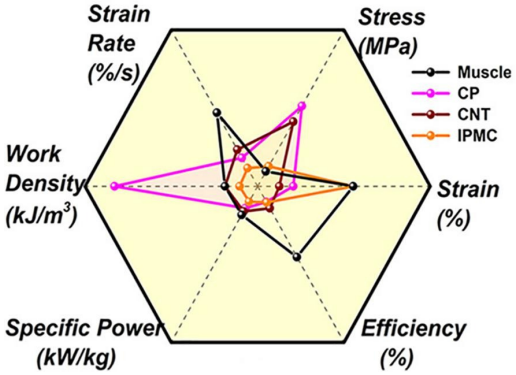

Figure 2.3: Radar plot of comparison between i-EAPs and skeletal muscle, CP conducting polymer, CNT carbon nanotubes. Despite low specific power, IPMC exhibits high strain, close to real muscle. This characteristic makes the IPMC a good candidate for OoC. Extracted from [15].

to a net displacement towards the anode (Figure 2.4) [18].

The principle of the platform is depicted in Figure 2.4. The culture medium widely used in cell biology is mostly composed of sodium cations, in the case of IPMC sodium cations will penetrate the polymer backbone. In actuation mode, upon application of an input voltage difference across the electrode pair, the loosely coupled sodium cations within the ionic polymer membrane migrate towards the cathode, causing the cantilever-shaped IPMC to bend. The bending thus achieved imparts mechanical loading to the cells cultivated on the surface of the IPMC. In sensing mode, the intrinsic contraction of the cells induces a deformation of the IPMC and consequent displacement of the cations, leading to a voltage drop across the electrodes that can be measured as a readout signal.

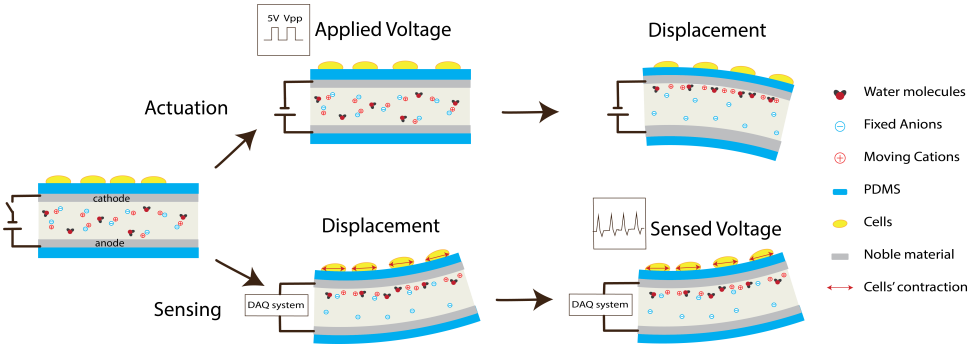

Figure 2.4: Sketch of the cross-section of the IPMC-based OoC working as actuator and sensor. In the actuation mode (top), the voltage applied between the electrodes induces a displacement of the polymer. In the sensing mode (bottom), cell contraction deforms the IPMC substrate, triggering cation migration and causing a charge imbalance, measurable as a voltage difference at the electrodes.

The proposed device is composed of two distinct parts (Figure 2.5). The first

includes a standard 12-well plate in which the IPMC substrate coated with polydimethylsiloxane and clamped between 2 gold electrodes is inserted. The second part is the electronic control board driving the IPMC substrate and running through a Matlab-based graphical user interface.

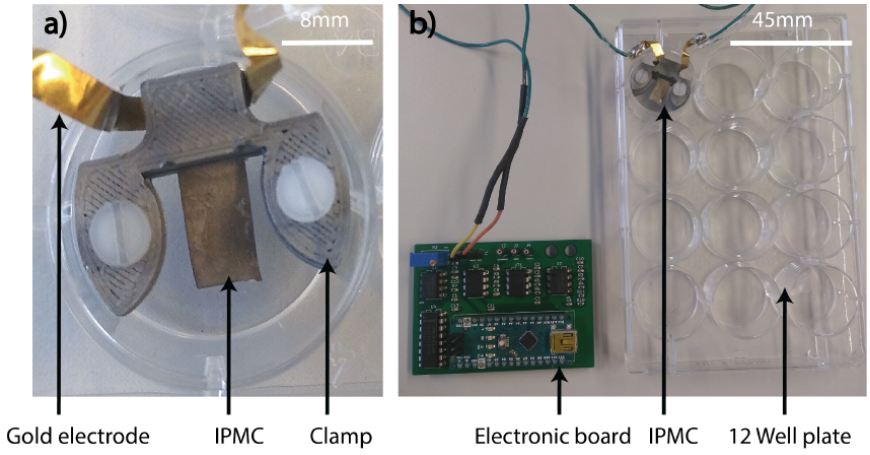

Figure 2.5: Full platform including a) the IPMC coated with PDMS and cells culture and b) the electronics board with the 12 well plates.

2.4. Electronics

The main purpose of the electronic board is to provide precise control over cantilever shape, displacement, and actuation frequency in the actuation mode, and to extract an accurate noise-free readout signal corresponding to the cantilever deformation induced by cell tissue contraction in the sensing mode. The operation modes are not simultaneous, and time division was adopted to allocate an optimal time interval to each mode. To enable all these functions, we designed a customized printed circuit board (PCB) centered around a small, inexpensive, and easy-to-use microcontroller (Arduino nano) (Figure 2.6 and 2.7). For the actuation part, a digital-to-analog converter (DAC) was used in series to the digital output of the microcontroller to actuate the IPMC substrate. Since the IPMC requires a current of around 100 mA to actuate properly, a standard amplifier was added after the DAC (Figure 2.6).

The amplifier and DAC were both powered by the microcontroller. A 2.5 V reference was used to deliver a full square wave with 5 Vpp amplitude as the Arduino nano cannot provide negative voltage. A second electronic circuit was designed on the same PCB to support sensing capabilities using the same IPMC substrate. The sensing circuit included a band-pass filter to remove parasitic and environmental noise; a differential amplifier together with a standard amplifier and active low-pass filters to read, amplify and filter the sensing signal from the IPMC substrate. The gain of the last amplifier in the sensing mode could be tuned up to 5000 thanks to a trimmer (Figure 2.7). The precise schematic of the electronic can be found in

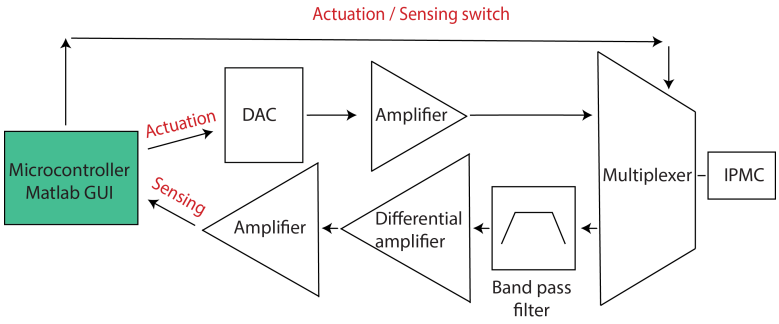

Figure 2.6: Schematic of the electronic circuit designed for both actuation and sensing.

Appendix 7.5.

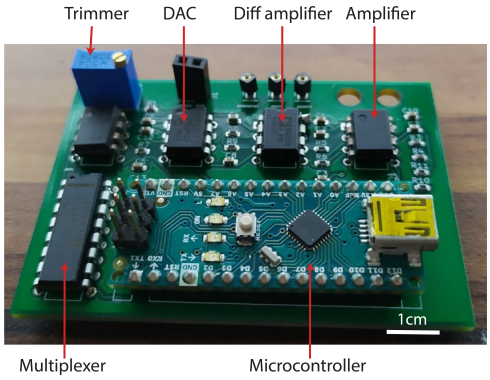

Figure 2.7: Close-up view of the printed circuit board including the single USB external connection, the microcontroller, the multiplexer, the DAC, the trimmer, and the amplifiers.

Finally, switching between the actuation and sensing modes of the system was enabled via a multiplexer controlled through the microcontroller. A graphical user interface (GUI) was developed for ease of use (Figure 2.8).

2.5. Characterization

Characterization of the actuation mode was performed by tracking the voltage-induced displacement of the IPMC cantilever using a laser triangulation sensor (ILD1750-2, Micro-Epsilon) connected to a data acquisition board (National Instruments) run through LabView. The setup to perform the frequency response analysis is sketched in Figure 2.9 and shown in Figure 2.10.

Experiments are based on applying sine waves of varying frequencies and measuring the corresponding tip displacement. We applied a frequency going from 0.1 Hz to 20 Hz which corresponds to physiological frequencies. Frequency spectra were obtained after analyzing the magnitude and phase difference between the applied signal and the resulting displacement. The experiments were performed

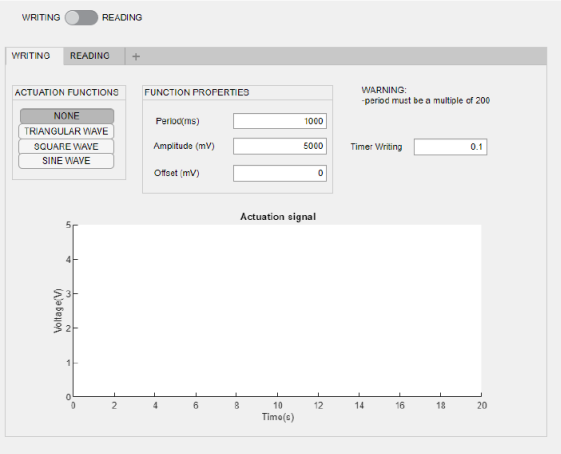

Figure 2.8: GUI developed to control the board, frequency amplitude, and shape of the actuation signal can be controlled in the writing mode. In the reading mode, the data can be saved in real-time.

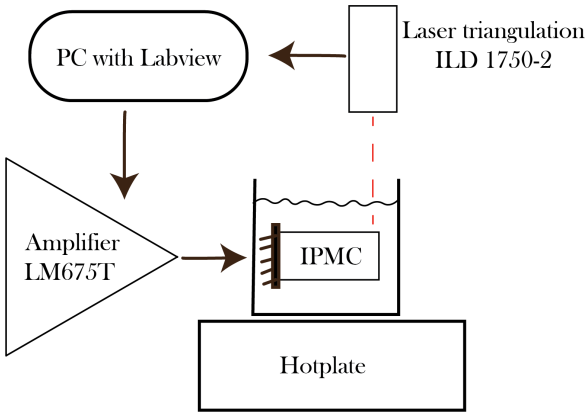

Figure 2.9: Experimental setup that is used to perform the frequency analysis

in different solutions by alternating deionized water and phosphate-buffered saline (PBS) solution. PBS contains the same amount of cations as standard culture media and is commonly used to wash cell cultures during culture medium change. Young's modulus of the IPMC was characterized by means of tensile tests. During the tensile test (Dynamic Mechanical Analysis Q800 TA), the sample is subjected to controlled tension and the stress-strain curve is calculated.

Actuation and sensing have been performed using the aforementioned electronic board (Figure 2.7). The characterization of the actuation mode showed a 0.04 mm/V actuation capability (Figure 2.11). We additionally noticed that the actuation characteristics did not change over a long actuation (4 hours) period. The measured Young modulus is 650 MPa which corresponds to the values in the literature [19].

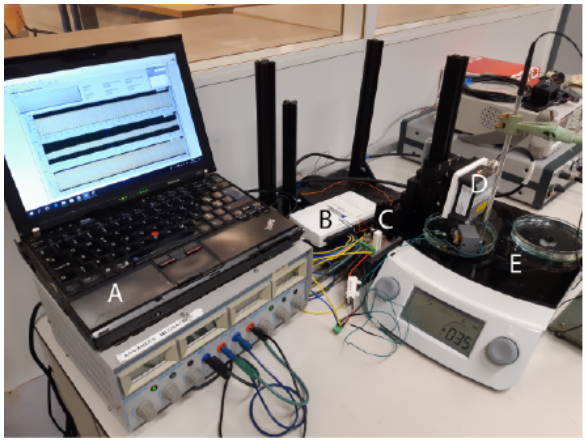

Figure 2.10: Frequency analysis setup. Including the PC for acquisition (A), the NA instruments DAQ (B), the amplifier (C), the laser (D), and the hotplate (E).

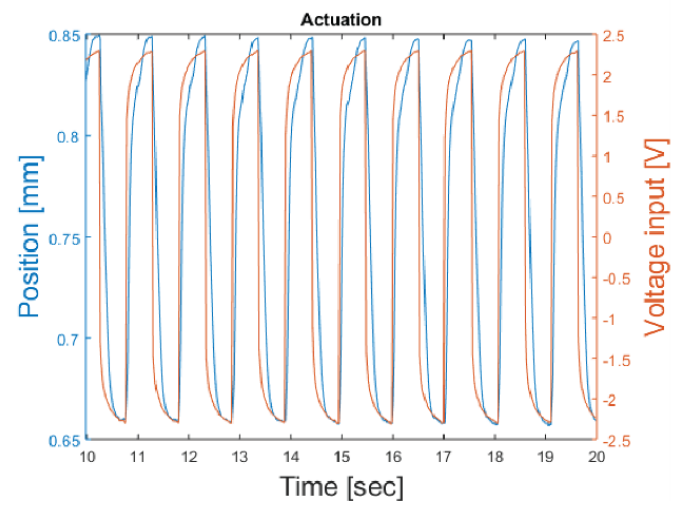

Figure 2.11: Actuation capabilities of the IPMC have been characterized, 1hz 5Vpp square signal has been used for actuation. The integrative behavior of the input signal is due to the capacitive behavior of the IPMC.

The frequency analysis shows a difference in actuation magnitude between PBS and DI water. In particular, the magnitude is higher in DI Water than in PBS at higher frequencies (1-20 Hz). We hypothesize that the saturation of cations within the IPMC immersed in PBS with high cation concentration leads to a smaller concentration gradient in the vicinity of the Pt electrodes, and thus lessens stress upon voltage application. Conversely, at lower frequencies (0.1 to 03 Hz) the magnitude is higher for the saline solution (Figure 2.12).

To characterize the sensing mode, a displacement was manually induced in the

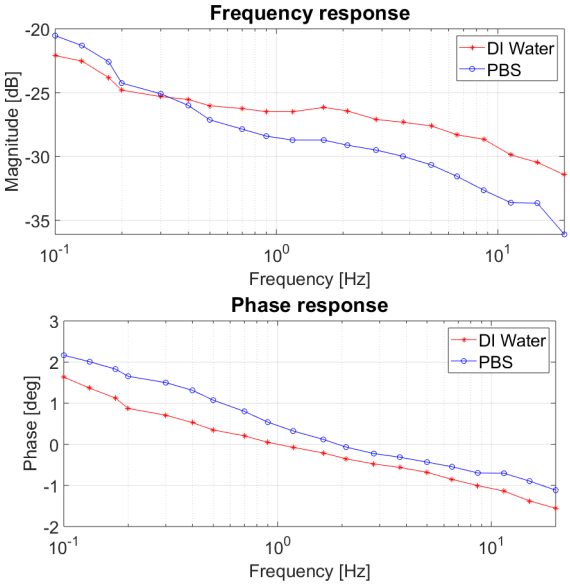

Figure 2.12: Bode plot for the IPMC cantilever actuated at 37° C both in DI water and in PBS.

IPMC and quantified using the laser triangulation sensor while the corresponding electric output signal was recorded through the control board. The sensitivity has been calculated as the average of the ratio between displacement and readout voltage (Figure 2.13). The sensitivity is 0.72 V/mm (Figure 2.13) with a trimmer giving a gain of around 2500, showing no parasitic noise. We also noticed that, under the cell culture conditions we used for the long-term actuation, the high concentration of sodium ions inside the culture medium is conducive to good actuation capabilities and prolonged viability of the IPMC. We hypothesize that the high concentration of sodium cations in the medium reduces the loss of the cations from the IPMC upon actuation, which is reported to shorten the lifetime of IPMCs [20].

2.6. Biology and mechanical input

The strain applied to the cells adhering to the top surface of the cantilever by the cantilever deformation was calculated as follows. Using traditional elastic beam theory, the lateral displacement of the beam in the vertical direction $(+y)$ is $v(x)$. In the elastic deformation regime, the curvature is related to the bending moment by:

$$\frac{d^2v(x)}{dx^2} = \frac{M(x)}{EI} = -\frac{P(L-x)}{EI} \tag{2.1}$$

with E the Young's modulus, $M(x)$ the bending moment, L the length of the beam and I the second moment of area. By integrating the above equation twice assuming no displacement $(x = 0)$ and no rotation $(x' = 0)$ at the base of the cantilever,

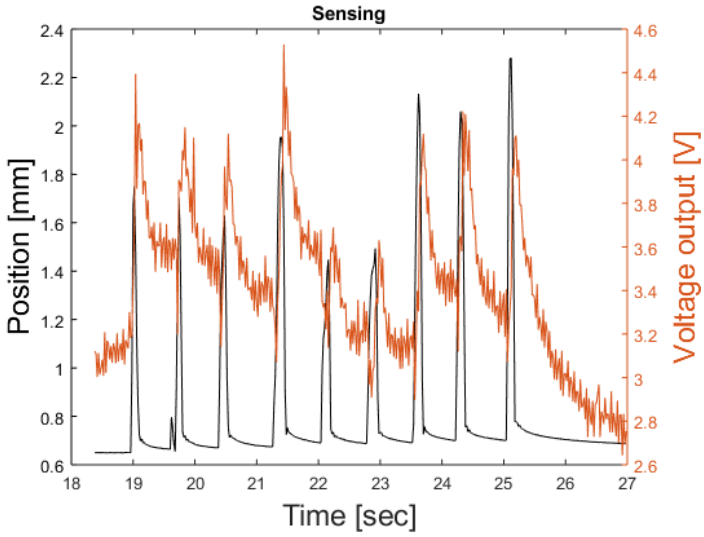

Figure 2.13: Characterization of the sensing capabilities. The induced displacement has been recorded using the electronic board and monitored using the laser triangulation system.

the equation of the displacement field is obtained as follows:

$$v(x) = -\frac{Px^2}{6EI}(3L - x) \tag{2.2}$$

P is the force applied to the cantilever. Accordingly, the lateral displacement δ (assumed downward) at the tip of the cantilever ($x = L$) is:

$$\delta = \frac{PL^3}{3EI} \tag{2.3}$$

Using the following definition of strain ϵ:

$$\varepsilon = \frac{\sigma}{E} = -\frac{M(x)t}{EI} \tag{2.4}$$

t being the thickness of the cantilever (200 μm). For $x = L$ and $t = \frac{h}{2}$, the strain can be correlated to the tip displacement:

$$\varepsilon = \frac{PLh}{2EI} = \delta\frac{3}{2}\frac{h}{L^2} \tag{2.5}$$

The main purpose of the present study was to study the cytotoxicity and biocompatibility of the IPMC substrate while actuated with living cells growing on its top surface. The biology and cell culture were performed by LUMC partners. Vascular smooth muscle cells (vSMCs) were obtained by differentiation from induced stem cells (iPSCs). High-density vSMCs were seeded on the substrate pre-coated

with fibronectin (Sigma Aldrich) and left in an incubator overnight at 37 °C, % 5 CO2, in Gibco® IMDM and Gibco® F12 culture media (1:1) to allow cell growth on the PDMS substrate. Several attempts also have been performed to actually pattern the cells anisotropically in order to create a tissue that could contract in one direction. To meet this purpose patterning of the surface has been performed using PRIMO system from Alvéole to print a grooves-like antifouling layer in order to induce alignment of the cultured cells. The resulting cells were actually patterned anisotropically (Figure 2.14). However, we noticed that the tissue was not confluent enough nor strong enough to actually be able to lift the cantilever.

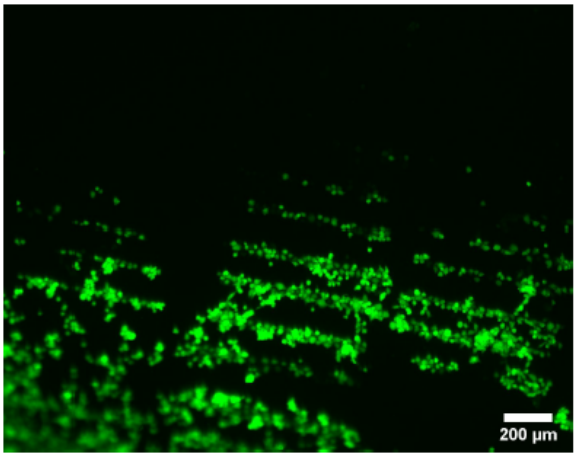

Figure 2.14: Vascular smooth muscle cells on the surface of the IPMC before being actuated for an extended period of time, the patterning can be seen, cells were actuated for an extensive period of time.

For the experiment with living cells, the seeded IPMC was connected to the printed circuit board in order to perform actuation. The cells were actuated for 150 minutes with a square wave input signal with a frequency of 1 Hz and amplitude of 3 Vpp (Figure 2.15).

However, we noticed that after a few minutes of actuation, the golden electrodes started to interact with the nutrient solution. The reaction stopped when the submerged gold turned completely black. The solution is filled with charged proteins and the constant flow of relatively high current through the electrodes caused an electro-deposition of these molecules on both the gold electrodes (since the current was going in both directions, the cathode electrode switched continuously). During the actuation, we were able to notice even higher displacement with respect to the one present in the characterization session. This was because the incubator was at a temperature of 36.7 °C, and at higher temperatures, the cations' movement capability is enhanced. During the characterization experiments, we measured a cantilever tip displacement of 0.2 mm. Given the dimensions of the clamped cantilever we used (L = 8 mm and t = 200 μm), we estimate via Eq 2.5 an induced strain of 0.094 %. This strain value corresponds to the circumferential strain value

experienced by cells in real condition *in vivo* in the jugular vein as previously reported in the rat [21].

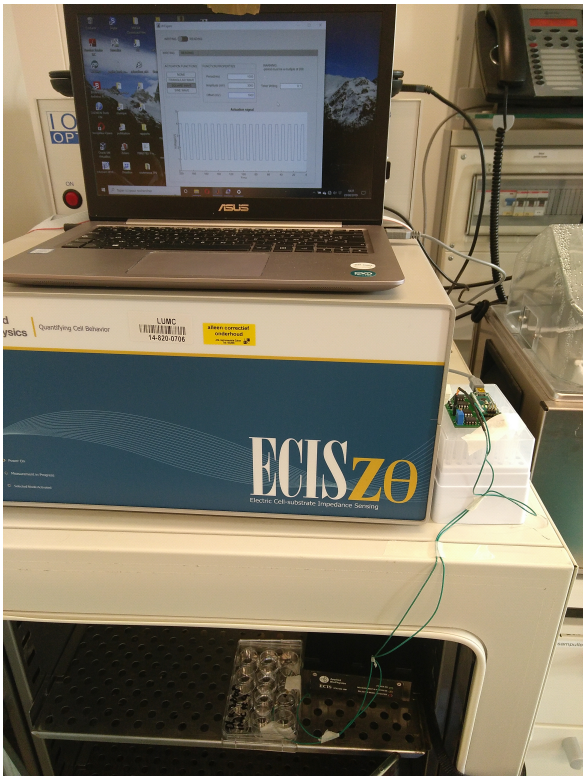

Figure 2.15: Actual setup during the experiment, the well-plate including the IPMC can be seen inside the incubator while the electronics board is situated next to the incubator with the computer on top.

After the experiments, the cells were stained using Calcein Am fluorescent dye (Sigma Aldrich) which only stains living cells. We evidenced no direct adverse effect, proving the suitability of IPMC-based organ-on-chip. We successfully actuated for 150 minutes the vSMC tissue cultivated on the IPMC substrate clamped to a 12-well plate inside a standard incubator (Figure 2.15) with no hydrolysis. The subsequent Calcein AM staining proved that after actuation stem cells were still alive with no adverse effects (Figure 2.16). Moreover, the cells showed an elongated shape, proving that vSMCs did not delaminate from the substrate despite the prolonged mechanical loading and that they were not affected by the actuation voltage. In addition, the overall view of the IPMC cantilever using reconstructed fluorescent images shows that the IPMC strip is not completely covered with cells, suggesting that the tissue engineering needs to be improved in order to actually be able to grow a tissue mature enough for displacing the IPMC cantilever (Figure 2.17). Further approaches are described in Chapter 5.

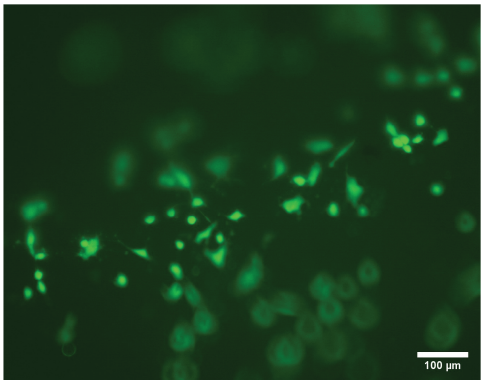

Figure 2.16: Vascular smooth muscle cells after being actuated for an extended period of time. The elongated shape of vSMC suggests that cells are not dying or detaching.

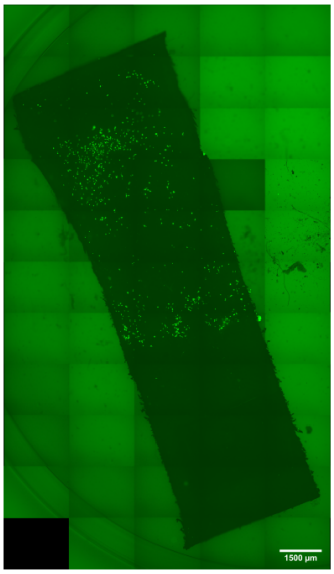

Figure 2.17: Reconstruction images of the actuated vSMC, vSMC cells can be seen on the IPMC material.

2.7. Conclusion

In this chapter, we have presented a novel, simple, inexpensive, and easy-to-use OoC device that could for the first time both perform actuation and sensing using the same substrate made out of a smart material. This first ionic polymer-based OoC allows the stretching of human cell tissues thanks to the unique properties of the IPMC under the electronic control of a microcontroller. Periodic actuation has been successfully performed for a few hours to induce mechanical load to a vascular smooth muscle cell culture (0.1 % strain with no hydrolysis issues). The

range of applied strain corresponds to the one experienced by cells *in vivo*, proving the relevance of using smart materials to mimic the human microenvironment for OoC applications. No adverse effects nor delamination of the human tissue were detected after actuation. Sensing has been characterized thanks to an externally induced displacement of the IPMC cantilever, showing good performance (0.72 V/mm). The proposed device could be easily tailored to many other uses and cell types, such as cardiomyocytes for heart-on-chip applications. However, the limited growth of the cells giving little to no contraction, and the inherent thickness of the IPMC hampers the actual recording of contraction. To solve this issue we propose in Chapter 4 the development of a thinner version of IPMC with lower flexural rigidity for sensing applications in bio-MEMS. In Chapter 5 the integration of hydrogel on top of this thin IPMC as well as soft lithography are discussed in order to obtain an aligned and matured tissue on the thin IPMC.

In the next chapter, another application of standard 180μm-thick IPMC is discussed: the IPMC-based micropump. IPMC is integrated within a flexible polymer membrane (polydimethylsiloxane) in order to have an electronically controllable micropump for microfluidics. In addition, a hydrogel-based channel is integrated within microfluidics in order to reproduce a compliant visco-elastic channel, mimicking a vascular network.

References

[1] P. Motreuil-Ragot, A. Hunt, D. Kasi, B. Brajon, A. v. d. Maagdenberg, V. Orlova, M. Mastrangeli, and P. M. Sarro, *Enabling actuation and sensing in organs-on-chip using electroactive polymers,* in *2020 3rd IEEE International Conference on Soft Robotics (RoboSoft)* (2020) pp. 530–535.

[2] D. Desmaële, M. Boukallel, and S. Régnier, *Actuation means for the mechanical stimulation of living cells via microelectromechanical systems: A critical review,* Journal of Biomechanics **44**, 1433 (2011).

[3] H. Zhang, Y. Bellouard, E. Burdet, R. Clavel, A.-N. Poo, and D. Hutamacher, *Shape memory alloy microgripper for robotic microassembly of tissue engineering scaffolds,* in *IEEE International Conference on Robotics and Automation, 2004. Proceedings. ICRA '04. 2004*, Vol. 5 (2004) pp. 4918–4924 Vol.5, iSSN: 1050-4729.

[4] P. Dineva, D. Gross, R. Müller, and T. Rangelov, *Piezoelectric Materials,* in *Dynamic Fracture of Piezoelectric Materials: Solution of Time-Harmonic Problems via BIEM*, Solid Mechanics and Its Applications, edited by P. Dineva, D. Gross, R. Müller, and T. Rangelov (Springer International Publishing, Cham, 2014) pp. 7–32.

[5] F. M. Sasoglu, A. J. Bohl, and B. E. Layton, *Design and microfabrication of a high-aspect-ratio PDMS microbeam array for parallel nanonewton force mea-*

surement and protein printing, Journal of Micromechanics and Microengineering **17**, 623 (2007).

[6] M. A. Brady, R. Vaze, H. D. Amin, D. R. Overby, and C. R. Ethier, *The Design and Development of a High-Throughput Magneto-Mechanostimulation Device for Cartilage Tissue Engineering,* Tissue Engineering Part C: Methods **20**, 149 (2014), publisher: Mary Ann Liebert, Inc., publishers.

[7] N. J. Sniadecki, A. Anguelouch, M. T. Yang, C. M. Lamb, Z. Liu, S. B. Kirschner, Y. Liu, D. H. Reich, and C. S. Chen, *Magnetic microposts as an approach to apply forces to living cells,* Proceedings of the National Academy of Sciences **104**, 14553 (2007), publisher: Proceedings of the National Academy of Sciences.

[8] R. Balint, N. J. Cassidy, and S. H. Cartmell, *Conductive polymers: Towards a smart biomaterial for tissue engineering,* Acta Biomaterialia **10**, 2341 (2014).

[9] E. W. H. Jager, O. Inganäs, and I. Lundström, *Microrobots for Micrometer-Size Objects in Aqueous Media: Potential Tools for Single-Cell Manipulation,* Science **288**, 2335 (2000).

[10] S. Taccola, F. Greco, B. Mazzolai, V. Mattoli, and E. W. H. Jager, *Thin film freestanding PEDOT:PSS/SU8 bilayer microactuators,* Journal of Micromechanics and Microengineering **23**, 117004 (2013).

[11] A. Poulin, C. S. Demir, S. Rosset, T. V. Petrova, and H. Shea, *Dielectric elastomer actuator for mechanical loading of 2d cell cultures,* Lab on a Chip **16**, 3788 (2016).

[12] B. Bhandari, G.-Y. Lee, and S.-H. Ahn, *A review on IPMC material as actuators and sensors: Fabrications, characteristics and applications,* International Journal of Precision Engineering and Manufacturing **13**, 141 (2012).

[13] S. Hitsumoto, T. Ihara, and K. Morishima, *A Miniaturized Cell Stretching Tool using Ionic Polymer Metal Composites Actuator,* MRS Online Proceedings Library **1097**, 10970303 (2008).

[14] A. Miriyev, K. Stack, and H. Lipson, *Soft material for soft actuators,* Nature Communications **8**, 596 (2017), number: 1 Publisher: Nature Publishing Group.

[15] W. Liang, H. Liu, K. Wang, Z. Qian, L. Ren, and L. Ren, *Comparative study of robotic artificial actuators and biological muscle,* **12**, 1687814020933409, publisher: SAGE Publications.

[16] M. Shahinpoor, Y. Bar-Cohen, J. Simpson, and J. Smith, *Ionic Polymer-Metal Composites (IPMCs) as Biomimetic Sensors, Actuators and Artificial Muscles: A Review,* Smart Materials and Structures **7** (1998), 10.1088/0964-1726/7/6/001.

[17] K. J. Kim and M. Shahinpoor, *Ionic polymer metal composites: II. Manufacturing techniques,* Smart Materials and Structures **12**, 65 (2003).

[18] S. Nemat-Nasser, *Micromechanics of actuation of ionic polymer-metal composites,* Journal of Applied Physics **92**, 2899 (2002).

[19] W. MohdIsa, A. Hunt, and S. H. HosseinNia, *Active Sensing Methods of Ionic Polymer Metal Composite (IPMC): Comparative Study in Frequency Domain,* in *2019 2nd IEEE International Conference on Soft Robotics (RoboSoft)* (2019) pp. 546–551.

[20] S.-G. Lee, H.-C. Park, S. D. Pandita, and Y. Yoo, *Performance Improvement of IPMC (Ionic Polymer Metal Composites) for a Flapping Actuator,* , 8.

[21] S. Q. Liu, *Influence of Tensile Strain on Smooth Muscle Cell Orientation in Rat Blood Vessels,* Journal of Biomechanical Engineering **120**, 313 (1998).

3

An IPMC-based micropump platform: Towards OoC applications

Je suis riche de mes doutes.

Albert Camus

Parts of this chapter have been presented at the European Organs-on-chips Society (EUROoCS) Conference 2022 (Grenoble, FR) and are included in a publication in preparation.

In this chapter, another application of standard 180um-thick IPMC has been explored: an IPMC-based micropump for microfluidics in organ-on-chip. IPMC is integrated within a polymer membrane (polydimethylsiloxane) in order to realize an electronically-controllable flexible diaphragm. Two designs have been explored, involving non-moving part valves (Tesla and nozzle-diffuser) for micropumping. By this means, it is possible to avoid using a non-user-friendly, cumbersome pneumatics-based system, currently widely used in the OoC field. In addition, wafer-level microfabrication techniques have been investigated. Finally, a micropump platform has been manufactured using Tesla passive check valves and direct light printing-based manufacturing techniques. Simulations were performed using a lumped model capturing the analogy between electric and fluidic domains. Furthermore, a hydrogel-based channel was integrated within the microfluidic circuit in order to reproduce a compliant visco-elastic microenvironment, mimicking a vascular network. A pulsatile flow rate (1ul/min) has been achieved with the Tesla valve design, which is biologically relevant giving a wall shear stress of 0.008 Pa.

3.1. Introduction: microfluidics for Organ-on-chip

Driving fluids within a cell culture chamber always has been a key aspect of OoC technology, as perfusion has been reported to be crucial in cell biology in order to mimic a realistic cell microenvironment [1–5]. Coluccio *et al.* reviewed the parameters of the microenvironment that can be influenced by microfluidics for cell culture applications as well as the different techniques that can be implemented to pump fluids inside a microfluidic cell culture [2]. Controlling fluids at the microscale allows the user to precisely sway shear stress over the cells' culture, control fresh medium refilling, and monitor CO_2 level, oxygen level as well as gradients of molecules of interest (Figure 3.1).

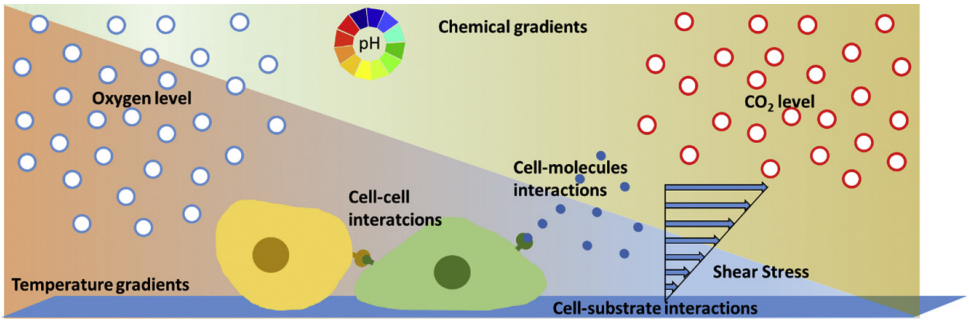

Figure 3.1: The cell microenvironment consists of physical (shear stress), biochemical (cell interactions), and physio-chemical (pH, CO_2, temperature, O_2) factors. Extracted from [2].

Among the different factors, the mechanical cues induced by microfluidics can be sorted by the type of flow as laminar, pulsatile, or interstitial flow [4]. The mechanical cues that need to be provided to the tissue strongly depend on the tissue

type, disease or model studied as well as the design of the chip (e.g. integrating hydrogel, membrane) and are non-exhaustively reported in Table 3.1.

Table 3.1: Summary of different types of mechanical stimuli and delivering mechanisms towards various organ/tissue models and their applications. Adapted from [4].

Mechanical stimuli	Delivery method	Organ Tissue model	References
Laminar flow	Gravity-driven	Liver	[6]
Laminar flow	Pressure controller	Liver	[7]
Laminar flow	Syringe pump	Kidney	[8]
Pulsatile flow	Peristaltic on chip	Blood vessel	[9]
Pulsatile flow	Syringe pump	Blood vessel	[10]
Pulsatile flow	Pneumatic pump	Blood vessel	[11]
Interstitial flow	Peristaltic	Breast cancer	[12]
Interstitial flow	Hydrostatic	Brain cancer	[13]
Interstitial flow	Hydrostatic	Blood vessel	[14]

3.1.1. Vasculature

Among different applications for organ-on-chip, one of the most relevant is the vascular network. As reviewed by Pollet and den Toonder, the vascular network is very complex and challenging to reproduce in-vitro [15]. The vasculature tree can be distinguished into 2 different sub-types, the venous system and the arterial system [15], and exhibits different flow regimes and profiles depending on the type of vasculature (Table 3.2). The arterial system which provides fresh blood to the organism exhibits a pulsatile behavior (systolic and diastolic pressure) with high blood flow velocity while the venous system shows no pulsatile behavior. Arterioles and capillaries exhibit slow velocities to improve the exchange of molecules of interest between the organs and the vascular system. Interestingly, the integration of pumping solutions to achieve relevant pulsating flowrate in a hydrogel channel remains challenging and poorly explored because of the inherent complexity in the context of vasculature-on-chip as reported by Sato and Sato [16].

Table 3.2: Summary of characteristic dimensions, blood flow velocities, and pressure for the different parts of the vascular tree. Adapted from [15].

Parameter	Elastic arteries	Muscular arteries	Arterioles	Capillaries	Venule	Vein
Diameter	2.5-1cm	0.3mm-1cm	300-10um	10-5um	8-100um	100um-2cm
Pressure (S:Systolic, D: Diastolic)	120S/90D (mmHg)	110S/80D (mmHg)	80S/60D (mmHg)	30 (mmHg)	15 (mmHg)	10 (mmHg)
Blood flow velocity	50-45 $cm.s^{-1}$	45-20 $cm.s^{-1}$	20-5 $cm.s^{-1}$	5-0.03 $cm.s^{-1}$	5-10 $cm.s^{-1}$	10-30 $cm.s^{-1}$

3.1.2. Pumping solutions

Many different approaches have been used to drive fluids within a microfluidic device for cell culture. For instance, syringe pumps (using a threaded tube connected to a step motor), gravity-based systems (rocking platform), pressure-based systems (using pressure controller), braille pins (using electronically controlled pins), centrifugal pumps (spinning disk), pressure-based peristaltic pumps (using time-scheduled valves) have been reported in literature [17, 18]. Unfortunately, most of the widely used pumping systems in organ-on-chip such as pressure-based, syringe-based or gravity-based systems hamper the versatility and ease of use, which has been reported as a crucial unmet need [19]. Many different other approaches and materials can be used as alternatives to pumping fluid inside a microfluidic chamber[20, 21]. Recently ionic electroactive polymer (i-EAP) has been reported to be an outstanding candidate material for pumping [22–24]. Ionic electroactive polymers such as IPMC present the benefit of using the ions naturally present in most of the culture media used in OoC such as sodium cations, and offer the possibility to integrate the moving diaphragm close to the microfluidic circuitry.

Annabestani and Fardmanesh published a very interesting review on micropumps made of electroactive polymer [22], as well as Sideris and de Lange [25]. It has been reported that most of the applications of IPMC in microfluidics are actually micropumps (Figure 3.2). Annabestani and Fardmanesh also reviewed the different shapes used in the micropumps developed with IPMC, showing that the most used shape is actually the disk (Figures 3.3).

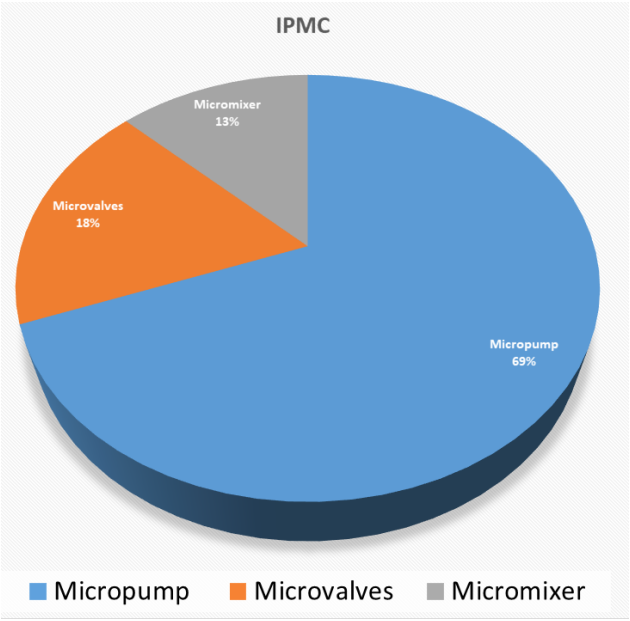

Figure 3.2: Types of microfluidic devices manufactured with IPMC. Adapted from [22].

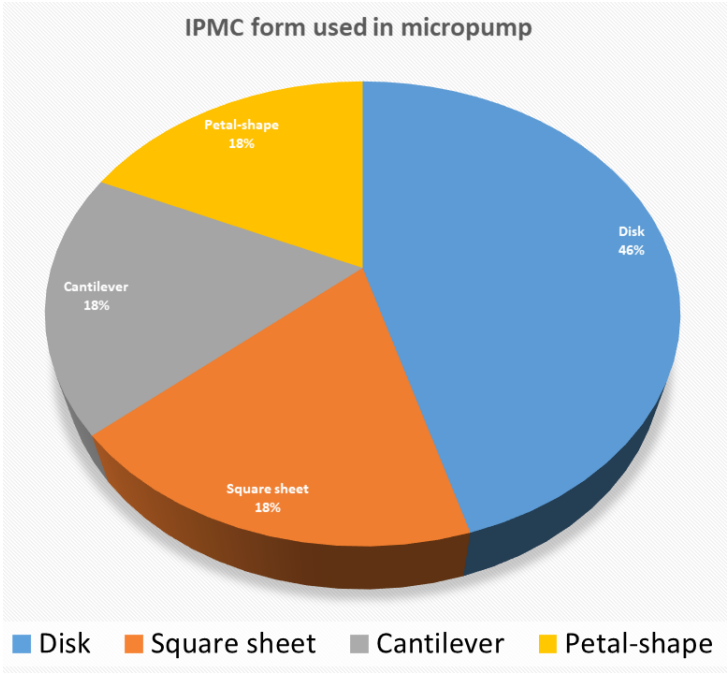

Figure 3.3: The shape of IPMC used for micropumps. Adapted from [22].

Previous work already outlined the possibility to manufacture an IPMC-based micropump [26–32]. In the aforementioned articles most of the authors used either a design including moving part (MP) valve such a flap valves [30], or non-moving part valve (NMP) such as nozzle-diffuser [31]. In all cases, the pumping systems were not used for any specific applications. Santos *et al.* used an acrylic plate clamp in between the IPMC diaphragm to build the pump [31] while Nguyen *et al.* used a polymethyl methacrylate (PMMA) plate also clamped with PDMS-IPMC diaphragm [30]. In both articles, the clamping leads to a non-robust device with possible leakage failure while the manufacturing technique offers little space for versatility. To the best of our knowledge, silicon-based as well as stereolithography-based IPMC micropumps have never been reported. In addition, the articles mentioned above [26, 27, 29–32] did not characterize the flow profile within the microfluidic circuitry (calculation of wall shear stress) precisely. The proper characterization of the flow profile is a crucial need for mechanobiology and OoC. Recently new approaches to manufacturing microfluidics have been outlined such as high-resolution 3D printing techniques [33]. The 3D printing of the microfluidic circuit offers versatility, and fast prototyping, and has been reported to be one of the ways to expand OoC toward easy-to-use devices [34]. Furthermore, lumped model for silicon-based devices implementing piezo actuator on top of silicon membrane has been reported in the literature [35], but never with a device using PDMS-IPMC-based flexible membrane showing different mechanical properties (Young'modulus) and actua-

tions range (amplitude and frequency). Finally, in the aforementioned articles, a relevant microenvironment for OoC application has not been integrated within the circuitry. To the best of our knowledge, an iEAP-based micropump offering the possibility of driving fluids in a viscoelastic vascular-like network with pulsatile behavior has never been reported.

3.2. Design of valveless microfluidic pump

Among different types of integrated micropumps previously reported, designs with no-moving parts (NMP) offer many advantages for OoC. NMP pumps first reported by Olsson *et al.* have been called "valveless micropumps" because of the absence of moving parts and were reviewed later [37, 38]. Interestingly the use of NMP valves has already been reported for biomedical applications, showing good potential [39, 40]. However, in the above articles, the actuation mechanisms were different, based on electromagnetic actuations. NMP-based (valveless) micropumps show a long life expectancy with limited mode failure because of the absence of moving parts that could show inherent defects such as mechanical fatigue. Additionally, NMP valves show a limited risk of clogging in comparison to moving valves such as check valves, which could be of crucial importance when studying biological models involving circulating cells such as blood cells or immune cells. Finally, micropump designs using fixed geometry such as Tesla valve and nozzle-diffuser valve have been reported to be compatible with wafer-scale fabrication, show ease of fabrication, and have been extensively made out of silicon and glass for their high integrability in an industrial environment [21]. Most of the no-moving part micropumps made of silicon are using piezoelectricity as an actuation mechanism. Fabrication relies on deep reactive ion etching as well as anodic bonding to close the circuit which gives the advantage to obtain a very reliable circuit, resistant to harsh environments, and optically transparent. The main drawback of using a piezoelectric system is the high voltage and materials used which can both potentially lead to changing the conditions of culture for an OoC application. In this work, design parameters for the Tesla valve and the nozzle-diffuser valve have been chosen to maximize the flowrate for the targeted application (vasculature) as well as including geometrical constraints (integration on a wafer for the nozzle-diffuser micropump as well as ease of use for the Tesla).

3.2.1. Nozzle-diffuser valve

The ease of fabrication and relative simplicity of the nozzle-diffuser valve make it attractive for OoC applications. The nozzle-diffuser valve is a type of valve that consists of a narrowing channel (nozzle) and an expanding channel (diffuser). The diodicity of the valve relies on the pressure imbalance between the inlet and outlet created inside the pumping chamber which is placed between the nozzle and the diffuser (Figure 3.4). When the membrane in the chamber is pushed downwards (pumping mode) the speed of the liquid inside the nozzle will increase, on the contrary, the diffuser has a higher fluidic resistance than the nozzle. Accordingly, when the pressure is applied in the pumping chamber, a higher volume will go

toward the outlet than toward the inlet. Conversely, when the membrane moves upwards (supply mode) the nozzle becomes the diffuser and the diffuser becomes the nozzle, therefore a higher volume of liquid goes inside the pumping chamber (Figure 3.4).

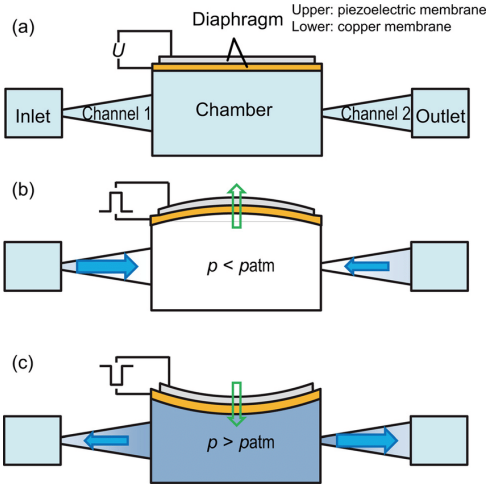

Figure 3.4: Working principle of the nozzle-diffuser valve. The pump is represented (a). Upon application of a pressure difference inside the pumping chamber, the flow will be sucked from the inlet (b) and pushed towards the outlet (c). Extracted from [41].

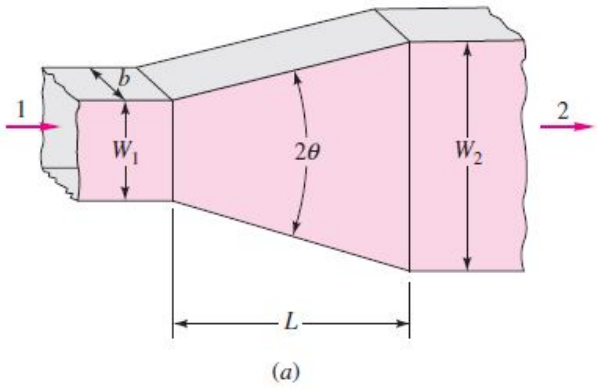

Figure 3.5: Flat wall diffuser geometry. Extracted from [42].

The nozzle-diffuser valve design relies on several parameters: the inlet width (W1), the outlet width (W2), the length (L) of the nozzle, and finally the angle of the expanding channel (2θ) (Figure 3.5). As explained by White [42], a stability map can be reported for flat wall nozzle diffuser valve depending on the design

parameters, with L/W1 in abscisses and (2θ) in ordinate (Figure 3.6). In Figure 3.6 C_p refers to the efficiency of the pump and is explained in more detail in Section 3.4 according to the dimensions of the flat wall diffuser valve. There are four basic regions in the map. Below the line "aa" there is steady viscous flow, no separation of the jet flow, and moderately good performance. A very short diffuser will separate the flow, or stall if its half-angle is greater than 10 °. Between lines "aa" and "bb" is a transitory stall pattern with a strongly unsteady flow. The best performance (highest Cp) occurs in this region. The third pattern, between "bb" and "cc", is a steady bistable stall from one wall only. The stall pattern may flip from one wall to the other, and performance is poor. The fourth pattern, above line "cc", is jet flow, where the wall separation is so gross that the mainstream ignores the walls and simply passes. Performance is extremely poor in this region.

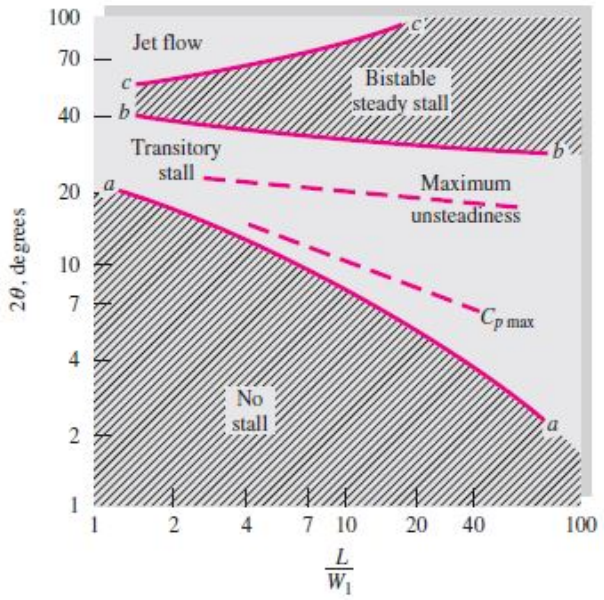

Figure 3.6: Typical flow regimes for a flat wall nozzle diffuser depending on the design parameters. Extracted from [42].

Finally, the footprint of the nozzle-diffuser valve has been kept to 18 by 9 mm^2 in order to fit 32 chips per 4-inch wafer. The device includes a culture chamber that fits a well of a standard 96 well-plate (diameter of 6.94mm). The nozzle has been designed with the following parameters L=3.5mm, W1=0.08mm, W2=0.57mm, θ=5 °and fit in a region with maximum efficiency (Figure 3.6); the pumping chamber is set to a diameter of 3.5mm. The final design of the silicon-based nozzle diffuser-based chip can be seen in Figure 3.7.

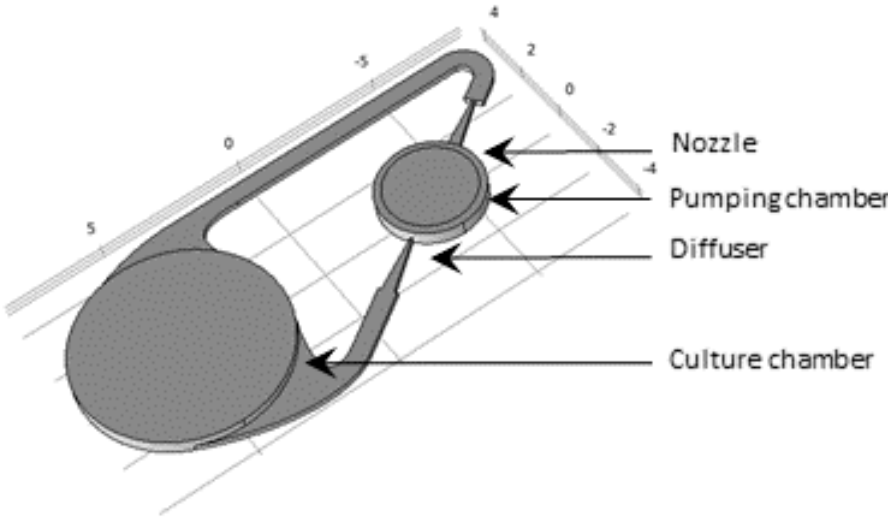

Figure 3.7: Design of the nozzle-diffuser microfluidics for the silicon-based chip. The scale is in mm. The micropump is 18mm long and 9mm wide. The diameter of the pumping chamber is 3.5mm, while the diameter of the culture chamber is 6.94mm.

3.2.2. Tesla valve

The Tesla valve has been named after his inventor Nikola Tesla who was awarded a U.S. Patent in 1920 for its invention. The Tesla valve is a passive valve that consists of a microfluidic channel with a "wing-shaped" structure inserted in the channel. The flow in one direction will experience low resistance from the channel duct, while in the other direction (reverse flow), the flow will experience maximum resistance with some of the liquid being directed toward the incoming flow. This way there is a total net flow going from the inlet toward the outlet (Figure 3.8). The Tesla valve also has been reported in the literature as a good candidate because of its ease of fabrication as the steps can be similar to the ones used for the nozzle diffuser fabrication.

The Tesla valve has been designed as follows. For ease of manufacturing and handling the footprint chosen is the one of a standard microscope coverslip (square of 22x22mm^2). The angle of the diverging channel in the Tesla valve has been set to 45 °, giving the maximum reverse flow and therefore highest diodicity. Two Tesla valves have been positioned one after the other to maximize the net flow. The dimension of the pumping chamber has been set to 8mm, which is the maximum size complying with the requirement of the coverslip size and enough space should be left from the edge to avoid breaking. Additionally, the circuit has been designed in order to leave an 8mm-long channel for the hydrogel to be inserted. The size of the channel is 200um in height with 108um in width, which fits the requirements of arterioles (Table 3.2) and the dimensions of pixels when using a stereolithography printer (27um wide for 20 um tall). The final footprint of the pump can be seen in

Figure 3.23.

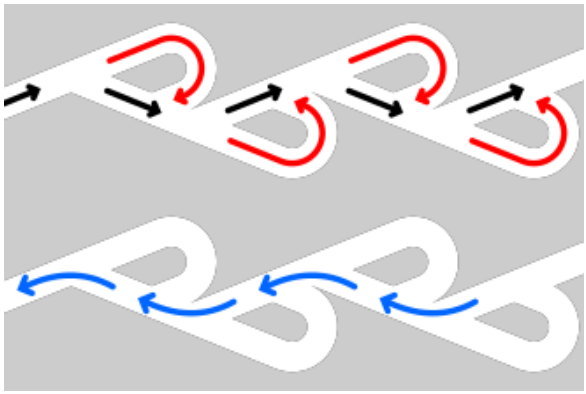

Figure 3.8: Working principle of the Tesla valve. The upper figure shows flow in the blocking direction: at each segment, part of the fluid is turned around (red) and interferes with the forward flow (black). The angle of the diverging channel is 45 °, which corresponds to the highest diodicity. The lower figure shows flow in the unimpeded direction (blue).

3.3. Device fabrication

Two main approaches have been investigated in order to manufacture an IPMC-based micropump using NMP valves. The first one, based on microfabrication technology and nozzle-diffuser design, was made out of silicon and glass. Unfortunately, the resulting device was not usable and was mostly limited by the difficulties of integrating the IPMC within the device together with the use of vapor etch, the last step of the manufacturing. However, the tests and experiences gained during the fabrication of the micropump are reported in order to help in the future any researchers who would like to continue exploring the implementation at wafer-level of IPMC for micro pumping applications. The second approach used high-resolution 3D printing (stereolithography) to fabricate micropumps including design with the nozzle-diffuser valve and the Tesla valve. This approach included the bonding of the micropump to a glass coverslip for optical transparency.

3.3.1. Silicon-based approach

In this part, the final flowchart that could lead to the fabrication of a silicon-based IPMC-driven micropump, where the microfluidic circuit is actually made of silicon covered on the sides with silicon oxide, is presented. The bottom of the chip is made of glass covalently bonded to the silicon wafer using anodic bonding. An IPMC-PDMS membrane is embedded on top of the manufactured microfluidic circuitry. Finally, the silicon membrane was meant to be released using xenon difluoride-based vapor etch to free the polymer-based membrane.

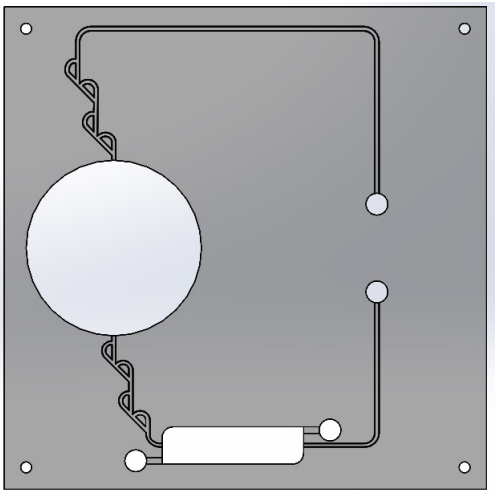

Figure 3.9: Design of the Tesla valve-based micropump, the footprint of the chip is 22X22mm^2, size of a standard coverslip. The Tesla valve has been designed with an angle of 45 °, giving maximum diodicity. An 8mm-long space is left at the bottom to allow the insertion of the hydrogel.

Flowchart

The manufacturing of the silicon-based micropump is based on deep reactive ion etching (DRIE). DRIE makes use of repetitive depositions of a passivation layer and etching of silicon through the creation of plasma, making it possible to create high-aspect-ratio structures within the silicon such as microfluidic channels. This process is also known under the name "Bosch process" [43]. Additionally, the microfluidic circuit is made hydrophilic through the deposition of silicon oxide on the walls of the channels. The silicon oxide is selectively etched thanks to a procedure using an anisotropic (dry) etch and an isotropic (wet) etch. Finally, the circuit is sealed through the anodic bonding of glass to close the silicon-based circuitry. A polymer-based membrane is deposited on top of the wafer and the membrane is released thanks to vapor etch. The detailed flowchart is explained in Appendix 7.4.

Briefly, a first silicon hard mask is deposited and patterned on the silicon wafer (Figure 3.10) (step 2) using standard photoresist and lithography. On top of this oxide mask, a second mask made of photoresist is deposited(Figure 3.10, step 3). This second mask could be used later for the 2 steps etch.

By two subsequent DRIE steps (4, 5, 6), it is possible to manufacture our structure which consists of a pumping chamber (Figure 3.11) connected to microfluidic circuitry (Figure 3.11).

The deposition of the silicon oxide inside the microfluidic circuit is made possible by growing thermal oxide isotropically on the silicon surface (Figure 3.12, step 8) and the use of anisotropic etching (reactive ion etching: step 10) of silicon oxide as well as isotropic etching of silicon oxide (wet etching: 12) (Figure 3.13). We obtained a final structure including silicon oxide inside the microfluidic circuitry (13) (for hydrophilicity and for protection from the last etch of the remaining silicon

Figure 3.10: . Cross-section view of the flowchart for the silicon-based micropump and microfluidics steps 1, 2 3. Black: silicon, yellow: silicon oxide, red: photoresist.

Figure 3.11: . Cross-section view of the flowchart for the silicon-based micropump and microfluidics, steps 4, 5, 6. Black: silicon, yellow: silicon oxide, red: photoresist.

membrane) as well as a smooth surface for the anodic bonding (step 13) (Figure 3.13). PDMS is spin-coated on the silicon side of the wafer. The laser-cut IPMC beam is then integrated into the uncured PDMS layer and left at room temperature in a moisture-rich environment for 72 hours and later protected by a layer of photoresist (14). In the end, the IPMC-PDMS membrane is eventually released using xenon difluoride (XeF2), a gas that is selective to silicon and that will keep the silicon oxide intact (15). The XeF2 etch has been performed at the MESA+ institute of the University of Twente.

Interestingly the 2-step etch showed very good results with the nozzle-diffuser geometry nicely defined as shown in (Figure 3.15). Unfortunately, the final step of the flowchart which consists of releasing the membrane by performing a xenon

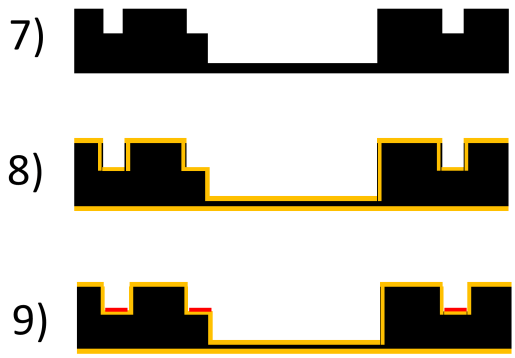

Figure 3.12: Cross-section view of the flowchart for the silicon-based micropump and microfluidics. Steps 7,8,9. Black: silicon, yellow: silicon oxide, red: photoresist.

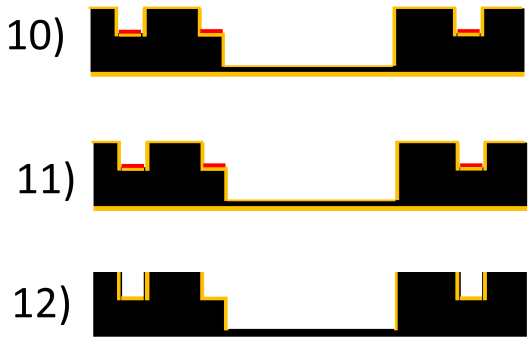

Figure 3.13: Cross-section view of the flowchart for the silicon-based micropump and microfluidics. Steps 10, 11, 12. Black : silicon, yellow: silicon oxide, red: photoresist.

difluoride etch could not be optimized, the vapor etch was not homogeneous and is very dependent on the volume that can enter the microfluidic circuit. Even after 2 hours and a half the membrane was still not released as shown (Figure 3.16).

To solve this issue it could be possible to thin down (100 μm-thick) the membrane prior to the bonding (during the second DRIE). However, during the bonding, which is done under vacuum, the membrane tends to bend because of the pressure difference between the chamber and the inside of the chip (Figure 3.17). A thinner membrane could lead to fracture while bonding. An optimum might be possible to find between the thickness of the membrane, the pressure applied during the bonding and the xenon difluoride etch parameters. Also, the anodic bonding perfectly withstands the presence of the microfluidic channels, as the resulting wafer

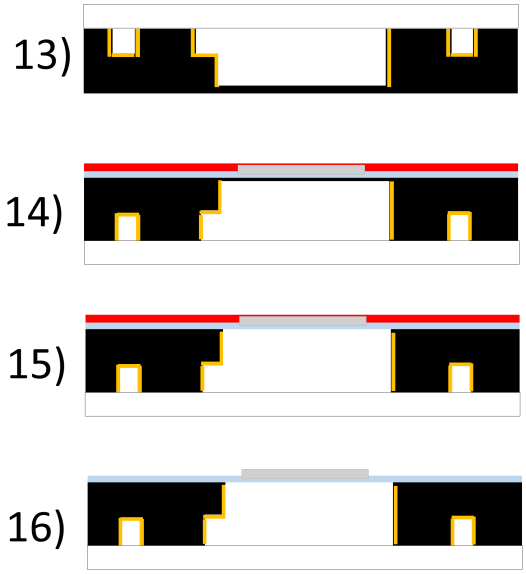

Figure 3.14: . Cross-section view of the flowchart for the silicon-based micropump and microfluidics; Steps 13, 14, 15, 16. Black: silicon, yellow: silicon oxide, red photoresist, white: glass, blue: PDMS, Grey: IPMC.

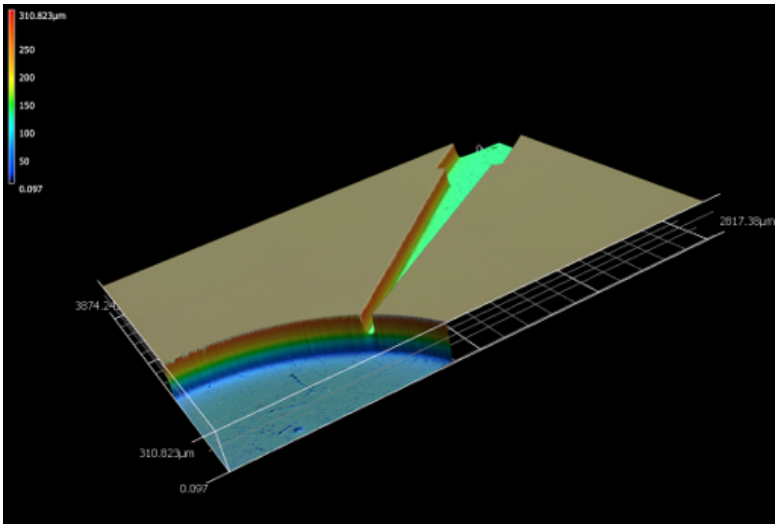

Figure 3.15: 3D view of the 2-step DRIE etch for the micropump with a focus on the intersection of the nozzle and pump chamber.

showed no detachment all over the wafer despite the presence of different struc-

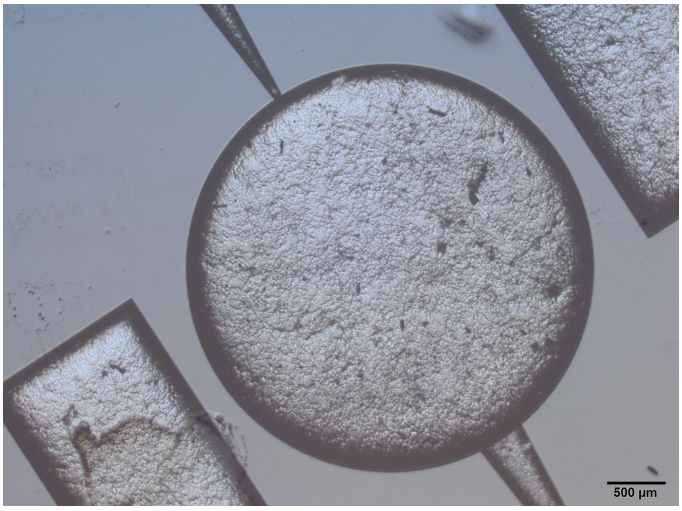

Figure 3.16: Close view of the pumping chamber after 2h30' of XeF2 etch. The membrane could not be released.

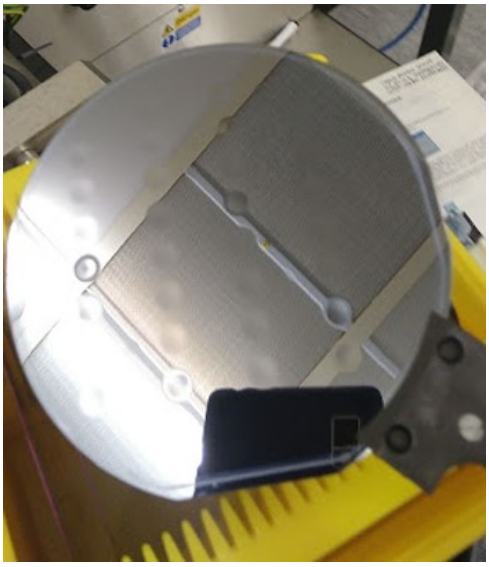

Figure 3.17: Frontside view of the wafer after the anodic bonding of glass. The membranes are deformed because of the vacuum.

tures (Figure 3.18). Anodic bonding is known for giving very robust microfluidic devices that could be used for instance in harsh environments with no side effect [44].

The high-quality bonding between the glass wafer and the silicon wafer was confirmed by SEM imaging, which also highlighted the 2-step etch and the PDMS

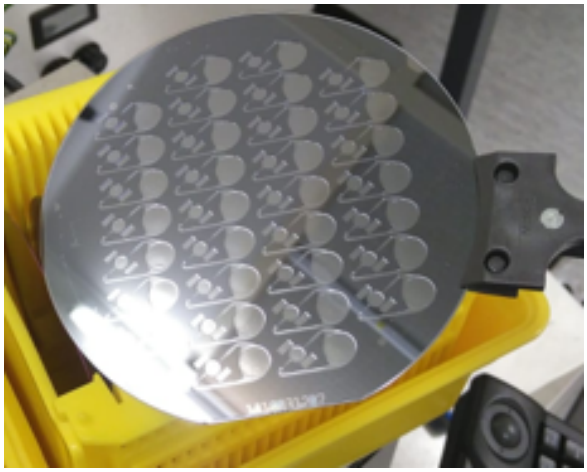

Figure 3.18: Backside view of the wafer after the anodic bonding (glass side).

on the silicon membrane (Figure 3.19).

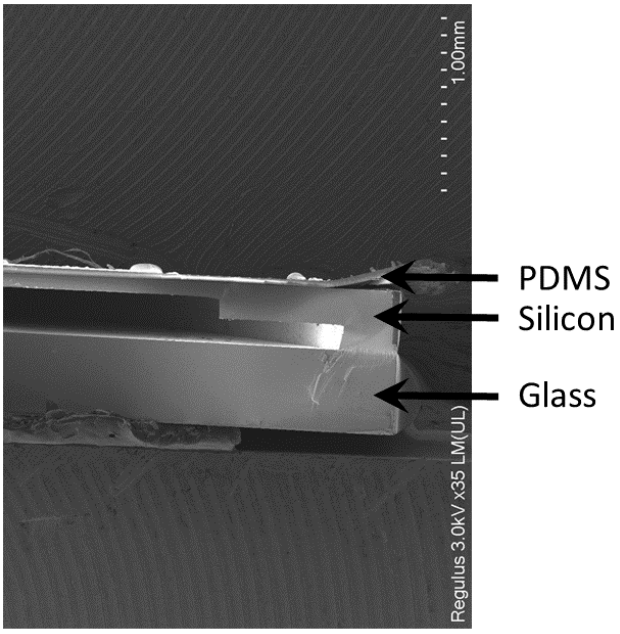

Figure 3.19: Cross-section of the silicon-based micropump; The 2 steps DRIE of silicon can be seen as well as the seamless bonding with glass. On the opposite side, the PDMS layer can be seen.

Integrating IPMC within a wafer level fabrication flow

Integrating IPMC within a wafer-level fabrication flow is very challenging because of the inherent properties of Nafion (high water uptake and solvent permeability). Therefore the use of any solvent or water will lead to the absorption of the chemical components by the PFSA material. However, some attempts have been made in order to explore ways to integrate the IPMC within the process flow. Briefly, after the first tests it became obvious that the IPMC needed to be embedded in a more stable material to be further processed. In Figure 3.20 we can see that the IPMC was embedded in between two polymers, on the bottom the PDMS and on top a positive resist (AZ10xt). We realized that the IPMC was prone to release water leading to repellence of the moisture-sensitive resist (Figure 3.20).

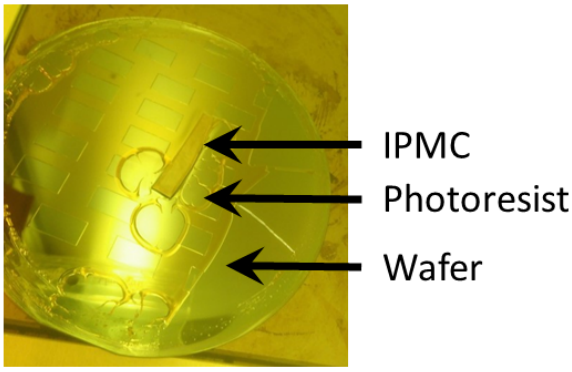

Figure 3.20: Attempt at embedding IPMC in between two layers of polymers (positive resist AZ10xt and PDMS). The water released by the IPMC can be seen as it repeals the photoresist.

To overcome the issue of water being released by the IPMC, we used small pieces of IPMC and dried them by putting the IPMC in the oven at 100 °C for 15mins. While doing so, the IPMC sample had to be kept in between two holders to avoid shrinking of the sample. Afterward, the IPMC was embedded as soon as possible in the uncured PDMS layer and the photoresist was spin-coated. This encapsulation of the IPMC was found to work efficiently. Interestingly the same approach can be used to manufacture the PDMS-IPMC-based membrane. The IPMC is kept in a moisture-rich environment at room temperature on the uncured PDMS for 72 hours. Once cured, the PDMS-IPMC membrane can gently be peeled off the silanized wafer. IPMC encapsulation has been already used in previous work [45], Bhattacharya *et al.* mentioned the use of PDMS to encapsulate the IPMC and avoid shrinkage while exposed to different moisture environments. In addition, we can mention the work of Tsuchitani *et al.* and Feng and Chen who studied the manufacturing of IPMC by using standard MEMS-specific microfabrication techniques with a focus on implementing the fabrication of IPMC on a Si substrate [46, 47]. They were able to manufacture a μ-IPMC by casting Nafion solution in a mold. This approach also has been investigated by us, however, the liquid Nafion is even less stable than

commercially available Nafion sheets, thus the casting approach was not possible as the liquid Nafion was detaching from any surface and final encapsulation was not possible.

Ion miling

In addition to the encapsulation of IPMC for processing the material in a clean room environment, another approach has been investigated. The concept is to encapsulate the IPMC in a photoresist and pattern the photoresist in order to pattern the IPMC sample as usually done to pattern standard metal with microfabrication techniques. As the IPMC contains platinum (noble metal) on the surface, it is not possible to etch it with standard reactive ion etching (RIE) and the use of ion milling is therefore needed. In addition, the use of standard RIE requires the use of a stable environment for plasma generation which is hardly achievable with Nafion, known to release solvent when dried. Ion milling consists of bombarding the surface with argon ions projected at high speed toward the sample. Some tests have been performed using Kapton tape (polyimide) as a mask. After 2 hours of ion milling only a very little portion of IPMC had been etched. In addition, tests have been made with standard positive resist for metal patterning, and ion milling tended to burn the resist because of the heat induced by the bombardment of ions.

3.3.2. Direct light printing

The final approach which has been investigated for the manufacturing of an IPMC-based micropump is direct light printing (DLP). DLP (or high-resolution 3D printing) consists of using a UV-sensitive resin illuminated by a LED-based UV source. Layer after layer, complex structures can be printed (Figure 3.21). The main advantage of using direct light printing is the ease of fabrication, cost, and fast manufacturing [48]. However the main hurdle is that the technique is hardly scalable to mass production. Ultimately, simple chips manufactured with this technique could be further industrialized using for instance injection molding or hot embossing. The OoC itself is made of a microscope cover slip, a double-side biocompatible tape (pressure sensitive adhesive, PSA), laser cut with a high-precision laser (Optec Microsystem), a microfluidic circuit printed with a high-resolution stereolithographic printer (Asiga Max), another layer of laser cut biocompatible adhesive and finally a PDMS diaphragm that embeds the IPMC (Figure 3.22). The diaphragm membrane including the IPMC and the PDMS layer has been manufactured as follows. A silanized wafer has been used to spin coat PDMS at 2500 rpm, giving a thickness of 40 μm. IPMC has been deposited on the uncured PDMS and kept at 60 C° under a moisture-rich atmosphere to avoid shrinkage of the IPMC. Once completely cured the IPMC-PDMS diaphragm has been gently peeled off and cut with a razor blade from the wafer to be bonded to the rest of the chip using pressure-sensitive adhesive (PSA).

The microfluidic system is made of a chamber on which a PDMS membrane is actuated, the chamber is connected to the microfluidic channels using the two Tesla valves (Figure 3.23).

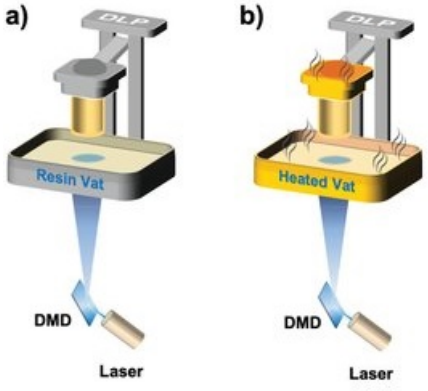

Figure 3.21: Working principle of direct light printing, a photo-sensitive resin is polymerized by incoming light in a shape of an image. The device is printed layer after layer along the vertical direction. The bath containing the resin can be conventional (a) or heat assisted (b). A digital micromirror device (DMD) is used to control the incoming light. Extracted from [48].

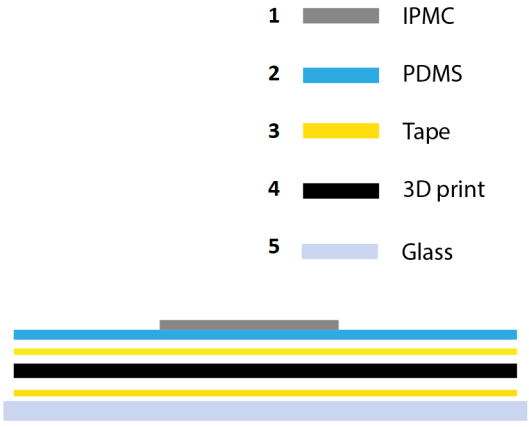

Figure 3.22: Cross-section view of the micropump manufactured with direct light printing.

3.4. Lumped model and simulation

Computational fluid dynamics (CFD) relies on the meshing of geometries and heavy computational capabilities. It is relevant for the microscopic model including multiphysics for comparative study. However, it proved hard to be extensively used in order to develop a reliable model of the full microfluidic system. CFD will be used for studying the most important part of the pump, the NMP valve, and more precisely the efficiency of the nozzle-diffuser. To model the full microfluidic system

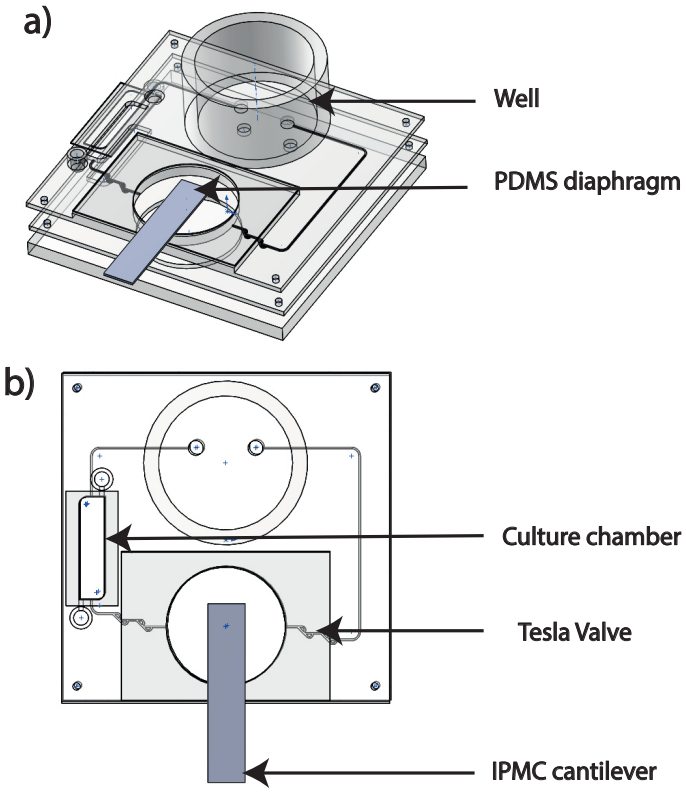

Figure 3.23: CAD view of the micropump a) 3/4 view of the micropump platform, b) top view of the micropump platform.

and its frequency response in this case we found it convenient to use a lumped model since as reported in literature it can give a good fit with experimental data [49]. The analogy between the electrical domain and fluidics already has been used to develop an equivalent circuit in order to simulate fluid behavior in a micropump [49–51]. However, the aforementioned works used a silicon-based micropump with a piezoelectric actuator [51]. Those models show low displacement of the moving diaphragm as well as higher rigidity of the material used for the diaphragm unlike what could be achieved with IPMC. To the best of our knowledge, this is the first time that a lumped model has been developed for a soft, flexible, PDMS-iEAP-based micropump. Accordingly, the model provides different mechanical responses because of the inherent high flexibility of the membrane (higher capacitance and inertance) as well as different frequency response as the frequency range of piezoelectric differs a lot from the frequency response of an IPMC. The lumped model consists of discrete components, defined using analogies between the electrical domain and fluidic domain to represent the full microfluidic system as an electrical circuit, which can be used to measure the frequency response of the system as well as pres-

sure and flow rate at different points of the system. The equivalences between electricity and microfluidics are summed up in Table 3.3 as reported by Morganti *et al.* [35] and mostly rely on the analogy voltage-pressure and flowrate-current. Hydraulic resistance can be simply simulated with an electrical resistance while the inertia (due to speed increase) can be simulated using an inductance (inertance in the fluidic domain). The elastic behavior of any part of the system (pumping chamber filled with water or PDMS membrane, for example) can be simulated through a capacitance that has the ability to store and deliver energy.

Table 3.3: The equivalences between electrical parameters and hydraulic parameters. Adapted from [35].

Fluidic quantity	Parameter	Unit	Electric quantity	Parameter	Unit
Pressure	P	Jm^{-3}	Voltage	V	JC^{-1}
Flow	ϕ	m^3s^{-1}	Current	I	Cs^{-1}
Resistance	R_{hyd}	Jsm^{-6}	Resistance	R	JsC^{-2}
Inertance	I_{hyd}	Js^2m^{-6}	Inductance	L	Js^2C^{-2}
Capacitance	C_{hyd}	m^6J^{-1}	Capacitance	C	C^2J^{-1}

The hydraulic resistance represents the energy dissipation due to the effects of the fluid viscous friction against the component wall:

$$\Delta P = R_{hyd}\phi \tag{3.1}$$

The inductive behavior depicts the inertia of the liquid. The hydraulic inertance (I_{hyd}) complies with a mass being accelerated:

$$\Delta P = I_{hyd}\frac{\mathrm{d}\phi}{\mathrm{d}t} \tag{3.2}$$

The hydraulic capacitance (C_{hyd}) depicts the elastic behavior of the system. As for the inertance, the term can either refer to the capacitive behavior of the liquid or the membrane. For instance, for the liquid, it links pressure difference to volume variation :

$$C_{hyd} = \frac{\mathrm{d}V}{\mathrm{d}P} \tag{3.3}$$

3.4.1. Nozzle-diffuser valve

Olsson *et al.* developed a lumped model of the nozzle diffuser micropump with an equivalent electrical circuit [51]. The resistance of the chamber has been considered as well as the capacitance of the outlet part, and that of the inlet part has been neglected (incompressible liquid). As explained earlier, extracting the NMP valve efficiency requires running a CFD simulation of the nozzle diffuser as reported by White [42](Figure 3.24).

The parameter to assess the efficiency of the diffuser is the pressure recovery coefficient C_p defined as :

$$C_p = \frac{p_e - p_i}{p_{0t} - p_i} \tag{3.4}$$

Where p_e and p_i mean the exit pressure and the inlet pressure respectively. Higher C_p means better performance. As reported by White [42] we can correlate the performance in term of area ratio $AR = \frac{A_2}{A_1}$. Where A_1 corresponds to the cross-section of the input of the nozzle and A_2 of the output.

$$C_p = 1 - (AR)^{-2} \tag{3.5}$$

It has been reported that C_p values don't match with experimental data when flow separation happens (stall). The viscous boundary layer breaks away from the wall and reduces the performance of the pump [42]. Only CFD can predict this behavior and compute the efficiency of the pump in a reliable way.

Table 3.4: Used dimensional parameters for the lumped model of the nozzle diffuser.

Parameter	Description
Q_{pos}	Positive flow (nozzle)
Q_{neg}	Negative flow (diffuser)
2a	width of rectangular channel
2b	height of rectangular channel
l	length of the nozzle diffuser
Lv	valve length
A	cross sectionnal area of the channel
S	membrane area
h_c	height of the chamber
ρ	water density
μ	water viscosity
K	water compressibility
γ	Cosinusoidal flexion
ν	membrane Poisson ratio (PDMS)
E	membrane Young's modulus (PDMS)
rm	membrane radius
m	membrane mass
h	membrane thickness

The recovery factor can also be called efficiency, the efficiency is used to model the full microfluidic part in the lumped model.

$$\epsilon = \frac{-(Q_{pos} - Q_{neg})}{Q_{pos} + Q_{neg}} \tag{3.6}$$

For a given design of the nozzle diffuser, a certain efficiency is calculated. As one can expect efficiency strongly depends on the pressure drop along the NMP valve, therefore having a precise idea of the pressure in the chamber is key. To model the full microfluidic system we need to give an electric equivalent for all the parts of the system which are involved. The microfluidic system is made of a chamber on which a PDMS membrane is actuated, the chamber is connected to the microfluidic channels using the two nozzle diffuser valves. For calculation of the hydraulic resistance the following equation 3.7 has been used, which is the first-order approximation of hydraulic resistance for a rectangular cross-section channel [52].

$$R_{channel} = \frac{4\mu l}{ab^3}\left(\frac{16}{3} - 3.36\frac{b}{a}\left(1 - \frac{b^4}{12a^4}\right)\right)^{-1} \tag{3.7}$$

The inertance of a rectangular channel is depicted as follows:

$$I_{channel} = \rho\frac{l}{A} \tag{3.8}$$

The chamber is filled with liquid and its resistive behavior is neglected in comparison to its capacitive behavior. Using compressibility of water (K).

$$C_{chamber} = \frac{Sh_c}{K} \tag{3.9}$$

The liquid in the chamber also has some inertia.

$$I_{chamber} = \frac{\rho h_c}{S} \tag{3.10}$$

We consider a PDMS membrane actuated by an IPMC embedded in the bulk PDMS. The moving membrane gives a capacitive effect on the entire system:

$$C_{membrane} = \frac{(\gamma S)^2}{k} \tag{3.11}$$

The membrane also has inertia and therefore needs an inertance to model it:

$$I_{membrane} = \frac{m}{(\gamma S)^2} \tag{3.12}$$

The actuator is represented by a sine wave voltage generator.

For the above equations, the following spring constant of a circular membrane has been used:

$$k = \frac{64}{12(1-\nu^2)}\frac{\gamma\pi E h^3}{(rm)^2} \tag{3.13}$$

The NMP valve (nozzle diffuser) can be modeled as a changing resistance in series with a changing inertance. The inertance and the resistance change accordingly to the direction of the flow (nozzle or diffuser).

To calculate the resistance of the diffuser (R_{pos}) the value of the resistance of a microfluidic channel (Eq. 3.7) is integrated along nozzle-diffuser valve length. 2α refers to the width of the nozzle at position x, x being the beginning of the nozzle and Lv the length of the nozzle. The dimension of the nozzle can be found in Section 3.2.

$$\int_0^{Lv} \frac{4\mu l}{\alpha b^3}\left(\frac{16}{3} - 3.36\frac{b}{\alpha}\left(1 - \frac{b^4}{12\alpha^4}\right)\right)^{-1} dx \tag{3.14}$$

$$\alpha = \frac{(570 - 80)}{3500}x + 80 \tag{3.15}$$

The efficiency of the nozzle-diffuser correlates to the inertance and resistance of the nozzle with respect to the diffuser thanks to the efficiency factor ϵ (Eq. 3.6). The flow is considered as positive in the diffuser mode Q_{pos} and negative in the nozzle mode Q_{neg}, therefore the resistance and inertance of the nozzle, respectively R_{neg} and I_{neg}, are higher than the resistance and inertance of the diffuser R_{pos} and I_{pos}.

$$R_{neg} = \frac{1 - \epsilon}{1 + \epsilon}R_{pos} \tag{3.16}$$

$$I_{neg} = \frac{1 - \epsilon}{1 + \epsilon}I_{pos} \tag{3.17}$$

As explained in the previous section there is no analytical solution to calculate the efficiency, only computational fluid dynamics can be used (Figure 3.24).

The final lumped model is represented in Figure 3.25 and the values computed using the given dimensions of the valves and the equations above are summed up in Table 3.5. The system of equations was solved using Matlab 2019 and lumped model was run through LT-Spice XVII. The design of the nozzle diffuser has been imported from Solidworks and implemented in Comsol. Single-phase laminar flow has been used and no slip has been set regarding the wall boundary conditions. A tetrahedral mesh with 1271017 domain elements was obtained using ”finer” predefined scale in Comsol Multiphysics. The result of the CFD runs through Comsol Multiphysics shows the efficiency of the nozzle diffuser to be 0.0064, with $Q_{neg} = 0.36355$ and $Q_{pos} = 0.35894$, in accordance with literature [42], with an inlet pressure ranging from 45 to 100mPa, pressure range typically used for microfluidics applications. The value of the efficiency has been used to estimate the resistance and inductance of the nozzle diffuser. To distinguish the pumping mode from the supply mode, diodes have been added to the lumped model (Figure 3.25), similar to the previous model existing in literature [35].

The first test of actuation of the prototyped nozzle-diffuser pump showed no diodicity despite the fact that water with micro-beads could clearly be seen moving inside the channel. Most probably the frequency range achieved by the IPMC was not sufficient to clearly drive the fluid within the channels as could have been

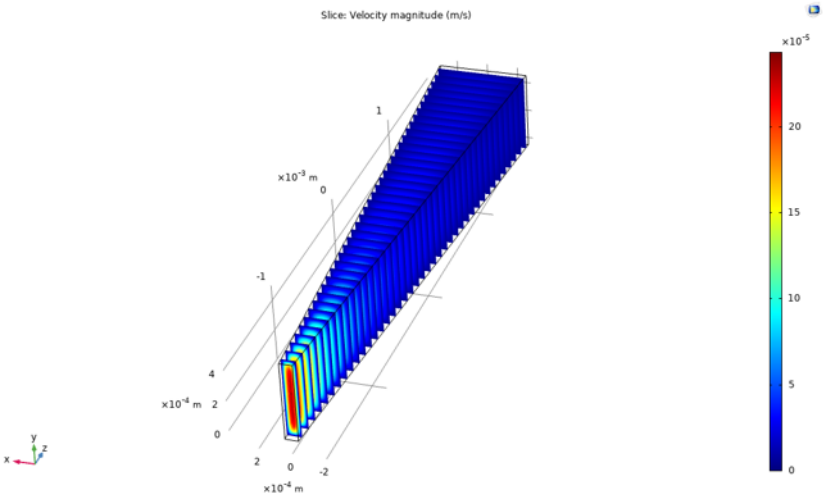

Figure 3.24: Velocity magnitude map (m/s) of the CFD simulation of the nozzle-diffuser valve for a 100mPa pressure input. The fluid speed increases at the narrowing channel. The simulation has been used to extract the efficiency of the NMP valve using the simulated flowrate Eq. 3.6.

Table 3.5: Table representative of the calculated parameters used for the lumped model of the micropump including the nozzle diffuser valves.

Symbol	Value	Definition
L_1	$5.601 \times 10^{1}\ N.s^2.m^{-5}$	Membrane Inductance
C_1	$2.58 \times 10^{-11}\ m^5.N^{-1}$	Membrane Capacitance
L_2	$1.27 \times 10^{4}\ N.s^2.m^{-5}$	Chamber Inductance
C_2	$2.23 \times 10^{-18}\ m^5.N^{-1}$	Chamber Capacitance
$L_3\ L_5$	$4.22 \times 10^{7}\ N.s^2.m^{-5}$	Nozzle Inductance
$R_2\ R_4$	$3.62 \times 10^{7}\ N.s.m^{-5}$	Nozzle Resistance
$L_4\ L_6$	$3.84 \times 10^{7}\ N.s^2.m^{-5}$	Diffuser Inductance
$R_3\ R_5$	$3.30 \times 10^{7}\ N.s.m^{-5}$	Diffuser Resistance
R_1	$1.52 \times 10^{10}\ N.s.m^{-5}$	Inlet channel Resistance
L_7	$5.74 \times 10^{7}\ N.s^2.m^{-5}$	Inlet channel Inductance
R_6	$1.52 \times 10^{10}\ N.s.m^{-5}$	Oulet channel Resistance
L_8	$5.74 \times 10^{7}\ N.s^2.m^{-5}$	Oulet channel Inductance

demonstrated with piezo-based pump [36]; The simulation of the lumped model of the nozzle diffuser confirms the lack of diodicity for the frequency range achieved (Figure 3.26). To overcome this issue a new design based on a Tesla valve was proposed, which was expected to better fit the frequency range response of the IPMC. A lumped model also has been devised for the microfluidic pump based on Tesla valves as well as proper characterization was performed.

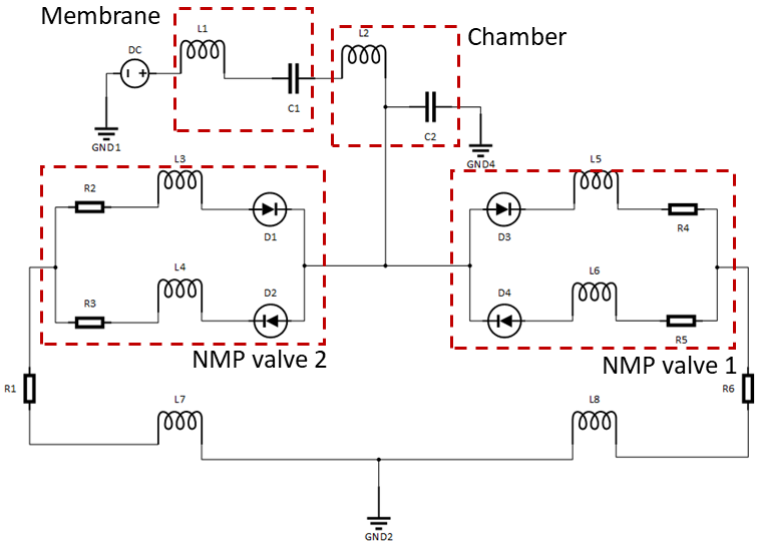

Figure 3.25: Lumped model of the microfluidic pump including nozzle-diffuser valves. The membrane is represented by an inertance in series with a capacitance. The liquid in the pumping chamber is represented through a capacitance and an inertance. The two NMP valves are represented by inertance in series with a resistance; To distinguish the diffuser from the nozzle, diodes are placed in accordance with the direction of the flow that refers to the nozzle or diffuser.

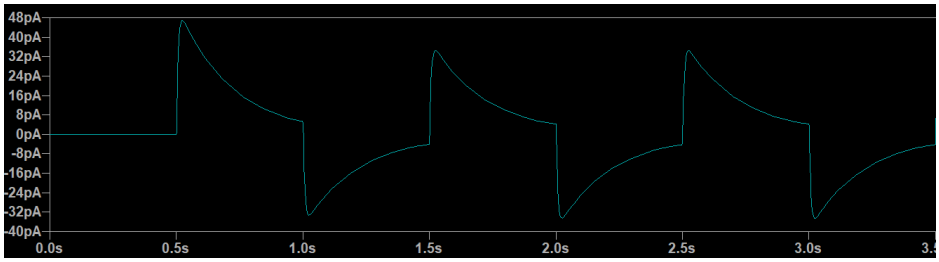

Figure 3.26: Result of the simulation in LT-Spice for the nozzle-diffuser pump (flow rate in the channel) at 1Hz actuation. nA in fluidic domain corresponds to μl/min. From the result of the simulation, no diodicity was found which could have been empirically confirmed. The simulation was meant to study the frequency responses and been fitted with empirical results. Higher frequencies should be used such as for piezo.

3.4.2. Tesla valve

The entire circuit can be separated into several parts, the 2 inlet and outlet channels, the pumping chamber, the actuating diaphragm, and the 2 NMP valves. Unlike for the nozzle diffuser valves, diodes are not requested and the Tesla valves can be represented by 2 inertances in series with 2 resistances. This simple design already has been reported using an electrical equivalent in previous work [49]. For calculation of the hydraulic resistance in the inlet and outlet, the first-order

approximation of hydraulic resistance for a rectangle cross-section has been used, similarly to the nozzle-diffuser (Eq. 3.7) [52]. The channels are filled with liquid (water) that can present some inertia, therefore an inertance is needed in series with the resistance to fully model the channel. In addition, the inlets and outlet are not closed by a lid, therefore the pressure at this part of the circuit is the atmospheric pressure and should be represented with a ground (Figure 3.27). The inertance and capacitance of the water in the pumping chamber, as well as the inertance and capacitance of the membrane, have been calculated similarly to the lumped model of the nozzle diffuser, using the same equations but with the dimensions of the Tesla valve-based micropump. A Tesla valve can be modeled using low-order modeling [53]. Therefore in this case the CFD simulation is not needed to extract the parameters needed for the lumped model, unlike for the nozzle-diffuser valve. As reported by Morris and Forster, the Tesla valve can be considered as an equivalent resistance R_v in series with an equivalent inertance I_s, the equivalent resistance is calculated using the estimated length of the Tesla valve (Leq):

Table 3.6: Used dimensional parameters for the lumped model of the Tesla valve.

Parameter	Description
μ	water absolute viscosity
Leq	length of the tesla channel
2b	channel depth
α	channel aspect ratio (width over depth)
ρ	density of water

$$R_v = \frac{3\mu Leq}{4\alpha^3 b^4}\left[1 - 6\sum_{n=0}^{\infty}\frac{\alpha\tanh(\frac{p_n}{\alpha})}{p_n^5}\right]^{-1} \tag{3.18}$$

where $p_n = (2n + 1\pi/2)$ is a geometrical parameters [42], for sake of calculation n=100. The resistance has been calculated using MATLAB 2019. The inertance I_s of the tesla valve was estimated using the following equation:

$$I_s = \frac{\rho Leq}{4\alpha b^2} \tag{3.19}$$

The chamber is filled with liquid and resistive behavior on the walls of the chamber is neglected in comparison to capacitive behavior as the chamber is more than 5 times wider than taller, therefore the liquid in the chamber can be modeled with a capacitance connected to the ground. The liquid in the chamber also has some inertia and therefore inertance is required (Figure 3.27). Similarly to the lumped model of the nozzle diffuser, we consider a PDMS membrane actuated by an IPMC embedded in the bulk PDMS. The moving membrane gives a capacitive effect to the entire system. The membrane also has inertia and therefore needs an inertance to be modeled. The actuating IPMC can be modeled as a voltage supply inducing

pressure imbalance on the membrane. The lumped model has been run under Lt Spice (version 17) and the output of the simulation was exported to Python 3.6 using Lt Spice packages for further comparison with the PIV experimental results (Section 3.5). The values calculated and used for the model have been gathered in Table 3.7.

Table 3.7: Calculated parameters used for the lumped model including the Tesla valves.

Symbol	Value	Definition
L_1	$9.85\ N.s^2.m^{-5}$	Membrane Inductance
C_1	$4.75 \times 10^{-9}\ m^5.N^{-1}$	Membrane Capacitance
L_2	$7.934 \times 10^3\ N.s^2.m^{-5}$	Chamber Inductance
C_2	$9.14 \times 10^{-18}\ m^5.N^{-1}$	Chamber Capacitance
$L_3\ L_4\ L_8\ L$	$3.378\,46 \times 10^5\ N.s^2.m^{-5}$	Tesla Inductance
$R_2\ R_3\ R_4\ R_5$	$1.769\,268 \times 10^6\ N.s.m^{-5}$	Tesla Resistance
$R_1\ R_6$	$1.604\,343\,0 \times 10^7\ N.s.m^{-5}$	Inlet and outlet Resistance
$L_5\ L_6$	$3.190\,400 \times 10^6\ N.s^2.m^{-5}$	Inlet and outlet Inductance

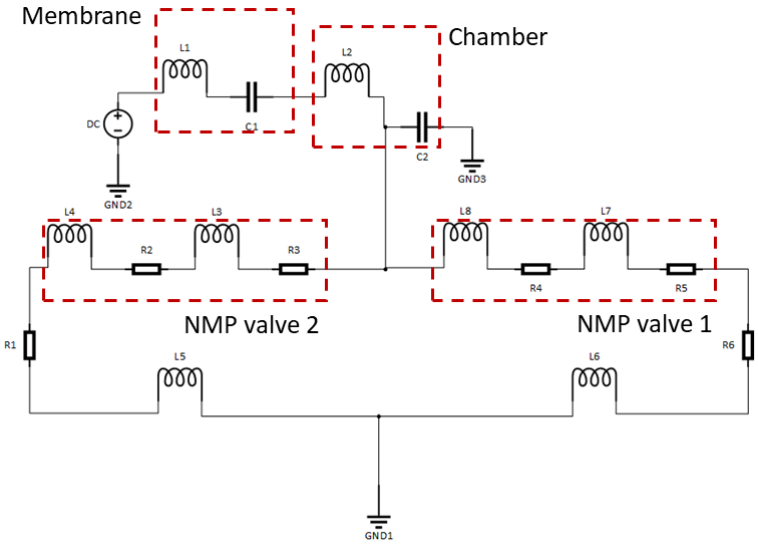

Figure 3.27: Lumped model of the microfluidic pump including Tesla valves. The membrane is represented by an inertance in series with a capacitance. The liquid in the pumping chamber is represented through capacitance and an inertance. The two NMP valves are represented by inertances in series with resistances.

For the simulation an input voltage of 0.5 V at 1Hz, corresponding to a pressure of 500mPa was applied in the chamber.

3.5. Device characterization

The micropump including the Tesla valve and manufactured by using direct light printing has been characterized through particle images velocimetry, voltage sweep, and frequency sweep have been performed to estimate the influence of the two parameters. The results of the lumped model also have been compared to the experimental data.

3.5.1. Microfluidic platform

To test the micropump a platform has been developed made of two separated parts. The platform includes an electronic board to drive the IPMC as well as the OoC inserted in a holder for ease of handling (Figure 3.28).

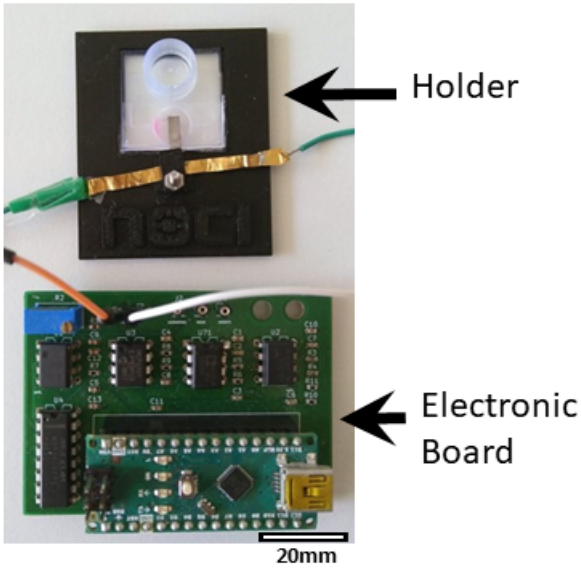

Figure 3.28: Microfluidic platform, including electronic board and holder for the micropump. The board is the same as in Chapter 2, schematic is available in Appendix 7.5.

A culture chamber has been created on the side of the micropump (Figure 3.23). The culture chamber has been filled with photosensitive hydrogel, a visco-elastic material that mimic closely the cellular microenvironment, a digital micromirror device (DMD, Primo Alvéole) has been used for the patterning (Figure 3.29). DMD is based on a UV source controlled through a set of mirrors in order to pattern precisely the hydrogel [54, 55]. The hydrogel has been patterned in a shape of a channel to reproduce a lumen, mimicking a microcapillary. More precisely, the channel has been filled with photosensitive 4-arm PEG hydrogel. A 220 μm wide and 250 μm tall hydrogel channel has been patterned using the DMD-based setup with 375 nm UV light for exposure from the bottom, through the glass coverslip (Figure 3.29).

For the electronics, a digital-to-analog converter (DAC) was used in series to the digital output of an Arduino microcontroller to actuate the IPMC substrate similarly to the electronics explained in Chapter 2 (Figure 2.6, Figure 2.7). The amplifier and DAC were both powered by the microcontroller. A 2.5 V reference was used to deliver a full square wave with a 5 Vpp amplitude. A Matlab-based graphical user interface was used to control the frequency and voltage. The precise schematic of the electronic circuit can be found in Appendix 7.5.

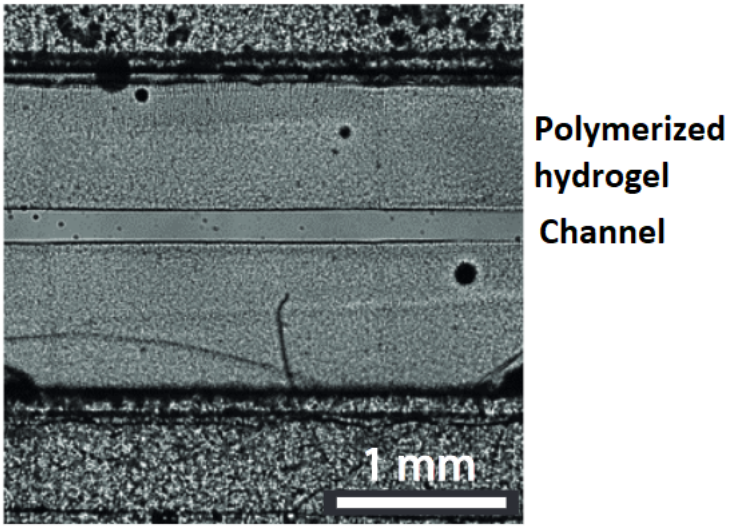

Figure 3.29: Microscope bright field view of the patterned hydrogel channel. The microfluidic channel can be seen in the central part, where the hydrogel has been removed.

3.5.2. Particle image velocimetry

Particle image velocimetry (PIV) is a method used to extract the vector field of a fluid flow. By seeding particles in the microfluidic channel, it is possible to record videos through an optical camera (flow visualization), by further processing of the videos it is possible to finally extract the vector fields [56]. The optical setup was a Nikon Eclipse (Ts2R-Fl) inverted microscope with a DS-Qi2 camera. Strictly speaking, the setup is not using a laser as a proper PIV setup would provide, in our situation, we could have an inverted microscope holding a camera with sufficient speed (45fps maximum) with fluorescence capabilities. The magnification used is 10x to be able to have an image large enough of the microfluidic circuit. The setup hosts a 477nm and 525 nm fluorescence capability. The fluorescence beads used were 1μm wide (FluoSpheres Polystyrene Microspheres) reference: F13083 and have been seeded in the channel at an approximate density of 1000 beads per μl. The focus of the microscope was directed in the central part of the channel, where the maximum amount of beads was moving. Further processing was performed to extract the velocity field using OpenCV and OpenPIV under Python 3.6.

To process the videos, preprocessing was needed using OpenCV and Python 3.6. The procedure was as follows:

- frames of the video were extracted
- pictures were binarized using a fixed threshold
- background subtraction was performed from one frame to another in order to remove fixed particles
- using OpenPIV, the vector field was extracted based on a correlation algorithm
- outliers from the vector field were removed (using the fact that the channel is aligned with the main axis of the camera recording)
- Using the velocity field, the flow rate was calculated as the dimensions of the channel are known
- flowrate values were filtered using Savitzky-Golay algorithm under Python 3.6

The use of Savitzky-Golay filter was needed to remove the impact of some vector outliers that could hamper the output signal. The microscope stage has been positioned in the culture chamber part, where the hydrogel is situated, in order to record the velocity field in the relevant part of the circuit, where tissue would grow.

As an example for clarity, a series of 2 frames (numbered 71 and 72) extracted from the video recording at 1Hz 3Vpp actuation pattern can be seen below Fig **??**. As well as the binarized pictures and the resulting computed vector fields

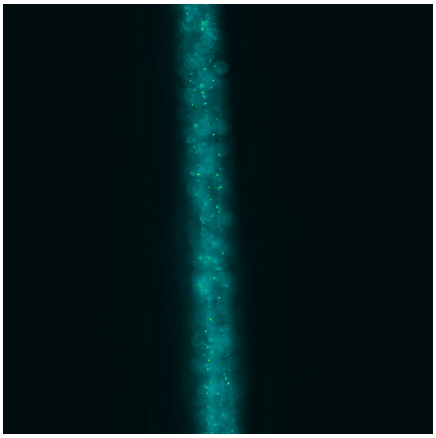

(a) Frame 71 of the video using 1Hz 3Vpp actuation pattern.

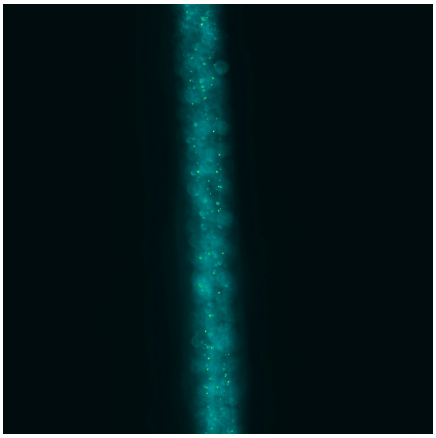

(b) Frame 72 of the video using 1Hz 3Vpp actuation pattern.

Figure 3.30: An example of the PIV preprocess-part 1, 2 frames are extracted from the video.

(a) Binarized image of the frame 71 (resulting of the background subtraction and thresholding, moving particles can be seen).

(b) Binarized image of the frame 72 (resulting of the background subtraction and thresholding, moving particles can be seen).

Figure 3.31: An example of the PIV pre-process-part 2, video frames are binarized to be further processed through the PIV algorithm.

3.5.3. Shear Stress

The shear stress τ can be estimated in a rectangular channel through the following equation:

$$\tau = \frac{6\eta Q}{H^2 W} \tag{3.20}$$

where Q is the flow rate, H is the height of the channel, w is the width, and η is the dynamic viscosity of the medium.

Interestingly we found a qualitative good fit between the experimental data and the simulation for the flow rate (Figure 3.33). The assumption of a 500 mPa pressure input inside the chamber due to the actuating membrane is correct as the peak flow rate achieved by the pump corresponds to the peak flow rate simulated (Figure 3.33). We can notice that the change of flow direction is sharper for the simulation than for the experimental data. The model neglected components with capacitive behavior such as the hydrogel channel, that might help smoothen the changes of the direction of the flow. The simulation is not meant to perfectly fit the experimental data but is meant to be used in order to study the frequency response of the system, as shown in Figure 3.34. However, the simulation can also be efficiently used to verify the impact of design updates (such as the dimension of the pumping chamber, channel dimensions) on the flow rate and frequency response of the system. We found a maximum peak flow rate for a 3Vpp at 1Hz actuation giving 1μl/min (Figure 7.4). This flow rate gives a maximum wall shear stress of 0.008 Pa in the hydrogel channel. This shear stress value is relatively small for vasculature application but high enough to trigger mechanotransduction mechanisms in bone cells for example [3]. The flow rate could be increased by changing the design of

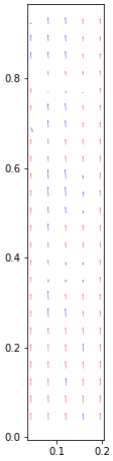

(a) Vectors field computed for frame 71, scale is in mm.

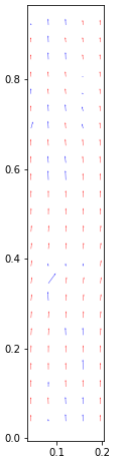

(b) Vectors field computed for frame 72, scale is in mm.

Figure 3.32: An example of the PIV, vectors field is stored in a text file in m/s and plotted with a constant arbitrary scale factor.

the micropump, for instance, a bigger pumping chamber as well as a bigger IPMC cantilever could give a bigger pressure drop. Also, by decreasing the size of the channel it could be possible to increase the wall shear stress within the lumen. For this proof-of-concept device, we used a simple glass coverslip, later a bigger glass substrate (for instance using well-plate dimensions) could give more freedom of design for a wider range of flow rate and shear stress. The achieved flow rate is lower than what has been previously published using a nozzle diffuser NMP valve based on a piezoelectric actuator [36]. In addition, our micropump shows a lower maximum flow rate than flap valve IPMC-based micropump [30, 31]. Santos *et al.* could achieve 5μl/s using nozzle diffuser in a milimeter-sized fluidic circuitry while Nguyen *et al.* could reach an remarkable flowrate of 750 μl/min using flap valve design. However, the first micropump is 8 cm wide with 10mm-wide channels, far from the dimensions used in OoC, while the second micropump uses a flap valve, known for its mechanical fragility as well as being not optimal while using circulating cells because of the risk of clogging.

3.5.4. Voltage and frequency sweep

A sweep over the actuation period ranging from 200ms to 1600ms in order to study the frequency response of the micropump was performed with a fixed voltage of 4Vpp. Another sweep to study the influence of the voltage for actuation was performed using a fixed period of 1000ms with a peak-to-peak voltage ranging from 1V to 4V. For every experiment, a 1min PIV video has been extracted to further process the velocity field and flow rate. For each parameter, 3 videos of 1 min have been used, and average and standard deviation have been calculated.

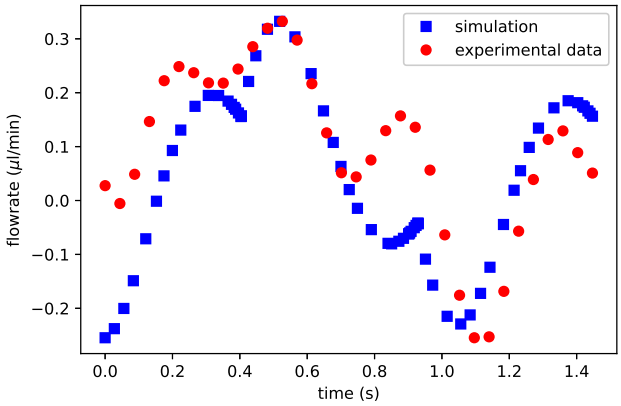

Figure 3.33: Flowrate calculated in the hydrogel channel for 1Hz actuation at 500mPa for the simulation (blue) and corresponding flowrate measured from the experimental data at 1Hz for 2Vpp (red). The mismatch is probably due to the capacitive components neglected in the lumped model (hydrogel channel).

The experimental frequency sweep (Figure 3.34) showed a resonance frequency of the micropump system for a 1200ms period (0.83 Hz). The simulation also shows a resonance frequency, but for a slightly higher frequency (1000ms period). Interestingly the general pattern for the simulation and experimental data is similar, showing a negative net flowrate rate for high frequency (200ms period), increasing to reach the resonance frequency and finally slightly decreasing. As said for the flowrate, the lumped model is simple and the capacitive effect of the hydrogel channel made of soft material was neglected for the first lumped model. Developing a more realistic model for hydrogel-based channels is reserved for future work. Also in reality the IPMC actuator is not perfect, delivering filtered force output while actuated with a square wave signal. Those differences between simulation and reality may explain the 20% difference in the resonance frequency.

Interestingly the voltage study shows an optimum voltage for pumping at 3Vpp, while higher voltage shows a decrease in the flowrate (Figure 3.35). We hypothesize that the optimum voltage for actuation is actually 3Vpp (or 1.5 V with cathode and anode shifting periodically) as higher voltage might lead to electrolysis of water, hampering actuation capabilities [57]. For the electrochemical water splitting reaction, the thermodynamic potential is 1.23V at 25 °C and 1 atm. However, due to the kinetic barrier for the reaction, water electrolysis requires a higher potential than thermodynamic potential (1.23 V) to overcome the kinetic barrier. In our case, we noticed that the electrolysis reaction started at 1.5 V, most probably also because of the morphology of the electrode (Chapter 4) and the design of the electronics (Chapter 2). In our case, 1.5V experimentally corresponds to 3V peak-to-peak as our actuation pattern is oscillating around 0V to shift the cathode and the anode periodically and triggers displacement (Chapter 2).

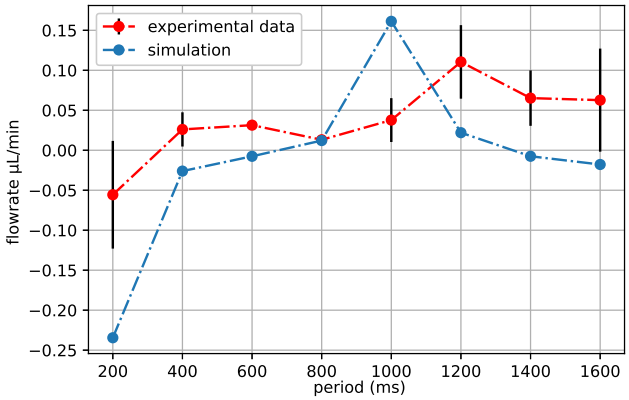

Figure 3.34: Actuation period sweep for the mean of the net flowrate for the experimental data and simulation. The voltage has been set to 4Vpp. For the experimental data, 3 videos have been used for each period, and mean and standard deviation have been calculated.

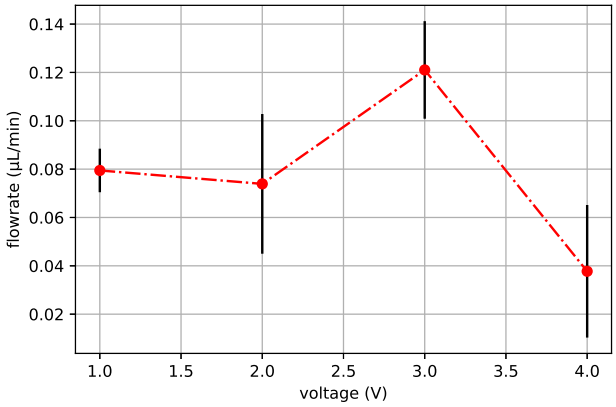

Figure 3.35: Actuation voltage sweep for the experimental value of flow rate at a fixed frequency of 1Hz. Maximum flowrate was achieved at 3Vpp, where the maximum displacement was achieved by the IPMC, before the potential occurring of electrolysis (4Vpp). The statistics (error bars) are the following: 0.009,0.029,0.020,0.027.

3.5.5. Reliability of the IPMC-based micropump

The IPMC-based micropump has been found to show some reliability issues which need to be reported. The injection of hydrogel within the chamber and the patterning has been found to work better without oxygen plasma treatment beforehand. The hydrogel droplet was found to spread over the chip surface instead of going inside the chamber if surface treatment was performed. Repetitive pipetting within

the chamber improves the injection of the hydrogel. The injection of hydrogel needs to be performed with care to avoid the apparition of bubbles. In addition, the bottom of the chip is made of a microscope coverslip and was found to be fragile, leading to potential breaking and ultimately leakage. Also, the bonding between glass and the DLP print was found to lead to potential leakage (as pressure would break the glass), this problem could be solved easily by using thicker glass or different material and manufacturing techniques such as cyclic olefin copolymer (COC), a transparent thermoplastic. Finally, the handling of the IPMC-PDMS membrane was found to be delicate and requires precise alignment to ensure that the tip of the IPMC cantilever is positioned in the center of the pumping chamber.

3.6. Conclusion

We have successfully manufactured a micropump for potential organ-on-chip applications with an integrated hydrogel channel for relevant microenvironment mimicry. By using ionic electroactive material and high-resolution 3D printing techniques we could obtain an easy-to-use, versatile, and integrated micropump. We have characterized the micropump and showed that the achieved flowrate and shear stress are biologically relevant for models requiring small shear stress such as bone tissue [3]. Interestingly there are also organs releasing endocrine molecules where small pulsatile flow is needed such as testicles [58], where needed wall shear stress has been reported to be in the 0.001 Pa range.

The cumbersomeness of the pneumatic system is mostly experienced by users as pneumatic systems for microfluidics applications require numerous tubings, when using fluidic cartridges many pressure inlets are needed to actuate each valve or peristaltic pump, hampering the scalability of the system. If the fluidics is not integrated in a microfluidic cartridge then fluidic tubes are required, connected to pressurized containers (Falcon). In this situation the long tubes filled with water are very sensitive to external input such as handling and the final microfluidic circuit might be impacted by the handling of the tubing (bubbles, drop of pressure). Our proposed solution by integrating the electronically actuated polymer-based diaphragm within the microfluidic circuit (Figure 3.23) avoids the use of tubings for pressurized air or liquid, easing handling and scalability in the future.

We also have successfully developed a lumped model of the micropump for simulation that could be used in the future to further develop the device and predict the design modification beforehand. The simulation shows a qualitative fit with the experimental data, especially for the frequency response of the system. However, we also noticed differences, especially in the flowrate response locally, showing that the lumped model could be improved by further characterization of the force output of the IPMC membrane as well as by integrating more capacitive components in the lumped model (for instance due to the presence of hydrogel, a visco elastic material). This lumped model is the first for a flexible iEAP-PDMS membrane integrated with a NMP valve design based on Tesla valve. This work could represent a milestone for further development of ionic electroactive polymer micropump for organ-on-chip, point-of-care devices or lab-on-chip devices application. Predicting the flow rate and the frequency response of the system with the lumped model

could be also performed in order to precisely evaluate the influence of the design parameters. The good properties of IPMC such as bio-compatibility, low voltage input, flexibility, and high force output makes IPMC a good candidate for other biological MEMS-based application. Further investigations could be performed by implementing different pump designs (pumping chamber and channel dimensions) depending on the targetted application or organ model. One could imagine integrating several pumps, or a bigger pumping chamber with higher flow regimes on the same plate in order to achieve a biologically relevant flow rate suitable for instance for models of vasculature [3].

In the current and previous chapter standard IPMC has been used with a thickness of 180 μm. However as shown in Chapter 2 one of the limitations of standard IPMC is its inherent high flexural rigidity due to its thickness, leading to a stiff substrate where contractile tissue can hardly induce a displacement and be sensed by the IPMC. In the next chapter, the manufacturing of thin IPMC (50 μm) will be explained, and the dynamics of the chemical reaction involved during the manufacturing compared in between thick Nafion and thin Nafion. Finally, the material will be characterized (sensitivity, flexural rigidity, and Young's modulus).

References

[1] B. Zhang, A. Korolj, B. F. L. Lai, and M. Radisic, *Advances in organ-on-a-chip engineering,* Nature Reviews Materials **3**, 257 (2018).

[2] M. L. Coluccio, G. Perozziello, N. Malara, E. Parrotta, P. Zhang, F. Gentile, T. Limongi, P. M. Raj, G. Cuda, P. Candeloro, and E. Di Fabrizio, *Microfluidic platforms for cell cultures and investigations,* Microelectronic Engineering **208**, 14 (2019).

[3] W. J. Polacheck, R. Li, S. G. M. Uzel, and R. D. Kamm, *Microfluidic platforms for mechanobiology,* Lab on a Chip **13**, 2252 (2013).

[4] K. Kaarj and J.-Y. Yoon, *Methods of Delivering Mechanical Stimuli to Organ-on-a-Chip,* Micromachines **10**, 700 (2019).

[5] E. Ergir, B. Bachmann, H. Redl, G. Forte, and P. Ertl, *Small Force, Big Impact: Next Generation Organ-on-a-Chip Systems Incorporating Biomechanical Cues,* Frontiers in Physiology **9**, 1 (2018).

[6] P. J. Lee, P. J. Hung, and L. P. Lee, *An artificial liver sinusoid with a microfluidic endothelial-like barrier for primary hepatocyte culture,* Biotechnology and Bioengineering **97**, 1340 (2007), _eprint: https://onlinelibrary.wiley.com/doi/pdf/10.1002/bit.21360.

[7] D. Bavli, S. Prill, E. Ezra, G. Levy, M. Cohen, M. Vinken, J. Vanfleteren, M. Jaeger, and Y. Nahmias, *Real-time monitoring of metabolic function in*

liver-on-chip microdevices tracks the dynamics of mitochondrial dysfunction, Proceedings of the National Academy of Sciences **113**, E2231 (2016), publisher: Proceedings of the National Academy of Sciences.

[8] K.-J. Jang, A. P. Mehr, G. A. Hamilton, L. A. McPartlin, S. Chung, K.-Y. Suh, and D. E. Ingber, *Human kidney proximal tubule-on-a-chip for drug transport and nephrotoxicity assessment,* Integrative Biology **5**, 1119 (2013).

[9] K. Schimek, M. Busek, S. Brincker, B. Groth, S. Hoffmann, R. Lauster, G. Lindner, A. Lorenz, U. Menzel, F. Sonntag, H. Walles, U. Marx, and R. Horland, *Integrating biological vasculature into a multi-organ-chip microsystem,* Lab on a Chip **13**, 3588 (2013).

[10] X. F. Liu, J. Q. Yu, R. Dalan, A. Q. Liu, and K. Q. Luo, *Biological factors in plasma from diabetes mellitus patients enhance hyperglycaemia and pulsatile shear stress-induced endothelial cell apoptosis,* Integrative Biology **6**, 511 (2014).

[11] J. Shao, L. Wu, J. Wu, Y. Zheng, H. Zhao, Q. Jin, and J. Zhao, *Integrated microfluidic chip for endothelial cells culture and analysis exposed to a pulsatile and oscillatory shear stress,* Lab on a Chip **9**, 3118 (2009).

[12] U. Haessler, J. C. M. Teo, D. Foretay, P. Renaud, and M. A. Swartz, *Migration dynamics of breast cancer cells in a tunable 3D interstitial flow chamber,* Integrative Biology: Quantitative Biosciences from Nano to Macro **4**, 401 (2012).

[13] K. M. Kingsmore, D. K. Logsdon, D. H. Floyd, S. M. Peirce, B. W. Purow, and J. M. Munson, *Interstitial flow differentially increases patient-derived glioblastoma stem cell invasion via CXCR4, CXCL12, and CD44-mediated mechanisms,* Integrative Biology: Quantitative Biosciences from Nano to Macro **8**, 1246 (2016).

[14] S. Kim, M. Chung, J. Ahn, S. Lee, and N. L. Jeon, *Interstitial flow regulates the angiogenic response and phenotype of endothelial cells in a 3D culture model,* Lab on a Chip **16**, 4189 (2016), publisher: The Royal Society of Chemistry.

[15] A. M. Pollet and J. M. den Toonder, *Recapitulating the Vasculature Using Organ-On-Chip Technology,* Bioengineering **7**, 17 (2020).

[16] K. Sato and K. Sato, *Chapter 6 - Blood vessels-on-a-chip,* in *Principles of Human Organs-on-Chips*, Woodhead Publishing Series in Biomaterials, edited by M. Mozafari (Woodhead Publishing, 2023) pp. 167–194.

[17] C. K. Byun, K. Abi□Samra, Y.-K. Cho, and S. Takayama, *Pumps for microfluidic cell culture,* ELECTROPHORESIS **35**, 245 (2014), _eprint: https://onlinelibrary.wiley.com/doi/pdf/10.1002/elps.201300205.

[18] M.-H. Wu, S.-B. Huang, and G.-B. Lee, *Microfluidic cell culture systems for drug research,* Lab on a Chip **10**, 939 (2010).

[19] M. Mastrangeli, S. Millet, t. O. Partners, and J. v. d. E.-v. Raaij, *Organ-on-Chip In Development:Towards a roadmap for Organs-on-Chip,* (2019), 10.20944/preprints201903.0031.v1.

[20] N.-T. Nguyen, X. Huang, and T. K. Chuan, *MEMS-Micropumps: A Review,* Journal of Fluids Engineering **124**, 384 (2002).

[21] D. J. Laser and J. G. Santiago, *A review of micropumps,* Journal of Micromechanics and Microengineering **14**, R35 (2004), publisher: IOP Publishing.

[22] M. Annabestani and M. Fardmanesh, *Ionic Electro active Polymer-Based Soft Actuators and Their Applications in Microfluidic Micropumps, Microvalves, and Micromixers: A Review,* arXiv:1904.07149 [physics, q-bio] (2019), arXiv: 1904.07149.

[23] W. Hilber, *Stimulus-active polymer actuators for next-generation microfluidic devices,* Applied Physics A **122**, 751 (2016).

[24] E. A. Sideris, H. C. de Lange, and A. Hunt, *An ionic polymer metal composite (ipmc)-driven linear peristaltic microfluidic pump,* IEEE Robotics and Automation Letters **5**, 6788 (2020).

[25] E. A. Sideris and H. C. de Lange, *Pumps operated by solid-state electromechanical smart material actuators - A review,* Sensors and Actuators A: Physical **307**, 111915 (2020).

[26] S. Lee and K. J. Kim, *Design of IPMC actuator-driven valve-less micropump and its flow rate estimation at low Reynolds numbers,* Smart Materials and Structures **15**, 1103 (2006), publisher: IOP Publishing.

[27] T. T. Nguyen, V. K. Nguyen, Y. Yoo, and N. S. Goo, *A Novel Polymeric Micropump based on a Multilayered Ionic Polymer-Metal Composite,* in *IECON 2006 - 32nd Annual Conference on IEEE Industrial Electronics* (2006) pp. 4888–4893.

[28] S. Ramírez-García and D. Diamond, *Biomimetic, low power pumps based on soft actuators,* Sensors and Actuators A: Physical Special Issue of The Micromechanics section of Sensors and Actuators (SAMM, based on contributions revised from the Technical Digest of the IEEE 19th International conference on Micro Electro Mechanical Systems (MEMS 2006), **135**, 229 (2007).

[29] D. N. C. Nam and K. K. Ahn, *Design of an IPMC diaphragm for micropump application,* Sensors and Actuators A: Physical **187**, 174 (2012).

[30] T. T. Nguyen, N. S. Goo, V. K. Nguyen, Y. Yoo, and S. Park, *Design, fabrication, and experimental characterization of a flap valve IPMC micropump with a flexibly supported diaphragm,* Sensors and Actuators A: Physical **141**, 640 (2008).

[31] J. Santos, B. Lopes, and P. J. C. Branco, *Ionic polymer–metal composite material as a diaphragm for micropump devices,* Sensors and Actuators A: Physical **161**, 225 (2010).

[32] J. Wang, A. J. McDaid, C. Z. Lu, and K. C. Aw, *A Compact Ionic Polymer-Metal Composite (IPMC) Actuated Valveless Pump for Drug Delivery,* IEEE/ASME Transactions on Mechatronics **22**, 196 (2017), conference Name: IEEE/ASME Transactions on Mechatronics.

[33] N. Bhattacharjee, A. Urrios, S. Kang, and A. Folch, *The upcoming 3D-printing revolution in microfluidics,* Lab on a Chip **16**, 1720 (2016).

[34] H. Sun, Y. Jia, H. Dong, D. Dong, and J. Zheng, *Combining additive manufacturing with microfluidics: an emerging method for developing novel organs-on-chips,* Current Opinion in Chemical Engineering Materials Engineering • Separations Engineering, **28**, 1 (2020).

[35] E. Morganti, I. Fuduli, A. Montefusco, M. Petasecca, and G. U. Pignatel *, *SPICE modelling and design optimization of micropumps,* International Journal of Environmental Analytical Chemistry **85**, 687 (2005).

[36] A. Olsson, P. Enoksson, G. Stemme, and E. Stemme, *Micromachined flat-walled valveless diffuser pumps,* Journal of Microelectromechanical Systems **6**, 161 (1997).

[37] Y. Hou, L. He, D. Hu, L. Zhang, B. Yu, and G. Cheng, *Recent trends in structures and applications of valveless piezoelectric pump—a review,* Journal of Micromechanics and Microengineering **32**, 053002 (2022), publisher: IOP Publishing.

[38] X. Wu, L. He, Y. Hou, X. Tian, and X. Zhao, *Advances in passive check valve piezoelectric pumps,* Sensors and Actuators A: Physical **323**, 112647 (2021).

[39] S. Mi, H. Pu, S. Xia, and W. Sun, *A Minimized Valveless Electromagnetic Micropump for Microfluidic Actuation on Organ Chips,* Sensors and Actuators A: Physical **301**, 111704 (2020).

[40] C. Yamahata, C. Vandevyver, F. Lacharme, P. Izewska, H. Vogel, R. Freitag, and M. A. M. Gijs, *Pumping of mammalian cells with a nozzle-diffuser micropump,* Lab on a Chip **005**, 1083 (2005), publisher: The Royal Society of Chemistry.

[41] L. Songjing, J. Liu, and D. Jiang, *Dynamic Characterization of a Valveless Micropump Considering Entrapped Gas Bubbles,* Journal of Heat Transfer **135**, 091403 (2013).

[42] F. M. White, *Fluid Mechanics* (McGraw Hill, 2011).

[43] F. Laermer, S. Franssila, L. Sainiemi, and K. Kolari, *Chapter 16 - Deep reactive ion etching,* in *Handbook of Silicon Based MEMS Materials and Technologies (Third Edition)*, Micro and Nano Technologies, edited by M. Tilli, M. Paulasto-Krockel, M. Petzold, H. Theuss, T. Motooka, and V. Lindroos (Elsevier, 2020) pp. 417–446.

[44] E. Verpoorte and N. De Rooij, *Microfluidics meets MEMS,* Proceedings of the IEEE **91**, 930 (2003), conference Name: Proceedings of the IEEE.

[45] S. Bhattacharya, B. Bepari, and S. Bhaumik, *Soft robotic finger fabrication with PDMS and IPMC actuator for gripping,* in *2016 SAI Computing Conference (SAI)* (2016) pp. 403–408.

[46] S. Tsuchitani, K. Kikuchi, I. Shimizu, T. Taniguchi, and H. Miki, *IPMC Actuators Fabricated Using MEMS Technology,* Advances in Science and Technology **97**, 57 (2016).

[47] G.-H. Feng and R.-H. Chen, *Improved cost-effective fabrication of arbitrarily shaped uipmc transducers,* Journal of Micromechanics and Microengineering **18**, 015016 (2007).

[48] Y. Bao, N. Paunović, and J.-C. Leroux, *Challenges and Opportunities in 3D Printing of Biodegradable Medical Devices by Emerging Photopolymerization Techniques,* Advanced Functional Materials **32**, 2109864 (2022), _eprint: https://onlinelibrary.wiley.com/doi/pdf/10.1002/adfm.202109864.

[49] N.-B. Le and Y.-C. Hsu, *MNHT2008-52047 DEMONSTRATION AND CHARACTERIZATION OF INERTANCE EFFECTS TO DIFFUSER MICROPUMPS FLOW RATE SPECTRUM,* in *Micro Nanoscale Heat Transfer International Conference* (2008).

[50] Y.-C. Hsu and N.-B. Le, *Inertial effects on flow rate spectrum of diffuser micropumps,* Biomedical Microdevices **10**, 681 (2008).

[51] A. Olsson, G. Stemme, and E. Stemme, *A numerical design study of the valveless diffuser pump using a lumped-mass model,* Journal of Micromechanics and Microengineering **9**, 34 (1999).

[52] R. Oosterbroek, *Modeling, design and realization of microfluidic components*, Ph.D. thesis, s.n.], S.l. (1999), iSBN: 9789036513463 OCLC: 67295242.

[53] C. Morris and F. Forster, *Low-order modeling of resonance for fixed-valve micropumps based on first principles,* Journal of Microelectromechanical Systems **12**, 325.

[54] W. Yang, Z. Wang, X. Wang, T. Yu, S. Xie, and Z. Ge, *3D printing of bioinspired hydrogel microstructures with programmable and complex shape deformations based on a digital micro-mirror device,* Optics & Laser Technology **157**, 108759 (2023).

[55] Y. Lu, G. Mapili, G. Suhali, S. Chen, and K. Roy, *A digital micro-mirror device-based system for the microfabrication of complex, spatially patterned tissue engineering scaffolds,* Journal of Biomedical Materials Research Part A **77A**, 396 (2006), _eprint: https://onlinelibrary.wiley.com/doi/pdf/10.1002/jbm.a.30601.

[56] I. Grant, *Particle image velocimetry: A review,* Proceedings of the Institution of Mechanical Engineers, Part C: Journal of Mechanical Engineering Science **211**, 55 (1997), publisher: IMECHE.

[57] S. Nemat-Nasser, *Micromechanics of actuation of ionic polymer-metal composites,* Journal of Applied Physics **92**, 2899 (2002).

[58] S. Sharma, B. Venzac, T. Burgers, S. Schlatt, and S. Le Gac, *Testis-on-chip platform to study ex vivo primate spermatogenesis and endocrine dynamics,* Organs-on-a-Chip **4**, 100023 (2022).

4

Manufacturing ionic polymer metal composite: a comparative study

Rather than love, than money, than fame, give me truth.

Henri David Thoreau

Parts of this chapter have been published in Smart Materials and Structures, 32, (2023) and presented in the 242nd Electrochemical society (ECS) meeting 9-13th October 2022 Atlanta, USA.

In this chapter, the manufacturing of thin (50 μm) IPMC is explored in the context of sensors application for organ-on-chip, and the dynamics of the electroless deposition recipe involved during the manufacturing is compared between thick (180 μm) Nafion and thin (50 μm) Nafion. Finally, the material is characterized with respect to sensitivity, flexural rigidity, and Young's modulus.

4.1. Introduction

Ionic polymer metal composite (IPMC) is used in the soft robotic field for its properties (see Chatper 2). However organ-on-chip in particular and MEMS, in general, require to actuate, sense, and monitor in the microscale range, too small for the already existing IPMC material developed for centimeter-scale application. IPMC has already been introduced in Chapter 2 and used for pumping applications in Chapter 3. In this chapter, we will describe in more detail how IPMC is fabricated. In the first part, the core material of IPMC, Nafion is introduced as well as the fabrication process (electroless deposition). In the second part of the chapter, the results from the comparative study between thick and thin IPMC are presented. A deep understanding of the chemistry involved is required in order to develop thinner IPMC that could lead the way for actuating and sensing in the microscale for organ-on-chip devices. Finally an electroless deposition recipe, based on a dilution factor, is replicated in order to manufacture thin IPMC with lower flexural rigidity. The manufactured IPMC is fully characterized with the peripheral sensing electronics (sheet resistance, electrodes surface morphology, platinum distribution, flexural rigidity, Young's modulus and sensitivity). The developed material shows superior sensing capabilities with lower flexural rigidity (46 times) than standard IPMC.

4.1.1. Manufacturing IPMC

Perfluorinated sulfonic-acid (PFSA) ionomer: Nafion

Perfluorinated sulfonic-acid (PFSA) ionomers are members of a class of ion-conductive polymers known for their ion conductivity and stability. PFSAs are commonly used as solid-electrolyte in electrochemical technologies or polymer-electrolyte fuel cells (PEFCs). The first commercially available PFSA was developed by Dupont in the 1970's under the brand name Nafion®. Several types of PFSA exist, the differences lie on the structure and number of side chains, which lead to difference in chemical structure and behaviour (Figure 4.1).

As Nafion is the PFSA showing the best actuation capabilities with sodium ions, most commonly used in culture media, the focus in this chapter will be on Nafion [2]. Over the past decades more and more interest has been raised from scientific community regarding the potential applications for thin PFSA (Figure 4.2). However one can already notice from Figure 4.2 that interest was rising until the 2010's, with a focus on thick PFSA membrane, this rise of interest was mostly due to the hopes regarding potential applications in soft robotics and PEFC. Unfortunately, interest in such applications started to decrease after the 2010's. But the average thickness studied decreased, showing that new applications were investi-

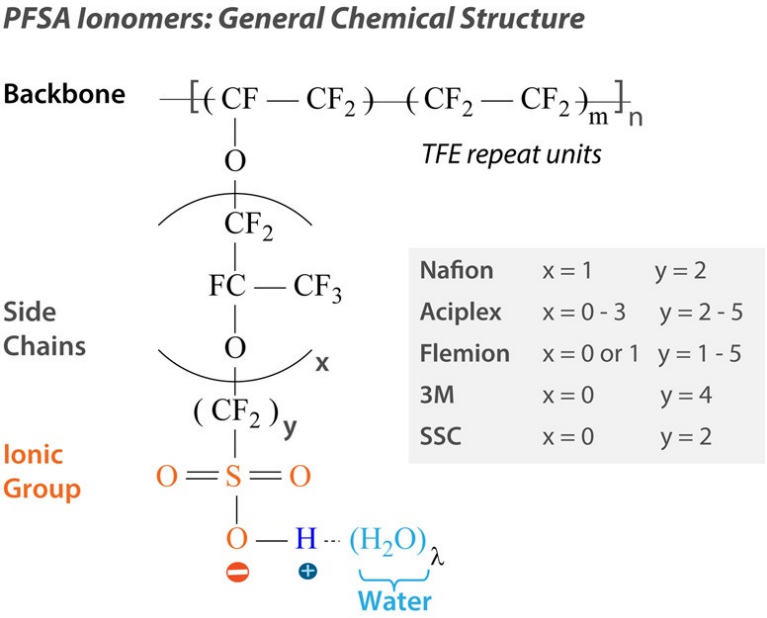

Figure 4.1: General structure of PFSA ionomers. The backbone is composed of tetrafluoroethylene (TFE) units. The fluorocarbon side chains are repeated a certain number of times, the number of repetitions will determine the length of the sides chains and therefore the chemical properties of the PFSA. All PFSA are terminated by sulfonate ionic group. Extracted from [1].

gated as well as a better understanding of thin PFSA behavior. Nafion is a random copolymer composed of an electrically-neutral semi-crystalline polymer backbone (polytetrafluoroethylene (PTFE)) and a randomly-tethered side-chain with a pendant ionic group, SO_3^- (polysulfonyl fluoride vinyl ether), that is associated with a specific counter-ion ($SO_3^- + H^+ \longrightarrow SO_3H$).

Nafion is made of a hydrophobic fluocarbon chain together with an hydrophilic anionic part (sulfonate group). The nature of Nafion results in phase separation between the anionic group and the rest of the backbone, which is enhanced by solvation (upon introduction of water or solvent molecules), giving the ionic cluster network structure (Figure 4.3) [1]. In this model the sulfonate group rearranges to allow water molecules as well as cations to freely move inside the material (Figure 4.3). This particular behavior of Nafion makes it unique for transducers properties, however it also hampers its use in semiconductor manufacturing facilities because of the solvent retention capabilities (Chapter 3).

Electroless deposition of platinum

As explained by Kim and Shahinpoor the manufacturing of IPMC requires to chemically deposit noble material such as platinum, gold or paladium on the PFSA in order to build chemically stable and mechanically resilient electrodes [3]. This manufacturing process is called electroless deposition, the most commonly used and studied

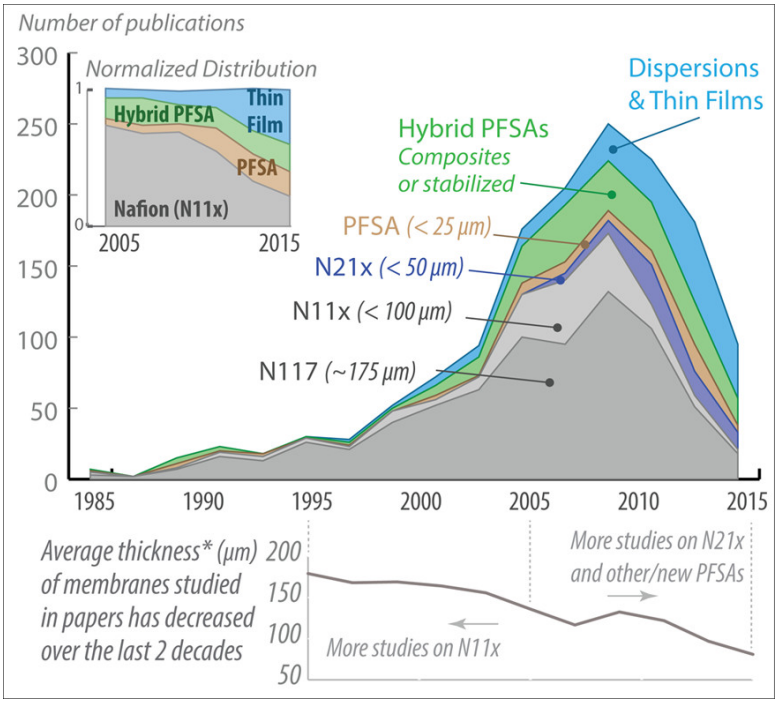

Figure 4.2: Rising interest in thinner PFSA ionomers membranes in the last decades. Interest in stabilized PFSA such as Nafion (N 117, 11x et 21x) also increased over the years. The decrease shown in 2010's is most probably due to defeated high hopes on PEFC and soft robotics applications. Extracted from [1].

material is platinum as it provides very stable IPMC electrodes [3]. Electroless deposition consists of chemically depositing platinum on the surface of a PFSA membrane and has been developed by the work of Millet *et al.* and Asaka *et al.* while developing IPMC [4] [5]. Manufacturing of standard IPMC has been reported in previous work and actually consist of 2 phases. The first phase is meant to deposit platinum deep inside Nafion using immersion in platinum salt followed by reduction [3]. Immersion-reduction steps are repeated several times and called *initial composition process*. Afterward, a final plating step is made, called *surface electrodes process*. The principle of the initial composition process is to metalize the bulk of the material by a chemical reduction of platinum inside the PFSA using reducing agent. The initial composition process requires an appropriate platinum salt such as $Pt(NH_3)_4HCl$ for doping the bulk material with platinum complex prior the reduction. Accordingly, the ion exchange polymer is soaked in a salt solution to allow platinum-containing cations to diffuse into the PFSA via the ion exchange process. Later, a proper reducing agent such as $LiBH_4$ or $NaBH_4$ is introduced to platinize the material by molecular plating. In our case the organo metallic was tetra-amine platinum chloride hydrate as an aqueous platinum complex ($[Pt(NH_3)_4]Cl_2$ or $[Pt(NH_3)_6]Cl_4$) solution. Although the equilibrium condition depends on the type of charge of the

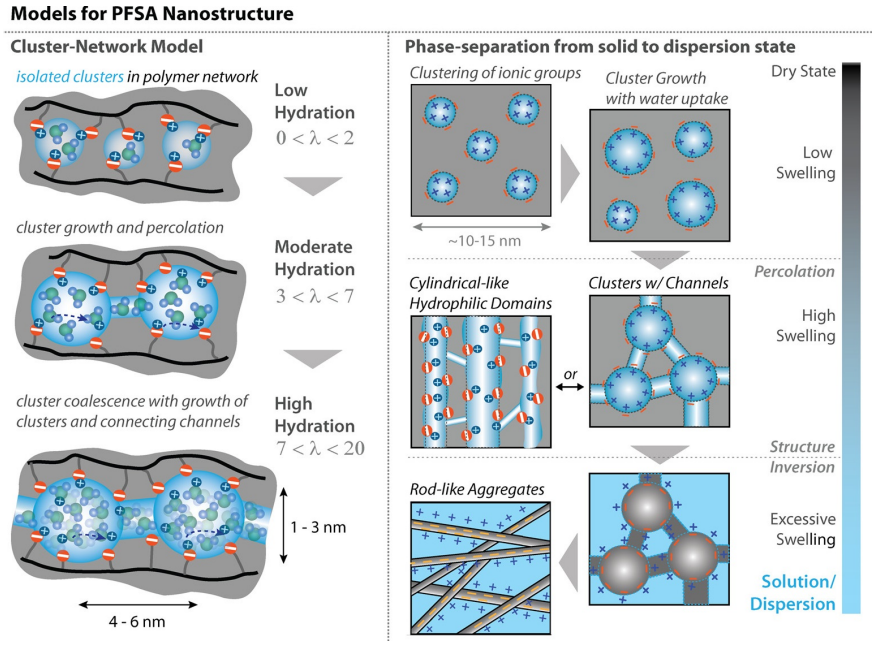

Figure 4.3: Ionic cluster model. Upon different hydration state the Nafion backbone will re-arrange. At low hydration state the sulfonates groups are organized in cluster, upon higher hydration the clusters are connected. Extracted from [1].

metal complex, such complexes were found to provide good electrodes in literature [3]. The immersion steps intended to deposit the platinum organometallic on the sulfonic acid group site within the Nafion backbone reaction 1.

$$\mathrm{R{-}(SO_3H)_2 + Pt(NH_3)_4^{2+} \longrightarrow R{-}(SO_3)_2Pt(NH_3)_4 + 2\,H^+} \qquad \{1\}$$

The reduction for the platinum is the following:

$$\mathrm{[Pt(NH_3)_4]^{2+} + 2\,e^- \longrightarrow Pt^0 + 4\,NH_3} \qquad \{2\}$$

While the oxidation reaction is the following:

$$\mathrm{NaBH_4 + 8\,OH^- \longrightarrow BO_2^- + Na^+ + 6\,H_2O + 8\,e^-} \qquad \{3\}$$

In addition, the sodium borohydride can interact with water

$$\mathrm{NaBH_4 + 2\,H_2O \longrightarrow NaBO_2 + 4\,H_2} \qquad \{4\}$$

The total oxydo-reduction reaction during the initial composition process is the following :

$$\mathrm{NaBH_4 + [Pt(NH_3)_4]^{2+} + 8\,OH^- \longrightarrow} \qquad \{5\}$$

$$4\,Pt^{0}(s) + 16\,NH_3(g) + BO_2{}^{-} + Na^{+} + 6\,H_2O \quad \{6\}$$

It can be seen (presence of protons) that pH is very important (reaction 1). Therefore during the chemical immersion (*initial composition process*), ammonium hydroxide is also added in order to promote the creation of anionic sites $SO_3{}^{-}$ and dope the maximum of sites with platinum complexes [6]. We also use Polyvinylpyrrolidone (PVP10) to improve miscibility between organic and non-organic components. The second step (*surface electrodes process*) aimed at depositing platinum on the already grown platinum sites, thus improving the overall conductivity of the electrodes. It consists of reducing platinum in the vicinity of the surface, next to the previously grown Pt sites using hydrazine monohydrate (N_2H_2) and hydroxylamine hydrochloryde ($HONH_2$ HCl). This way, the resistivity of the surface electrodes is diminished, giving a finally working IPMC. The deposition of Pt onto the surface of Nafion is based on the autocatalytic Pt reduction of $PtCl_6{}^{2-}$ with N_2H_4 (hydrazine) reactions 7,8, producing a dense micrometer-thick Pt layer on the Nafion surface in addition to low density, highly dispersed Pt particles in the bulk of the Nafion membrane. The overall electrodes show good electronic capabilites as well as superior mechanical stability, allowing the IPMC to reach high strain values at low voltage [7].

$$PtCl_6{}^{2-} + 4\,e^{-} \longrightarrow Pt + 6\,Cl^{-} \quad \{7\}$$

$$N_2H_4 \longrightarrow N_2 + H_4 + 4\,e^{-} \quad \{8\}$$

Hydrazine monohydrate is a mild reducing agent (unlike $NABH_4$), therefore controlling the pH and controlling the side reactions are very important. In addition hydrazine can also react with H^{+} and anionic group of the PFSA (Figure 4.4). Simultaneously, the N_2H^{5+} moves through the membrane and reacts with $SO_3{}^{-}$ group in the membrane as shown in Figure 4.4. After all, $SO_3{}^{-}$ groups are occupied by N_2H^{5+}, the remaining N_2H_4 and N_2H^{5+} could be oxidized and reversed, respectively: reaction 9. Excess N_2H_4 is used, as all quantity of Pt^{2+} need to be reduced by N_2H_4 into metallic platinum. Consequently, hydroxylamine hydrochloride is used as an oxidiser to reduce the hydrazine once the reaction is over with the platinum and to avoid creation of sides products. Once again PVP10 is used in order to improve miscibility between organic and non organic compounds.

$$N_2H_4 + H^{+} \longleftrightarrow N_2H_5{}^{+} \quad \{9\}$$

4.2. Thin IPMC vs thick IPMC

State-of-the-art manufacturing of standard IPMC

The electroless deposition conducted in this Chapter was performed within the Else Kooi Laboratory of TU Delft, using a microscale and stirring platform with heating capabilities. Nafion can be bought in different thicknesses, in this chapter we will call the 180 μm thick Nafion "thick" and the 50 μm thick Nafion "thin".

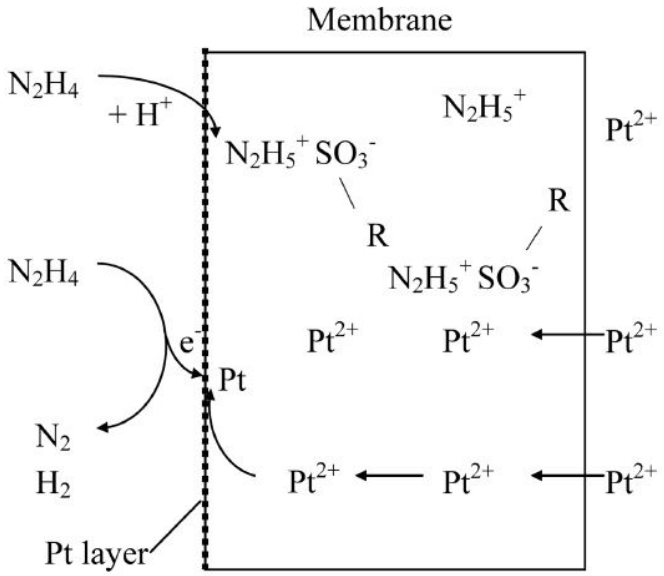

Figure 4.4: Proposed mechanism of electroless deposition for final plating of Platinum with hydrazine monohydrate. Extracted from [8].

Manufacturing IPMC for MEMS has been studied by very few reports this far. Most of the already existing reports focus on 180 μm-thick IPMC, in addition, sensing has been poorly studied. Yanamori *et al.* studied the fabrication of 180 μm-thick palladium-based IPMC for microsystems, as palladium is reported to have lower stiffness and be cheaper than Au or Pt electrodes [9]. Tsuchitani *et al.* and Feng and Chen studied the manufacturing of IPMC by using standard MEMS-specific microfabrication techniques with a focus on implementing the fabrication of IPMC on a Si substrate [10, 11]. They were able to manufacture a micro-IPMC by casting Nafion solution. However, the focus was on the standard 180 μm-thick Nafion for Yanamori *et al.*, and the standard electroless recipe for Tsuchitani *et al.* and Feng and Chen leading to too stiff material to obtain low flexural rigidity for sensing applications. Yang *et al.* reviewed recent progress in IPMC manufacturing, however, there was no report on thin Nafion for micro-scale applications [2]. Wang *et al.* studied the effect of IPMC dimensions on IPMC sensing, indicating that thicker IPMCs exhibit stronger sensing signal [12] however it is unfavorable for bio-MEMS applications due to their high thickness leading to high flexural rigidity. Thus, to give an example, Lind *et al.* developed a thin (5 μm) PDMS cantilever-shaped sensor with cardiac tissue, the cantilever could be displaced by the contractile behavior of the tissue, even though the modulus of 180 μm-thick IPMC and PDMS is similar, the big difference lies in the thickness of the used material as the flexural rigidity evolves with the cubic of the thickness [13]. The force applied by contractile tissue is in the range of μN [13], therefore thick IPMC with standard Nafion has too high

flexural rigidity to be lifted by cells. The gap between IPMC and bio-MEMS application lies in the fabrication of thin IPMCs with low bending stiffness and sufficient sensing and actuation capabilities. Prior reports studied the different parameters that can influence the electroless deposition for IPMC manufacturing, such as dimensions, concentration of reducing agents, number of reducing cycles, time and temperature [6, 14–18]. However, little explanation and no comparative studies have been reported on commercially available Nafion 212 (50 μm-thick), which is 3.6 times thinner than Nafion 117 (180 μm-thick) and has the same equivalent weight (1100 $g.mol^{-1}$). Arguably, this is because IPMC was originally mainly used in Soft robotics and fuel cells. In soft robotics, thicker IPMC shows higher actuation capabilities [18], whereas in fuel cell thinner Nafion shows higher exchange capabilities, therefore thickness ranging from 20 μm to 180 μm has been poorly studied in the context of IPMC as well as for general purposes.

Influence of manufacturing parameters

Yip *et al.* used the Taguchi method for design of experiments to look for the best IPMC manufacturing parameters. They outlined that a few parameters have a very strong influence on the electroless deposition recipe, such as reducing time and reducing agent concentration [14]. Sode *et al.* reported the crucial importance of hydration level as well as pH to control the depth of Pt deposition in thick Nafion [6]. Nakamura *et al.*, Oh *et al.*, Khmelnitskiy *et al.* and Çilingir and Papila studied the influence of thickness for actuation purposes using hot-pressed resin to manufacture Nafion with different thicknesses ranging from 50 μm to 700 μm [15–18]. Interestingly Nakamura *et al.* and Khmelnitskiy *et al.* also showed the influence of reduction cycle repetitions [15, 17]. However, Oh *et al.* used multi-wall carbon nanotube electrodes, which are not as robust as the platinum-based electrodes fabricated with the electroless deposition technique, as evidenced by delamination issues [16].

IPMC fabrication based on thin Nafion has not been studied in depth, however, insights into the behavior of Nafion 212 shown in literature attest that thin Nafion behaves differently than thick one. Thin Nafion has been reported to exhibit higher water uptake versus swelling ratio, as well as higher ionic conductivity [1, 6, 19]. Ingle *et al.* studied the Pt particles distribution within Nafion 212 for fuel cell membrane manufacturing and with different chemicals than the ones standardly used for IPMC manufacturing [20]. Pak *et al.* reported the manufacturing of thin IPMC (Nafion 212) for micropump application, they were the first to introduce the idea to lower the concentration of reducing agent (2/5 of the original reducing agent concentration) [21]. Fuel cell researchers also studied the impact of Pt deposition on very thin perfluorinated membranes. Kumar *et al.* studied the impact of hydration level on Nafion membranes thinner than 50 μm for fuel cells [22]. While Hawut *et al.* and Hosseinabadi *et al.* studied the influence of electroless deposition parameters for fuel cell applications [8, 23]. The literature points to dilution as a way to improve platinum electroless deposition on Nafion, however, this has not been well described so far for thin IPMC manufacturing.

4.2.1. Electroless deposition standard recipe

The complete procedure for IPMC standard manufacturing including the initial composition process and the final plating is described below :

- Initial composition process
  - Incorporate the tetra-amine platinum chloride Pt(NH3)4HCl into the Nafion membrane by immersion.
  - Reduce the platinum in the membrane using NaBH4 solution (5%) including Polyvinyl-pyrrolidone PVP10 (0.001 M) for miscibility.
- Surface electrodes process
  - Prepare a 240 mL aqueous solution containing 120 mg of Pt with 5 mL of 5% ammonium hydroxide.
  - Reduce the platinum on the surface of the Nafion using 5% aqueous solution of hydroxylamine hydrochloride (6 ml) and a 20% solution of hydrazine monohydrate (3 mL).

4.2.2. Distribution of platinum

Both IPMC substrates, Nafion NRE-212 membrane (thickness 50 μm, Alfa Aesar), here called thin Nafion, as well as the Nafion 117 membrane (thickness 180 μm, Alfa Aesar), here called thick Nafion, were manufactured by electroless deposition of platinum, following the standard recipe described above in section 4.2.1 [3]. The two Nafion membranes have the same equivalent weight (1100 $g.mol^{-1}$). All chemicals have been purchased from Sigma Aldrich and used as received. As already mentioned, Pak *et al.* used 2/5 dilution ratio to increase the performance of the IPMC [21]. Therefore, for the altered recipe the immersion bath was left unchanged, while the $NaBH_4$ mass as well as the PVP10 mass were decreased by 60% in the reduction bath using the same amount of water as previously used for the standard recipe (i.e. dilution factor of 0.4). The mass of the reactants used in the final plating of the diluted recipe (hydroxylamine hydrochloride, hydrazine monohydrate and PVP10) was also decreased by the same amount. After full processing, an IPMC cantilever has been cut with laser (Optec) with the following dimensions : L=18 mm, B=6 mm. Afterward, the IPMC has been cleaned in an HCl (0.1 M) bath, and ions were exchanged in phosphate-buffered saline solution (PBS), a sodium-based medium commonly used to wash cells and biological samples.

To obtain a clean IPMC cross-section, the IPMC has been immersed in liquid nitrogen and cleaved. Pictures of the cross-section have been taken using scanning electron microscopy (SEM) (Jeol JSM-6010LA). Energy-dispersive X-ray spectroscopy (EDS) and image processing were used to characterize the platinum distribution. In EDS, an electron beam hits the inner electronic shell of an atom, knocking off an electron from the shell, while leaving a positively charged electron-hole (Figure 4.5). When the electron is displaced, it attracts another electron from an outer shell to fill the vacancy. As the electron moves from the outer higher-energy to the

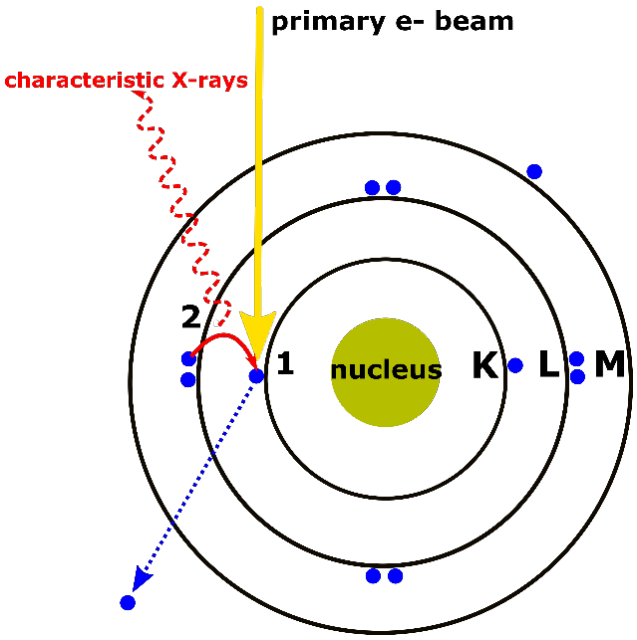

Figure 4.5: Principle of energy dispersive X-ray spectroscopy (EDS), electrons are bombarded towards an element of interest, the electrons leave an energy state and release an x-ray beam, specific to an element. Extracted from [24]

inner lower-energy shell of the atom, this energy difference can be released in the form of an X-ray. The energy of this X-ray is specific to the element.

A region of interest has been extracted in order to select the dedicated area with the electrodes (Fig. 4.6 a). EDS has been used to localize the Pt particles and the Nafion in the cross-section (Fig. 4.6 b). The position of the Pt particles has been extracted using Python 3.6 and Open Computer Vision library (OpenCV) (Fig. 4.6 c). EDS fluorine detection has been used to obtain a precise pixel-to-μm ratio as the thickness of Nafion was known (180 μm or 50 μm) (Fig. 4.6 d). Platinum distribution has been normalized using the amount of fluorine detected in the cross-section for every sample, as fluorine concentration was assumed equal for every sample given the same starting material. The distribution is not meant to be absolute but relative in order to perform a comparison from one picture to another.

The spatial resolution of EDS has been estimated using the Castaing formula (Eq 4.1) and the standard value of Nafion Density (1.59 kg/m3). The minimum emission voltage used was the one from carbon as the fluoropolymer is made of carbon and fluorine. The acceleration voltage used for the EDS was 5kV. Using Castaing's formula we estimated that the spatial resolution depth for the fluorine is 0.670 μm, while for platinum it is 0.79 μm.

$$Zm = 0.033 \cdot ((E_0)^{1.7} - (E_C)^{1.7}) * \frac{A}{\rho * Z} \tag{4.1}$$

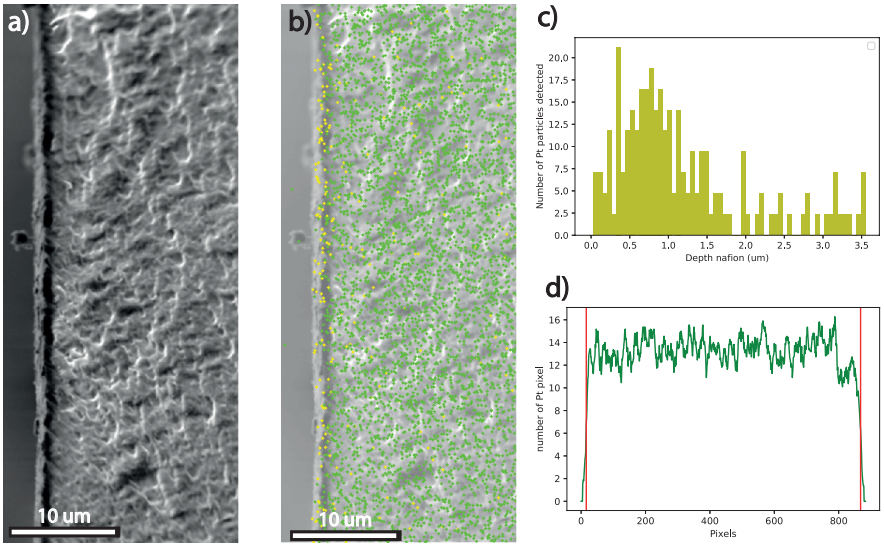

Figure 4.6: a) SEM picture of the cross-section of thick IPMC. b) SEM picture overlap with EDS of platinum and fluorine after one reduction step (green: fluorine, yellow: platinum). c) Platinum distribution at the electrode inside Nafion after one reduction step. d) Fluorine distribution for the entire thickness of the IPMC.

The results for the repeated immersion-reduction steps of the 50 μm-thick Nafion are presented in Figure 4.7. Pt distributions after the first reduction step of 50 μm and 180 μm-thick samples are compared in Fig. 4.8. The Pt distribution for Nafion 212 (50 μm thick) using the diluted recipe is shown in Fig. 4.10.

Thanks to the high precision of tools and image processing, the effect of repeated immersion-reduction steps can clearly be seen in the pictures of the cross-section for the thin IPMC which went under the standard electroless recipe (Fig. 4.7). The effect of repeated cycles could hardly be seen on the previously published Pt distribution profiles within standard Nafion [4, 25]. It is apparent from the distributions that the reduction steps follow one another in-depth, i.e. the last reduction acts deepest in the membrane while the first reduction happens in the proximity to the surface. The overall electrode thickness after 3 cycles is about 8 μm (Fig. 4.7).

Interestingly, we could show that the Pt distribution differs strongly between thin and thick Nafion after one reduction step, while the two samples were immersed in the same immersion bath and reduced in the same reduction bath during the first stage of the initial composition process (Fig. 4.8). The number of platinum particles detected is different, meaning that, despite the fact that both samples are coming from the same baths, more platinum was reduced at the interface in the

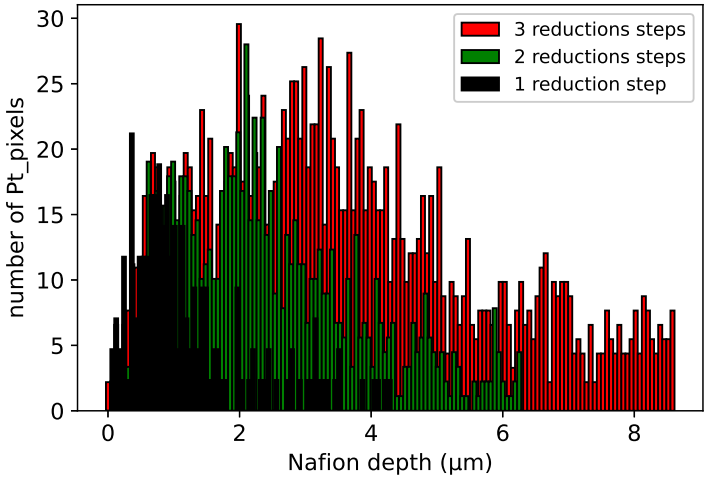

Figure 4.7: Platinum distribution within the thin Nafion 212 membrane for one (black), two (green), and three (red) reduction steps.

thin Nafion than in the thick Nafion. The difference in Pt distribution is therefore to be correlated with the difference in geometry used (thick versus thin membrane) as both samples are made of the same material with the same equivalent weight. It has been reported in the literature that Nafion behaves dynamically in correlation to the electrolyte concentration [26] and that thinner Nafion experiences higher water uptake [27]. Kusoglu *et al.* reported that a higher water uptake leads to higher diffusion coefficients in Nafion. Therefore Nafion 212, which has a higher water uptake than Nafion 117, gives rise to a faster reduction close to the surface of the Nafion. In addition, we can hypothesize that a PFSA membrane with higher water uptake experiences higher solvation, helping the charged species to move inside the polymer backbone, further promoting interaction between the reducing agent and the reactant to be reduced.

As shown by Hsu *et al.* in their cluster network model, the ionic channels and networks are bigger and more connected in Nafion that absorbs more water than in the one with smaller water uptake capability [28]. Therefore we hypothesize that the ionic cluster network reorganizes differently in the thin Nafion in comparison to the thick Nafion, allowing the chemicals involved in the reduction process to react more on the surface of Nafion (Fig. 4.9). Accordingly, thin Nafion has wider ionic channels and higher connectivity, therefore there are more interactions between the $NaBH_4$ and the Pt organometallic as there is more space for the chemicals to react (Fig. 4.9). We hypothesize that bigger and more connected ionic clusters increase the ion mobility, allowing the Pt organometallic from bulk Nafion to migrate toward the surface electrode as well as $NaBH_4$ to react faster with the incoming organometallic. This may explain why platinum is reduced deeper into thick Nafion

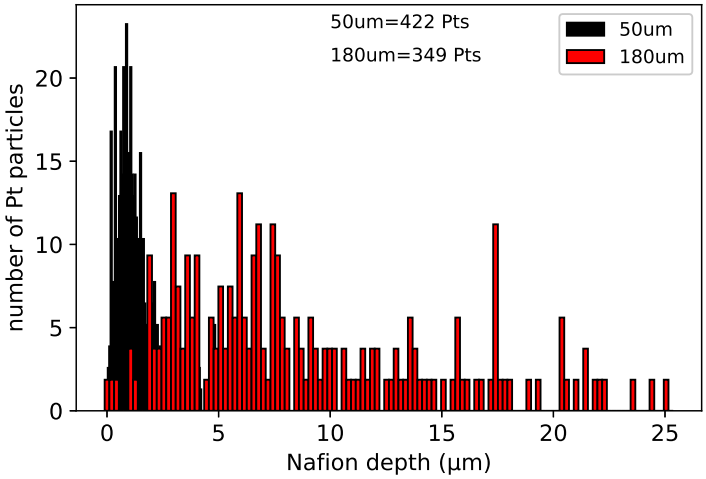

Figure 4.8: Platinum distribution within thin and thick Nafion after one reduction step immersed for 30 mins using the standard recipe. The number of points detected is reported, more platinum particles have been detected in the thin Nafion than in the thick one.

than in thin Nafion that went through the same immersion bath and reduction step (Fig. 4.8). These claims are also in line with the results of Sode *et al.*, who studied the influence of parameters on Nafion 117 [6]. They showed that the kinetics of the electroless reaction is mostly dependent on the hydration state of the Nafion. Moreover Millet *et al.* reported that the diffusion rate inside the Nafion membrane can be determined by bulk diffusion (M mechanism) or by interfacial diffusion (F mechanism) [25]. Our results suggest that inside Nafion 212 the rate of precipitation is based on the M mechanism as the water uptake capability of the PFSA membrane mostly influences the diffusion inside the membrane [25].

Diminishing the concentration of the chemicals allows to reduce the platinum closer to the surface, giving more localized electrodes [30], and alleviating the influence of the diffusion inside the membrane. In the platinum distribution of the final sample that went through the three reduction steps by using the diluted recipe, 75% of platinum is homogeneously localized within 2.62 μm of the Nafion depth (Fig. 4.10), while 90% of the particles have been detected within 4.42 μm. It should be pointed out also that the maximum detected amount of platinum is double of the amount detected at the highest peaks for non-diluted recipe (50 instead of 25). Unlike the Nafion 212 that went through the 3 reduction steps in the non-diluted recipe (Fig. 4.7), in the diluted recipe sample the effect of repeated reductions cannot be seen (Fig. 4.10). This supports that the platinum deposited during the second and third steps predominantly stays at the interface of the Nafion, most probably on the already-grown platinum sites after the first reduction. These results comply with the aforementioned assumptions that the mechanism of precipitation

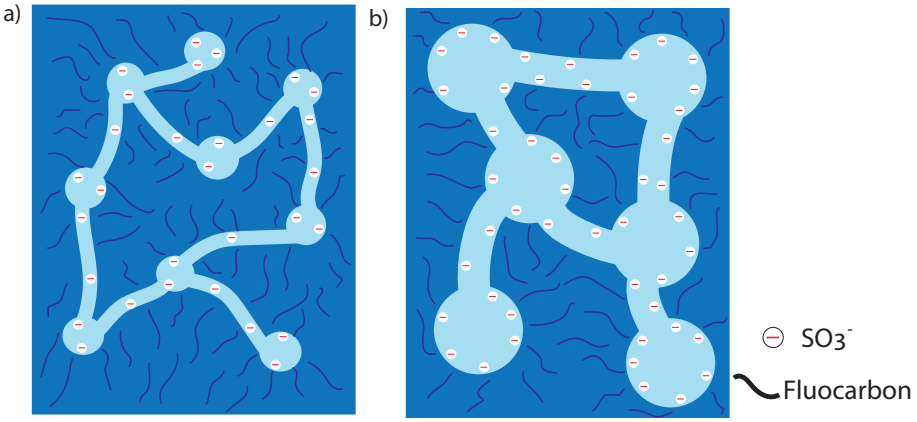

Figure 4.9: Ionic cluster model in Nafion, a) Ionic cluster reorganization at low water uptake b) Ionic cluster reorganization at high water uptake. (Adapted with permission from [29]).

in the Nafion 212 is determined by diffusion inside the membrane (M mechanism) and not by diffusion inside the boundary layer (F mechanism). In addition, by using dilution, we limit the bubbling during the reactions. This helps to keep the thin IPMC sunk into the solution, reducing the fabrication errors inherent to electroless deposition and therefore increasing reproducibility.

The distribution of platinum within Nafion 117 has already been studied by Millet *et al.* [25]. The Pt distributions thereby reported strongly differ from the profiles we obtained (Fig 4.10 Fig 4.11 and Fig 4.12). In the aforementioned profiles (thick Nafion), the maximum Pt concentration is located at the liquid-substrate boundary of the Nafion membrane, whereas the Pt distribution in Nafion 212 reaches the maximum inside the Nafion membrane, between 0.5 µm and 1 µm below the surface (Fig 4.11 and Fig 4.12).

The position of the peaks in our experimental data suggests that the mechanism determining the Pt precipitation rate inside Nafion 212 is diffusion inside the membrane while using Nafion 117 with the same reducing agent concentration leads to a precipitation rate determined by diffusion at the liquid/film boundary. As already mentioned it has been proven experimentally that ionic conductivity and water uptake of Nafion 212 is higher than for Nafion 117 [1]. We could obtain a good fit of the Pt distribution ($R^2 = 0.919$ and $R^2 = 0.945$) within Nafion 212 with the Rayleigh distribution for immersion time of 30 minutes and 2 hours respectively:

$$f(x, \sigma^2) = \frac{x}{\sigma^2} \exp \frac{-x}{\sigma^2} \tag{4.2}$$

4.2.3. Surface morphology and resistivity

The surfaces of the IPMCs that were produced using the standard and altered recipe were characterized using SEM and atomic force microscopy (AFM) to study the surface roughness and connection between platinum layers. The AFM set-up was

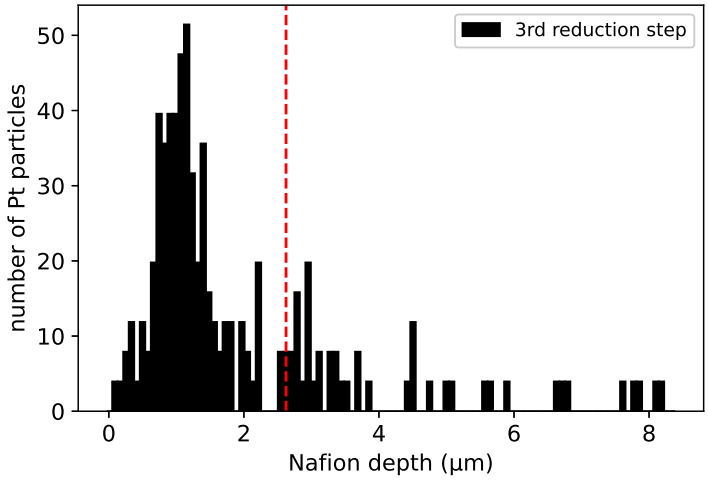

Figure 4.10: Platinum distribution for the Nafion 212 membrane using the diluted recipe after 3 reductions steps. 75% of the particles have been detected within 2.62 μm from the surface (red dashed line).

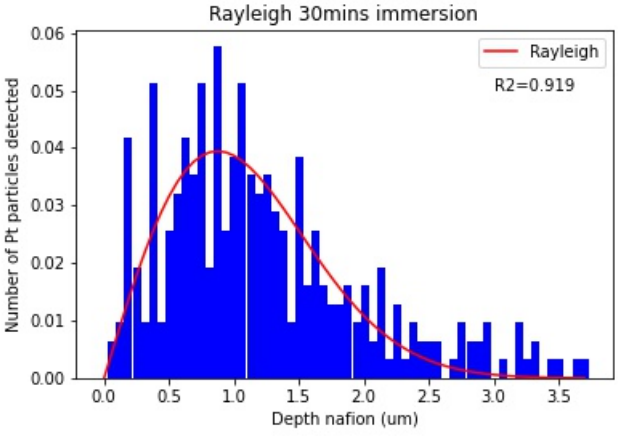

Figure 4.11: Rayleigh fit of platinum distribution within Nafion 212 for a 30min immersion bath.

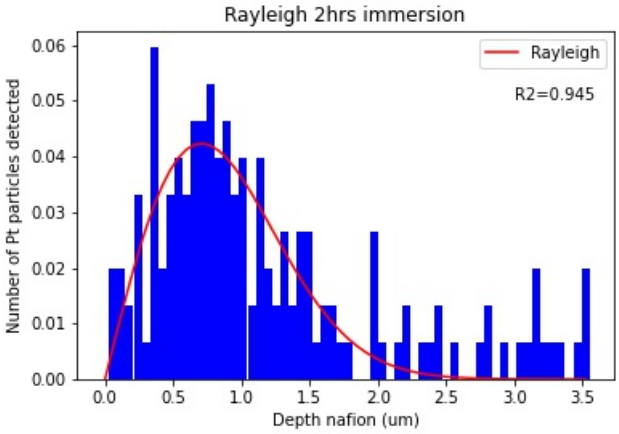

Figure 4.12: Rayleigh fit of platinum distribution within Nafion 212 for a 2hrs immersion bath.

a ND-MDT Aura, operated in semi-contact mode with a cantilever having a radius smaller than 10 nm (Nanosensors), at a frequency of 0.80 Hz and acquiring 256 lines on areas of 1 μm^2 and 10 μm^2 respectively. The sheet resistance of the two samples (diluted and non-diluted) has been measured using the van der Pauw method with a 4-probe station (Cascade 31, Summit) using a 400 mV range.

Van der Pauw measurements

The sheet resistance measurements are plotted in a heat map format in Fig. 4.13. The conductivity of the electrodes strongly depends on the electroless deposition recipe, as already shown by Shahinpoor *et al.* [31]. The final resistivity of the electrodes mostly depends on the initial composition process that grows the first sites of platinum prior to the surface electrodes process. Diminishing the surface resistivity by controlling closely the manufacturing process will lead to a better distribution of the charges along the length of the material and will result in better transducer capabilities [31].

As one can expect from the SEM and AFM images, resistivity is higher for the non-diluted recipe than for the diluted recipe (Fig. 4.13). We also noticed during the van der Pauw measurements that many points for the non-diluted recipe could not be measured as the resistance was too high (open circuit). The mean value calculated for the sheet resistance of the diluted recipe is 22.06 Ω for a $1mm^2$ area (N=36) with a standard deviation of 5.94 Ω/mm^2.

We hypothesize that by using the dilution factor on the thin IPMC we obtained better-defined sites with platinum being deposited on the surface of Nafion during the initial composition process. Those sites are the ones where the platinum grows during the surface electrodes process, leading to a higher connection of the platinum particles. Conversely, for the standard recipe, after the initial composition, the Pt sites are more numerous and more concentrated in the bulk (Fig. 4.7).

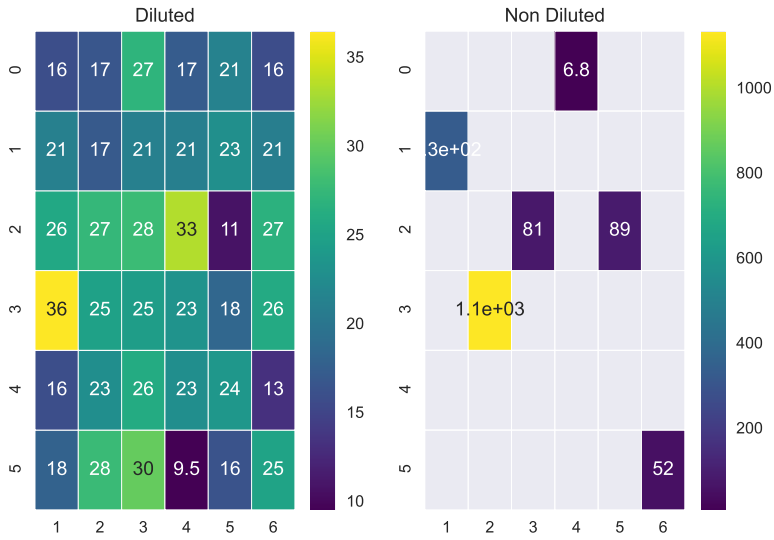

Figure 4.13: Surface resistance measured for diluted and non-diluted samples (values are in Ω). The blank rectangles indicate no current flow through these areas.

Electrodes surface morphology

The results of the surface morphology of the 50 μm samples that went through the entire manufacturing process using the diluted recipe and non-diluted recipe are shown in Fig. 4.14. The platinum particles deposited on the surface of the thin Nafion for the diluted recipe showed a homogeneous layer with particles connected together (Fig 4.14 a). We hypothesize that in this case, the growth of the Pt particles is happening within the same plane of the Nafion sheet, due to the dilution. On the contrary, the thin Nafion with non-diluted recipe showed a non-homogeneous layer with little connection between the Pt particles and grainy look (Fig. 4.14 b). We hypothesize that the reaction predominantly happening at the interface between the Nafion and the reduction bath (F mechanism) leads to the development of the Pt particles in a plane perpendicular to the one of the Nafion sheet. Thus the Pt particles grow in height for the non-diluted recipe while growing in width for the diluted recipe, giving different appearances (Fig. 4.14).

It should be pointed out that the root mean square (RMS) surface roughness for the diluted recipe (51.6 ± 4.3 nm) is higher than for the non-diluted recipe (39.1 ± 6.9 nm). The difference might come from the fact that the connection of the platinum particles is not complete, leaving large gaps between the Pt particles as seen on the SEM pictures of the diluted recipe (Fig 4.14 a). On the other hand, the non-diluted recipe leads to a more grainy structure with smaller gaps between the Pt particles, therefore resulting in a lower roughness.

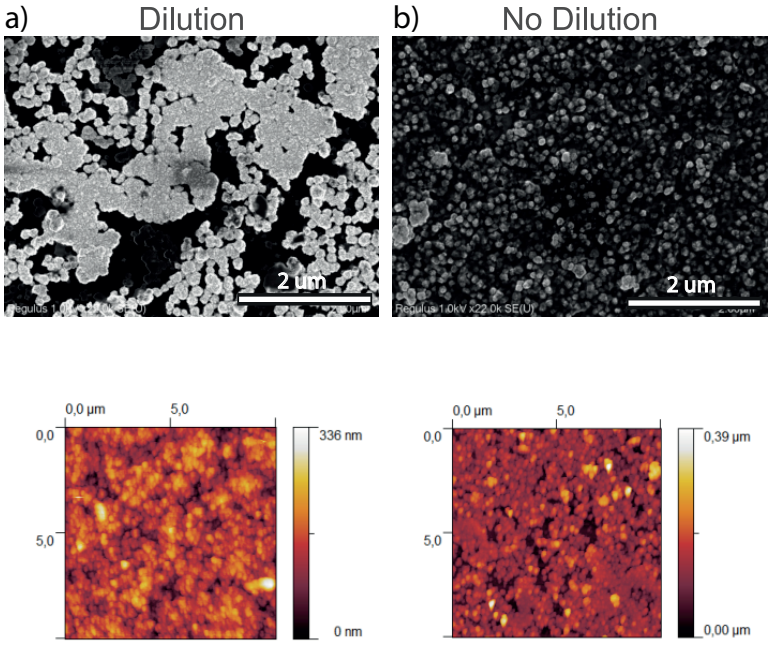

Figure 4.14: SEM (top) and AFM (bottom) pictures of surface electrodes for the diluted recipe a) and for the standard recipe b) for 50μm thick IPMC.

4.3. Characterization of the sensing capabilities

Sensing with IPMCs can be implemented using active or passive methods. Active sensing relies on the fact that the IPMC develops charge imbalance when deformed, measurable via charge, current or voltage measurement circuits [32]. Passive sensing considers the IPMC as capacitance or resistance so that when a signal is sent, the drop in resistance or capacitance due to displacement is used as a recording signal. In the first case, the IPMC is called active as the material delivers energy while in the second mode, the material is considered as a passive element that disturbs the sent signal [32]. Here we have developed an electronic board for sensing the charge produced on the IPMC electrodes [32]. IPMC electrodes are connected through gold contacts to the board input. The first stage of the board is made of a charge amplifier circuit with gain G=100. The signal is sent to an instrument amplifier (G=1), then a second-order passive low-pass filter with cut-off frequency of 1125 Hz is used to filter out high-frequency noise. Data are saved in real-time on a memory card. Impulse excitation technique (IET) was used to induce controlled displacement to the IPMC cantilever. Oscillations were induced by unit step excitation at the IPMC base, and displacements at the IPMC tip were measured. The unit step excitation was induced through a loaded spring (Thorlabs). Oscillations were measured using a laser displacement sensor (ILD 1750-2 Micro epsilon)

and through the developed electronics to extract sensitivity (Fig. 4.15). Prior to the impulse, the IPMC was refilled with PBS solution using a pipette and the measurements have been performed shortly after to maintain the IPMC hydrated. The recorded data were further processed with custom Python 3.6 code to extract the oscillation amplitude and natural frequency of the cantilever.

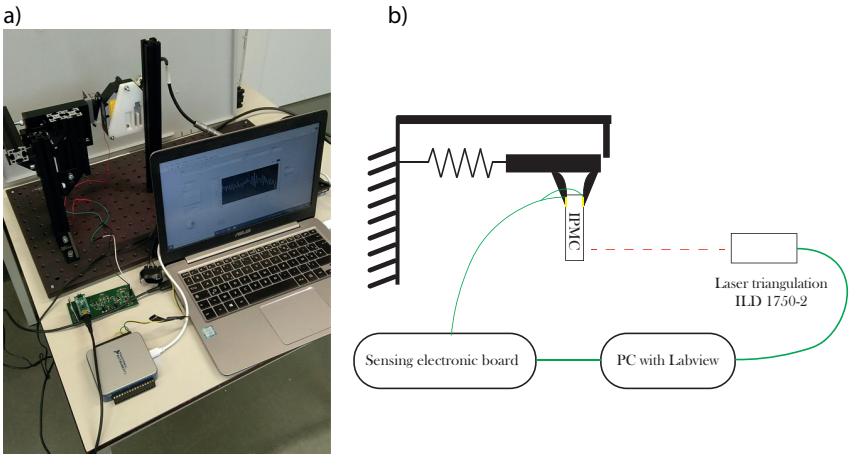

Figure 4.15: a) Impulse excitation setup used to characterize the IPMC and its responsivity. b) Schematic of the setup, the IPMC is loaded on an arm connected to a spring, upon release of the spring the IPMC will oscillate. Oscillation will be recorded with a laser triangulation system as well as by the developed electronic board.

The oscillations recorded by the laser position system corresponded to the oscillations recorded by the electronics (Fig. 4.16 and Fig. 4.17, respectively). For each oscillation, the tip displacement (peak-to-peak) measured by the laser triangulation has been correlated to the recorded voltage (peak-to-peak). Mean and standard deviation values were used to compose the responsivity curve (Fig. 4.18). Data for 30 oscillations show a good fit with a first-order polynomial ($47.6\ x - 11.6$) ($R^2 = 0.99$). We noticed that dispersion in responsivity was mostly coming from high amplitude oscillations (Fig. 4.18). We also noticed that the drying of the thin IPMC increased the dispersion after a few minutes. During the experiments, the water leaves the IPMC, changing the material characteristics (ions mobility) and responsivity. This effect could be avoided when using this material in a wet environment, as it is typically the case for bio-MEMS (muscular thin film platform [13]). The smallest tip displacement detected electrically (960 μm peak- to-peak for a 16 mm-long IPMC) was recorded as a 0.39 mV voltage output (prior to amplification) (red and blue dots in Fig. 4.16, 4.17). As a comparison, Wang *et al.* were able to obtain a 0.32 mV amplitude signal by using a 50 μm-thick IPMC (20 mm-long) at maximum displacement (10mm). However Wang *et al.* manufactured the thin IPMC in a different way, using electroplating after electroless deposition and Pd based electrodes, known for their lower stiffness [12]. However, electrolpating is known not to be as stable chemically and mechanically as electroless deposited

material. The calculated sensitivity is S=47.6 $\pm$ 2.0 mV/mm after amplification (G=100) and 0.476 mV/mm without amplification, which can be compared to the value found by Khmelnitskiy *et al.* (0.072 mV/mm without amplification). The authors used a standard IPMC with Nafion 117 [33], showing lower flexibility than our IPMC because of its inherent thickness, which can explain the difference of sensitivity.

The limit of detection (LOD) is a key figure of merit to assess the performance of the fabricated sensor. The LOD refers to the minimum signal that can reliably be considered as a displacement from the reference position [34, 35]. The limit of detection with a 90% confidence level is $LOD = \frac{3\sigma}{S}$, S being the sensitivity of the sensor and σ the standard deviation of the noise, recorded by the electronics board when the beam its undeflected rest position (Fig. 4.17 red dashed line). We calculated σ as 7.9 mV, the slope being 47.6 $\pm$ 2.0 mV/mm. Therefore the limit of detection for our sensor is 500 $\pm$ 20 μm.

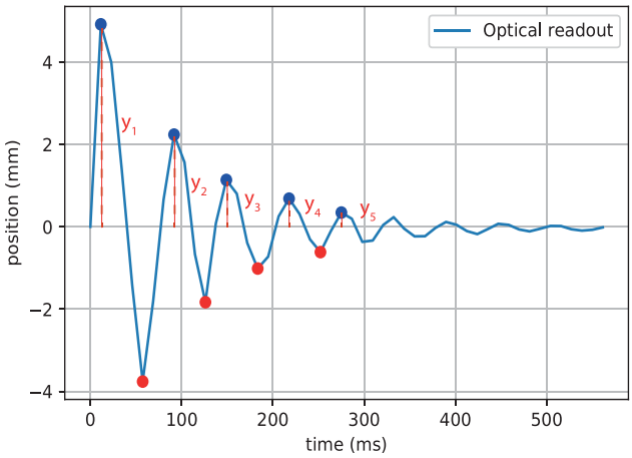

Figure 4.16: a) Oscillations of a 50 μm-thick IPMC from diluted recipe recorded through the laser position system. y_i are the points used to compute the logarithmic decrement and damping. The points used to calculate the amplitude are in red and blue.

4.3.1. Long-term sensitivity assessment

After 6 months of storage in deionized water, the impulse excitation characterization methods has been performed again on the same sample. Results are plotted in Figure 4.19. We notice that only the first oscillation can be seen while the smaller ones cannot be detected. We have measured that the first oscillation amplitude is 8.6mm for a 93mV output (Figure 4.19). Therefore the estimated sensitivity is lower than when the sample was used as manufactured. We hypotesized that the handling of the thin IPMC as well as the tests performed in air might lead to shrinkage of the material, leading to potential cracks on the electrodes.

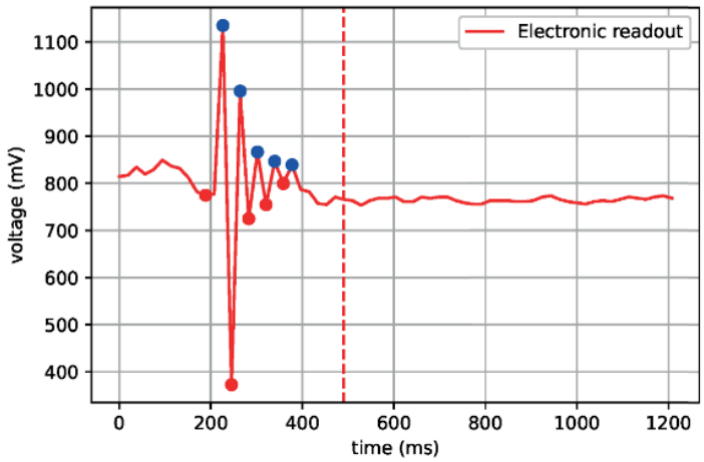

Figure 4.17: b) Oscillations of the same IPMC sample recorded through the electronic board. Points used to calculate the amplitude are in red and blue. Points used to calculate σ (standard deviation of the noise floor) are extracted starting from the red dashed line.

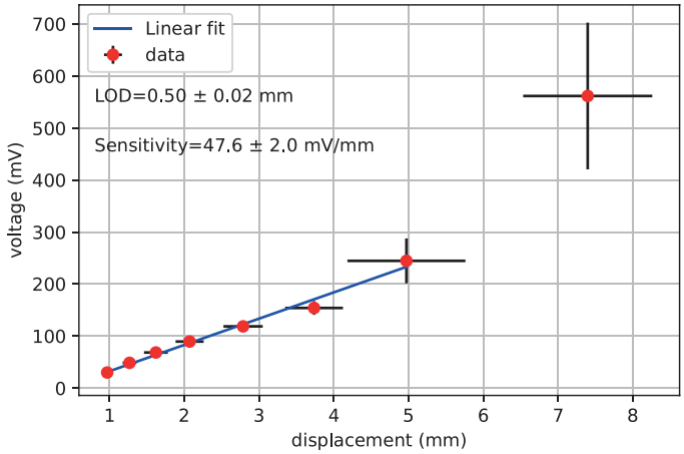

Figure 4.18: Responsivity plot for 50 μm-thick IPMC from diluted recipe for 30 oscillations. Linear fit used to calculate the sensitivity ($R^2 = 0.99$).

4.3.2. Repeatability

Repeatability has been investigated by performing the exact same measurement on different samples. Five samples coming from the same manufacturing batch were used for the sensing tests. The repeatability of the measurement has been investigated by performing measurements with long time intervals in between (days). We noticed that the sensor shows good repeatability as long as the IPMC is stored in a wet environment. We should point out that the setup used to characterize the sample might influence the measurement as the quality of the connection with the

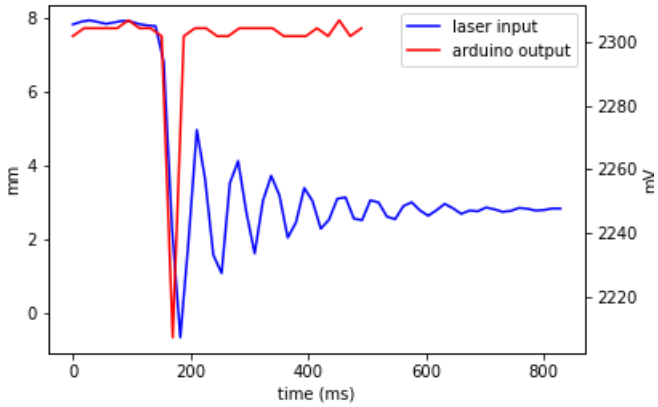

Figure 4.19: Oscillation recorded through the laser (blue), and the response of the IPMC (red) Sample 1 after 6 months storage in deionized water.

gold electrodes might differ slightly from one experiment to the other (clamping) as well as the position of the laser on the IPMC sample. Examples of the impulse output have been plotted in Figure 4.20 and Figure 4.21.

For every sample it was possible to use the IPMC as a senor, most often the first oscillation is detectable. From the different sensing tests performed only results from sample 1 (Figure 4.17) has been used to characterize the material as this is the sample showing several oscillations as well as damping. We hypothesized that the sensitivity setup is the main hurdle, inherently producing disparities between responses, nevertheless from our experiments we could always sense a response of the thin IPMC material, especially for the largest oscillation (first one).

4.4. Young's modulus estimation and flexural rigidity of IPMC

Extracting the mechanical parameters of an IPMC is of crucial importance when developing a sensor as mechanical stiffness will influence flexural rigidity. Excitation techniques already have been used to characterize the mechanical properties of IPMC such as Young's modulus [36]. As already seen from the results of mechanical characterization, upon impulse excitation the IPMC beam exhibits a damped simple harmonic oscillator behavior. The logarithmic decrement δ (Eq. 4.3, y_i being the amplitude of the i^{th} oscillation) can be used to estimate the damping of the system ζ (Eq. 4.4). From the estimation of the damping, the natural frequency w_0 can be estimated using the resonance frequency w (Eq. 4.5).

$$\delta = \frac{1}{n} \ln \frac{y_i}{y_{i+n}} \tag{4.3}$$

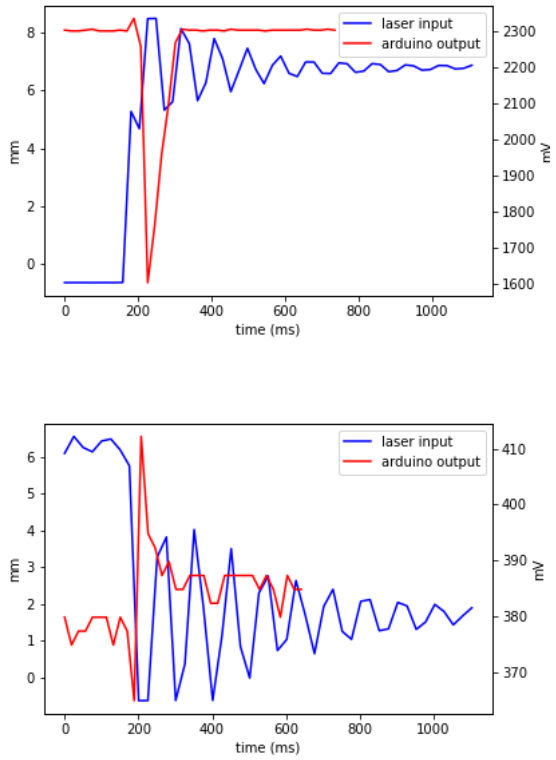

Figure 4.20: Oscillations recorded through the laser (blue) and through the electronic board (red) for Sample 3 (top) and for Sample 4 (bottom). The first (largest) oscillation can be correlated to the electronic output signal.

$$\zeta = \sqrt{\frac{\delta^2}{4\pi^2 + \delta^2}} \tag{4.4}$$

$$w = \sqrt{w_0^2 - 2\zeta^2} \tag{4.5}$$

$$E = \frac{mL^3}{I}\left(\frac{w_i}{\alpha_i^2}\right)^2 \tag{4.6}$$

As reported by Barboni *et al.* Young's modulus E can be estimated using Eq. 4.6, with I being the moment of inertia of plain area $I = \frac{BH^3}{12}$, B being the width, H the height, L the length, m the mass and α_i a dimensionless coefficient for the i^{th} resonance frequency of the cantilever beam. The mass of the IPMC has been estimated

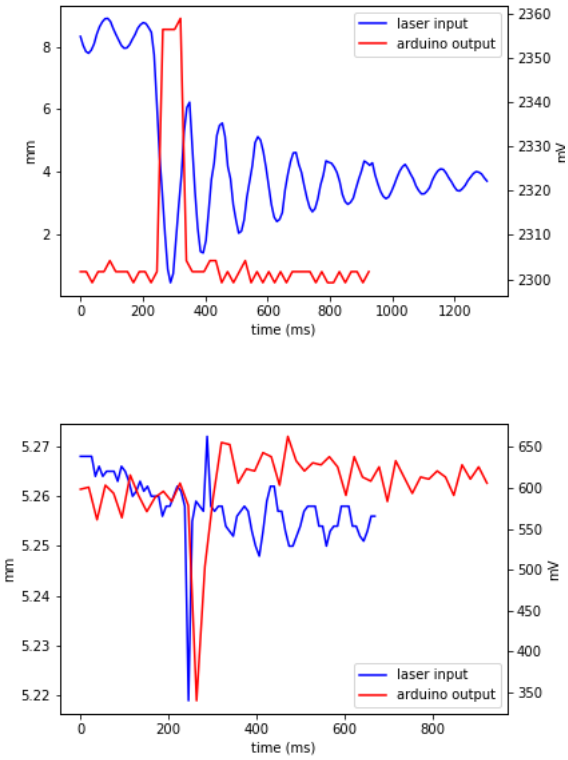

Figure 4.21: Oscillations recorded through the laser (blue) and through the electronic board (red), for Sample 4 (left) and Sample 5 (right), the oscillation (500 μm) can be correlated to the electronic output signal despite inherent noise.

using a precision balance (Allscales Europe) and the mean value was calculated from 15 measurements. 30 oscillations recorded through the aforementioned laser triangulation system have been used to estimate the resonance frequency of the cantilever. The mean value has been extracted to calculate Young's modulus. The flexural rigidity D of the beam has been calculated using the relation $D = EI$.

The oscillations recorded through the laser were used to estimate Young's modulus (Fig. 4.16). The estimated logarithmic decrement was 0.7082, the estimated damping was 0.1120 (N=10, standard deviation=0.06). The mean of 30 oscillations period was found to be 75 ms, giving a resonance frequency of the beam of 13.2 Hz. In the end, the estimated Young modulus was 550 MPa, a value close to that already found for standard IPMC [32]. This value shows that, despite the more localized platinum electrodes of the surface of the Nafion, Young's modulus is still mostly influenced by the bulk material (PFSA).

The flexural rigidity D of our IPMC beam has been calculated to be $3.43\ \ 10^{-8}$

$N.m^2$. Since the material is 3.6 thinner than standard IPMC, the overall flexural rigidity is largely lower in comparison to standard IPMC as the moment of inertia evolves with the cubic of the beam's height.

4.5. Conclusion

In this chapter, we have presented a complete study of the fabrication of thin IPMC for MEMS and organ-on-chip application based on oxidation-reduction reaction. A comparative study has been performed on the electroless deposition of platinum within thick and thin Nafion membranes. The standard recipe cannot be used for thinner PFSA membranes because of the dynamic properties of PFSA material. We have successfully manufactured a thin IPMC (50 μm thick) for sensing applications using platinum electroless deposition. The difference in platinum distribution for thick and thin IPMC has been shown by comparing the distribution of platinum in Nafion 212 and Nafion 117 that went under the same electroless deposition recipe. We hypothesized that the difference of water uptake explains the difference in Pt distribution for the two samples. Accordingly, the thin polymer is more solvated than the thick one, allowing enhanced displacement of reactants within the polymer backbone and improved ionic cluster reorganization. Overall, reactants have more freedom to distribute and move within the thin Nafion than the thick Nafion. These assumptions suggest that the dynamics of precipitation within thin Nafion is rate-determined by membrane diffusion (M mechanism). Pt profiles have been fitted with a Rayleigh distribution and show maximum peak within the material, suggesting that the dynamic of the reaction is rate-determined by diffusion inside the membrane and not by the boundary layer interface. We have shown that using dilution we can restrain the reaction in order to better control the deposition of Pt on a thin Nafion membrane. The resulting electrodes showed higher conductivity and a higher amount of platinum close to the surface of the PFSA membrane.

Limiting the precipitation reaction by using a dilution factor is the key to manufacturing a functional thin IPMC sensor. Constrained electrolyte concentration leads to denser sites during primary plating, which leads to more localized sites for the Pt to be deposited during the following reduction step and final plating. We have characterized the resulting material and showed that it could be used for sensing in the microscale range by means of an active, charge-based sensing setup. In the future, hydrogel materials could be used to create a more compliant layer on top of the thin IPMC sensor for bio-MEMS applications.

This work could represent a milestone for the further development of IPMC in different fields. The flexural rigidity of the thin IPMC we obtained is largely lower than for standard IPMC, expanding potential application for sensing. Further investigations could be performed by using different thicknesses of Nafion and different dilution factors. Fitting the distribution of platinum with existing models on the precipitation process within PFSA may provide additional insight. In addition, in order to explore potential applications, electronics could be further developed that could amplify and filter the recorded signal in the frequency range of interest, depending on the explored application (e.g. humidity, strain, or force sensors).

In the next chapter, one potential application of the thin IPMC developed in the current chapter is presented. Similarly to the work presented in Chapter 2, tissue is grown on top of the thin cantilever shape IPMC, and soft lithography, as well as hydrogel-based techniques, are explored in order to grow matured and aligned tissue on top of the smart material.

References

[1] A. Kusoglu and A. Z. Weber, *New Insights into Perfluorinated Sulfonic-Acid Ionomers,* Chemical Reviews **117**, 987 (2017).

[2] L. Yang, H. Wang, and X. Zhang, *Recent progress in preparation process of ionic polymer-metal composites,* Results in Physics **29**, 104800 (2021).

[3] K. J. Kim and M. Shahinpoor, *Ionic polymer metal composites: II. Manufacturing techniques,* Smart Materials and Structures **12**, 65 (2003).

[4] P. Millet, M. Pineri, and R. Durand, *New solid polymer electrolyte composites for water electrolysis,* Journal of Applied Electrochemistry **19**, 162 (1989).

[5] K. Asaka, K. Oguro, Y. Nishimura, M. Mizuhata, and H. Takenaka, *Bending of Polyelectrolyte Membrane–Platinum Composites by Electric Stimuli I. Response Characteristics to Various Waveforms,* Polymer Journal **27**, 436 (1995), number: 4 Publisher: Nature Publishing Group.

[6] A. Sode, N. J. C. Ingle, M. McCormick, D. Bizzotto, E. Gyenge, S. Ye, S. Knights, and D. P. Wilkinson, *Controlling the deposition of Pt nanoparticles within the surface region of Nafion,* Journal of Membrane Science **376**, 162 (2011).

[7] B. Bhandari, G.-Y. Lee, and S.-H. Ahn, *A review on IPMC material as actuators and sensors: Fabrications, characteristics and applications,* International Journal of Precision Engineering and Manufacturing **13**, 141 (2012).

[8] W. Hawut, M. Hunsom, and K. Pruksathorn, *Platinum electroless deposition on nafion membrane for PEM fuel cells,* Korean Journal of Chemical Engineering **23**, 555 (2006).

[9] H. Yanamori, T. Kobayashi, and M. Omiya, *Ionic Polymer Metal Composite (IPMC) for MEMS Actuator and Sensor,* (2012) pp. 417–424.

[10] S. Tsuchitani, K. Kikuchi, I. Shimizu, T. Taniguchi, and H. Miki, *IPMC Actuators Fabricated Using MEMS Technology,* Advances in Science and Technology **97**, 57 (2016).

[11] G.-H. Feng and R.-H. Chen, *Improved cost-effective fabrication of arbitrarily shaped uipmc transducers,* Journal of Micromechanics and Microengineering **18**, 015016 (2007).

[12] J. Wang, Y. Wang, Z. Zhu, J. Wang, Q. He, and M. Luo, *The Effects of Dimensions on the Deformation Sensing Performance of Ionic Polymer-Metal Composites,* Sensors **19**, 2104 (2019).

[13] J. U. Lind, M. Yadid, I. Perkins, B. B. O'Connor, F. Eweje, C. O. Chantre, M. A. Hemphill, H. Yuan, P. H. Campbell, J. J. Vlassak, and K. K. Parker, *Cardiac Microphysiological Devices with Flexible Thin-Film Sensors for Higher-Throughput Drug Screening,* Lab on a chip **17**, 3692 (2017).

[14] J. Yip, L. S. Feng, C. W. Hang, Y. C. W. Marcus, and K. C. Wai, *Experimentally validated improvement of IPMC performance through alternation of pretreatment and electroless plating processes,* Smart Materials and Structures **20**, 015009 (2010).

[15] T. Nakamura, T. Ihara, T. Horiuchi, T. Mukai, and K. Asaka, *Measurement and Modeling of Electro-Chemical Properties of Ion Polymer Metal Composite by Complex Impedance Analysis,* SICE Journal of Control, Measurement, and System Integration **2**, 373 (2009).

[16] C. Oh, S. Kim, H. Kim, G. Park, J. Kim, J. Ryu, P. Li, S. Lee, K. No, and S. Hong, *Effects of membrane thickness on the performance of ionic polymer–metal composite actuators,* RSC Advances **9**, 14621 (2019).

[17] I. K. Khmelnitskiy, L. O. Vereshagina, V. E. Kalyonov, A. P. Broyko, A. V. Lagosh, V. V. Luchinin, and D. O. Testov, *Improvement of manufacture technology and research of actuators based on ionic polymer-metal composites,* Journal of Physics: Conference Series **857**, 012018 (2017), publisher: IOP Publishing.

[18] H. D. Çilingir and M. Papila, *"Equivalent" Electromechanical Coefficient for IPMC Actuator Design Based on Equivalent Bimorph Beam Theory,* Experimental Mechanics **50**, 1157 (2010).

[19] C. Feng, Y. Li, K. Qu, Z. Zhang, and P. He, *Mechanical behavior of a hydrated perfluorosulfonic acid membrane at meso and nano scales,* RSC Advances **9**, 9594 (2019).

[20] N. J. C. Ingle, A. Sode, I. Martens, E. Gyenge, D. P. Wilkinson, and D. Bizzotto, *Synthesis and Characterization of Diverse Pt Nanostructures in Nafion,* Langmuir **30**, 1871 (2014).

[21] J. J. Pak, J. Kim, S. W. Oh, J. H. Son, S. H. Cho, S.-K. Lee, J.-Y. Park, and B. Kim, *Fabrication of ionic-polymer-metal-composite (IPMC) micropump using a commercial Nafion,* in *Smart Structures and Materials 2004: Electroactive Polymer Actuators and Devices (EAPAD)*, Vol. 5385 (International Society for Optics and Photonics, 2004) pp. 272–281.

[22] P. Kumar, R. P. Bharti, V. Kumar, and P. P. Kundu, *Chapter 4 - Polymer Electrolyte Membranes for Microbial Fuel Cells: Part A. Nafion-Based Membranes,* in *Progress and Recent Trends in Microbial Fuel Cells*, edited by P. P. Kundu and K. Dutta (Elsevier, 2018) pp. 47–72.

[23] P. Hosseinabadi, M. Javanbakht, L. Naji, and H. Ghafarian-Zahmatkesh, *Influence of Pt Nanoparticle Electroless Deposition Parameters on the Electrochemical Characteristics of Nafion-Based Catalyst-Coated Membranes,* Industrial & Engineering Chemistry Research **57**, 434 (2018).

[24] *Eds how does it work,* (2019).

[25] P. Millet, R. Durand, E. Dartyge, G. Tourillon, and A. Fontaine, *Precipitation of Metallic Platinum into Nafion Ionomer Membranes: I . Experimental Results,* Journal of The Electrochemical Society **140**, 1373 (1993).

[26] K. A. Mauritz and R. B. Moore, *State of Understanding of Nafion,* Chemical Reviews **104**, 4535 (2004).

[27] *Nafion™ Membrane Comparison Table,* (2014).

[28] W. Y. Hsu and T. D. Gierke, *Ion transport and clustering in nafion perfluorinated membranes,* Journal of Membrane Science **13**, 307 (1983).

[29] R. Kim, S. Yuk, J.-H. Lee, C. Choi, S. Kim, J. Heo, and H.-T. Kim, *Scaling the water cluster size of Nafion membranes for a high performance Zn/Br redox flow battery,* Journal of Membrane Science **564**, 852 (2018).

[30] P. Millet, F. Andolfatto, and R. Durand, *Preparation of solid polymer electrolyte composites: investigation of the precipitation process,* Journal of Applied Electrochemistry **25**, 233 (1995).

[31] M. Shahinpoor and K. J. Kim, *The effect of surface-electrode resistance on the performance of ionic polymer-metal composite (IPMC) artificial muscles,* Smart Materials and Structures **9**, 543 (2000).

[32] W. MohdIsa, A. Hunt, and S. H. HosseinNia, *Active Sensing Methods of Ionic Polymer Metal Composite (IPMC): Comparative Study in Frequency Domain,* in *2019 2nd IEEE International Conference on Soft Robotics (RoboSoft)* (2019) pp. 546–551.

[33] I. K. Khmelnitskiy, V. V. Gorodilov, V. E. Kalyonov, A. V. Lagosh, and A. P. Broyko, *Investigation of electromechanical parameters of IPMC-sensors,* in *2018 IEEE Conference of Russian Young Researchers in Electrical and Electronic Engineering (EIConRus)*, pp. 411–414.

[34] J. Burgués, J. M. Jiménez-Soto, and S. Marco, *Estimation of the limit of detection in semiconductor gas sensors through linearized calibration models,* Analytica Chimica Acta **1013**, 13.

[35] H. Tang, Y. Li, R. Sokolovskij, L. Sacco, H. Zheng, H. Ye, H. Yu, X. Fan, H. Tian, T.-L. Ren, and G. Zhang, *Ultra-high sensitive NO2 gas sensor based on tunable polarity transport in CVD-WS2/IGZO p-n heterojunction,* ACS Applied Materials & Interfaces **11**, 40850.

[36] D. K. Biswal, D. Bandopadhya, and S. K. Dwivedy, *Evaluation of Electromechanical, Damping and Dynamic Mechanical Properties of Silver Electrode IPMC Actuator,* in *Advanced Nanomaterials and Nanotechnology*, Springer Proceedings in Physics, edited by P. K. Giri, D. K. Goswami, and A. Perumal (Springer, Berlin, Heidelberg, 2013) pp. 321–331.

5

An IPMC-based muscular thin film platform

La science est devenue un moyen de la technique.

Jacques Ellul

Parts of this chapter have been published in Micromachines 2022, 13(1), 49.

In this chapter, one application of the thin IPMC developed in the previous chapter is presented. Similarly to the work presented in Chapter 2, tissue is embedded on top of the thin cantilever-shape IPMC, soft lithography approach, as well as hydrogel-based techniques, are explored in order to grow matured and aligned tissue on top of the smart material.

5.1. Introduction

Developing integrated sensors always has been a central axis of research for organ-on-chip, as controllable quantitative sensing would allow gathering information about tissue state metabolism, drug response, and disease mechanisms *in situ*. This urgent requirement of integrated sensors is still an unmet need for organs-on-chip [1, 2]. Among different types of sensing, strain sensing has been an important tool to assess the muscular response of cardiac tissue, skeletal muscle cells or vascular smooth muscle cells [3]. The strain developed by the cultured tissue on the substrate with integrated sensor can be used to asses the phenotype of the tissue as well as its current state [4]. In the heart, several sheets of aligned muscle cells are wrapped to form the heart tissue. Each muscle layer is actually four cells thick on average, each layer is supported by cells such as fibroblasts [5, 6]. The skeletal myocytes fuse into one long muscle fiber, and the arrangement of several of these fibers ultimately forms a muscle. Both cell types (skeletal muscle cells and cardiomyocytes) possess sarcomeres, contractile components made of structured proteins arranged in a parallel way that form, in the end, a long tissue able to provide a mechanical force (myofibrils) [7]. Vascular smooth muscle cells (VSMCs) constitute the major supporting cells in arteries and are critical to maintaining the function of the vascular system, by restricting the duct or adapting to the arterial pressure. They play a central role in arterial wall remodeling and are involved in many cardiovascular diseases [8].

5.1.1. Muscular thin film platform

From previously reported work [9], it is clear that developing biologically relevant tissue on top of sensing substrate is a crucial need. The difficulty comes from two aspects, deeply linked together: developing a mature tissue strong enough to displace the sensing substrate is very important, but also it is crucial to develop a sensor sensitive enough to record the contracting tissue. One of the most relevant models of muscular tissue is the Muscular Thin Film (MTF). It consists of growing anisotropically muscle cells on a flexible, thin, cantilever-shaped substrate. The contraction of the cells, adhering to the cantilever, will induce a displacement of the cantilever, where contraction can be recorded through optical measurement or in situ through a strain sensor. Another name for the MTF is also biohybrid thin film [10–12]. Among different contributions, the work of Parker's group at Harvard is standing as a reference in the field. They first developed in 2012 a simple version of the MTF in which the recording of tissue contraction was made through optical measurement [10]. Later in 2017 they expanded this work and reported an MTF

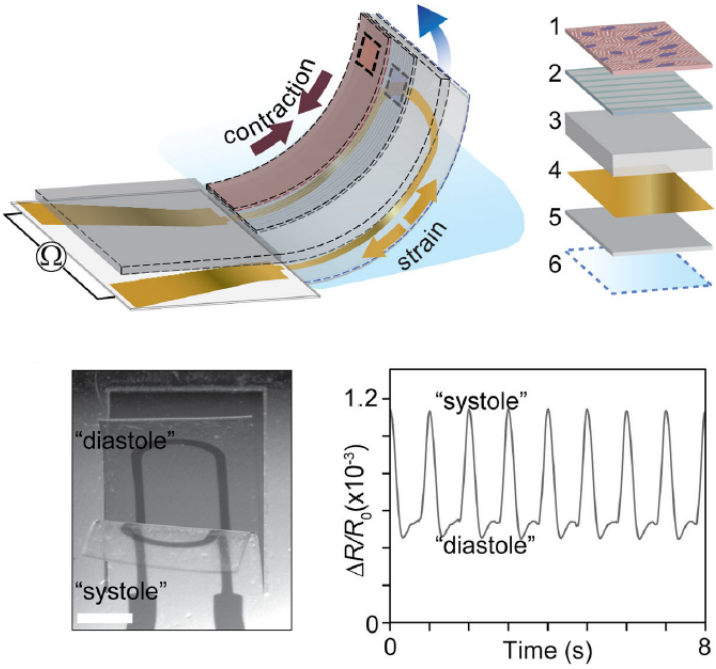

Figure 5.1: Top: the MTF platform for Parker's group is composed of several layers 1: Engineered cardiac muscle tissue 2: tissue-aligning micro-molded or micro-patterned layer 3: PDMS layer, 4: Ti-Au thin-film sensor layer, 5: bottom PDMS layer 6: PNIPAAM release layer. Bottom: example of readout of systole and diastole during the contraction of cardiomyocytes. Extracted from [9].

platform made of engineered heart tissue on top of a PDMS-based cantilever including a Ti-Au strain sensor as an in situ readout system (Figure 5.1). Interestingly, Lind *et al.* developed the device into a well-plate format for ease of use and scalability [9]. Parker's group further developed the concept of strain gauges inserted in the MTF and actually developed another version using 3D printed materials to ease the manufacturing and increase even more scalability. They succeeded to perform 3D printing of soft biocompatible materials together with conductive ink for integrated sensors. The device was printed in a standalone procedure where conductive ink was used to print the strain gauges. These techniques might show some potential to develop complex tissue as reviewed by Xiang *et al.* [13]. Additionally, as reported in older publications, the device integrates a patterned structure to induce alignment of the tissue on the main axis of the cantilever in order to induce anisotropic contraction [14]. Previous work already outlined the potential of using electroactive polymer for sensing, Araromi *et al.* developed a dielectric elastomer actuator (DEA)-based sensor for smooth muscle cell contraction sensing. However as mentioned in Chapter 2 DEA is known to require high voltage, which can harm cell culture. Saberi *et al.* already tried to use IPMC as a sensor in order to record the

intrinsic contraction of human cells, however, they could not record actual contraction because of the use of a too-thick IPMC as well as poor tissue engineering on top of the IPMC [16]. The authors explored the coating of IPMC with Rhodamine labeled Fibronectin (FN) in order to promote adhesion of cells later, they also studied the impact of FN coating on the IPMC substrate. In this Chapter, the development of hydrogel-based substrate embedding cells is explored as well as its integration on a thin IPMC cantilever.

5.2. Platform

The schematic of the entire platform is depicted in Figure 5.2. The incubator is meant to work as a Faraday cage protecting the electronics from possible environmental electric noise. Upon contraction of the tissue, the induced displacement of the IPMC will be recorded through the sensing electronic board controlled through an Arduino microcontroller. The system is powered off-grid using a 9V battery to avoid parasitic noise, data are saved in real-time using an SD card memory.

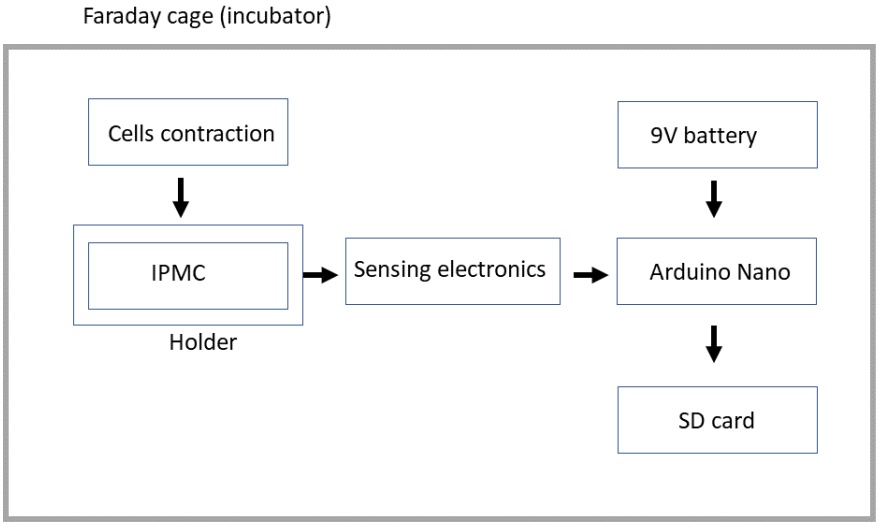

Figure 5.2: Schematic of the proposed MTF sensing platform. The platform is located in an incubator that works as a Faraday cage, upon contraction of the cells the IPMC will be displaced. The IPMC is kept in culture medium and connected to the sensing electronics through a holder. The signal is saved on an SD card.

5.2.1. Holder

Several tests to develop a proper holder in order to clamp the IPMC in between gold electrodes have been conducted. As previously described in Chapter 2, the holder was made of a 3D printed system with screws. To avoid screws, which were not user-friendly, different prototypes have been manufactured to evaporate gold directly on the 3D printed clamps using an SEM gold evaporator (Quorum 150 RS).

However, this system was not ideal, giving fragile electrodes that deliminated with time, especially while using IPMC. Then a second version was made using milled COC (cycleic olefin copolymer) under the brand name TOPAS®as the holder for optical transparency and gold (100nm) with a 10nm chromium adhesion layer, both deposited using a clean room compatible evaporator (CHA systems) and laser cut steel shadow mask (Figure 5.3). However, when tested for actuation and sensing the electrodes showed delamination, suggesting that a very low current was enough to destroy the electrodes.

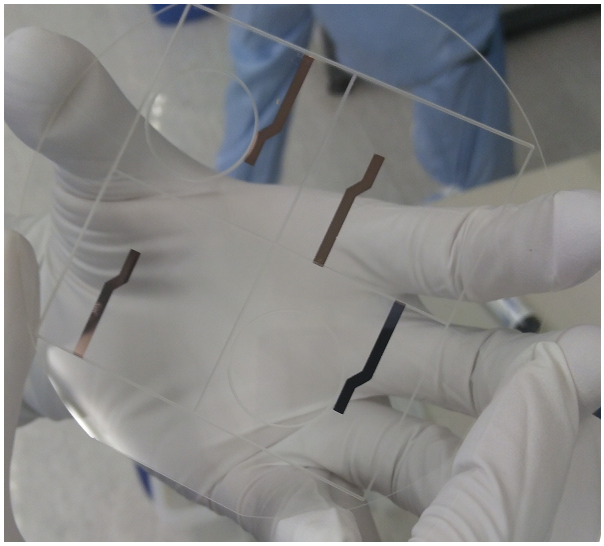

Figure 5.3: 100nm-thick gold electrodes evaporated on the TOPAS wafer. The wafer is 4-inch wide.

Therefore a second holder using standard electrodes has been finally used, the holder consists of a square reservoir where the IPMC is clamped between two gold electrodes thanks to a commercially available microscope spring (Thorlabs). The electrodes were manufactured as follows: pure gold was thinned down thanks to a roller, and later the thin gold was cut using a laser (Optec WS Starter) at the desired dimensions in order to be connected to simple wires. The entire platform is shown below in Figure 5.4, it consists of the holder embedding the MTF-IPMC and the electronics.

5.2.2. Electronics for sensing

Active sensing considers the IPMC as the source of energy. Upon displacement, the IPMC will deliver a charge imbalance measurable as a voltage [17]. The potential difference needs to be further amplified and filtered in order to precisely record the displacement. Unlike in Chapter 2 where the material used was the thick IPMC, showing a large voltage drop, the thin IPMC developed in Chapter 4 needs more precise electronics in order to filter and amplify the delicate output signal. During the development of the electronics, we faced several issues. The Arduino Nano can

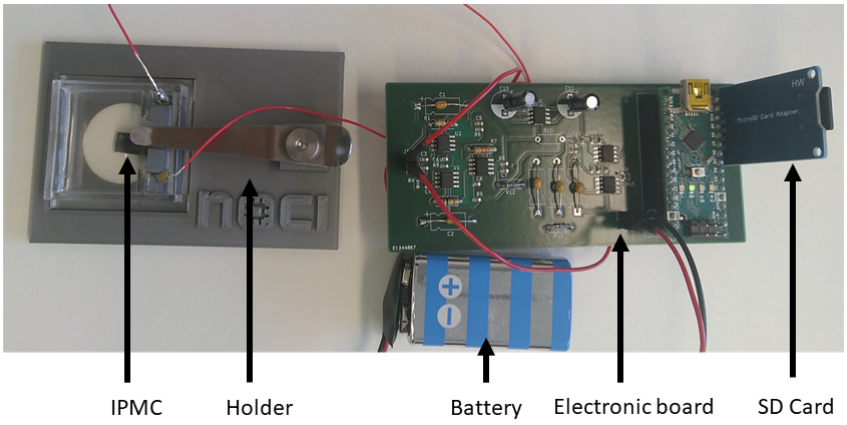

Figure 5.4: MTF Platform including the holder with the IPMC (left) and the electronics for sensing (right).

only deliver and read positive voltage ranging from 0 to 5V while the output of the IPMC is filtered and amplified in the -2.5 to 2.5 V. To overcome this issue we first thought to divide the voltage and invert it in order to read the negative voltage. However, this concept had to be rejected due to the division occurring, leading to a loss of precision. Instead, a voltage inverter based on the charge pump principle was used. The ICL7660 inverter was used to convert a positive DC voltage to its inverted form. The inverter works on the principle of charge accumulation on a polarised capacitor and then obtaining the inverted voltage from it, with respect to the ground as shown in Figure 5.5.

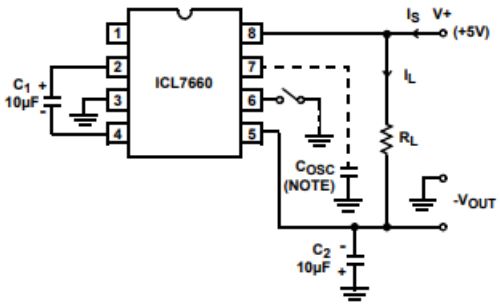

Figure 5.5: Voltage inverter principle (ICL 7660). Upon application of a charge on the capacitor the voltage will be inverted.

To be able to shift the voltage range in a range readable by the Arduino nano, as the output range will saturate after the voltage inverter, we first thought of a standard simple resistive divider. Initially, a diode-based output with voltage inversion was thought of, however, it was rejected due to the complexity involved.

Instead, a more elegant method involving a voltage shifter was used, as shown below.

By using a non-inverting summing amplifier (Figure 5.6), we were able to shift the output DC level to a positive value. The output voltage is given by:

$$V_{out} = (1 + \frac{R_a}{R_b})(\frac{V_1 + V_2}{2}) \tag{5.1}$$

According to our needs (halving the voltage), we kept R_1 and R_2 equal to each other and short R_a (resistance null) while opening R_b(infinite resistance) with R_1, R_2, R_a and R_b defined in Figure 5.6. We also connected V2 to +5V. By doing so, the output voltage can be written as:

$$V_{out} = \frac{V_1 + 5}{2} \tag{5.2}$$

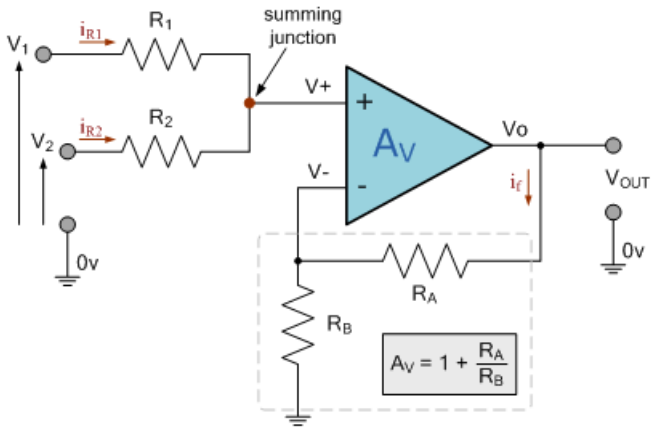

Figure 5.6: Level Shifter. Output voltage can be shifted to higher value and divided.

Since the inverter can output large currents, much above the total current drawn by the amplifiers, the inverted voltage stayed stable and did not drop. Also since the resistive divider is not used, we did not need a 9 V battery and can instead use the Arduino output itself to generate the stable +5 V which is to be inverted by the inverter. Therefore the electronics was changed in order to only use the 9 V battery to power the Arduino, while the Arduino delivers the stable voltage for the entire electronic board.

Since our output voltages can range from -5 V to 5 V, by using this level shifter, we created a final level-shifted output ranging from 0 to 5 V without any loss of information apart from a scaling down of the output swing by half. The output of the voltage level shifter was then sent to a voltage buffer stage in the form of a unity gain op-amp in order to avoid voltage drop coming from the Arduino board that could worsen the sensed signal. This ensured impedance mismatches were

avoided and the op-amp was able to provide enough input current for the Arduino. The entire circuitry can be seen in Appendix 7.6.

Preliminary tests were performed in order to check that the electronic board was working for simple displacement of the IPMC. A setup based on a microfluidic droplet generator was used, water droplets were falling on a beaker containing the thin IPMC. The delicate displacement of the liquid in the beaker would deform the thin IPMC. This technique presents the benefit of keeping the thin IPMC in a wet environment. The initial tests were positive showing a recording of displacement (Figure 5.7). However, because no laser triangulation system was used it was not possible to assess the position of the beam during the induced displacement.

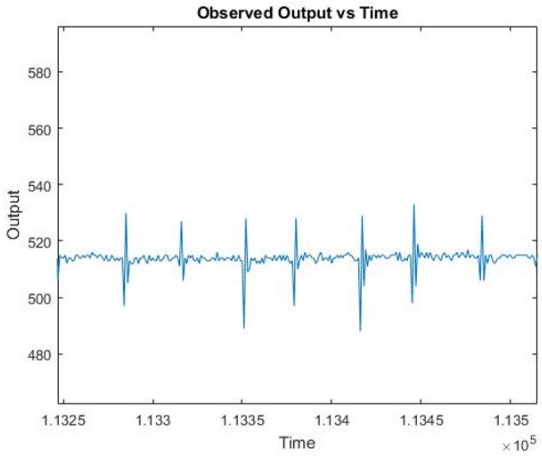

Figure 5.7: Read out of the test made on the electronics board using a water droplet generator. The sensing mechanism is active: the displacement of the IPMC will trigger a charge imbalance measurable as a voltage drop. The peak corresponds to the water droplet falling, leading to the displacement of the IPMC. The value of the baseline is around 515 mV corresponding to the charge of the IPMC when the measurement started.

5.3. Tissue engineering

5.3.1. Soft lithography and membrane release

Besides developing materials and platforms for sensing, one of the biggest challenges in MTF is to actually be able to engineer the tissue in a way that it will be mature and strong enough to induce a displacement on the cantilever-shaped substrate. Several approaches have been explored, one being a patterned substrate made of PDMS to induce anisotropic growth of the human tissue, the other one being direct hydrogel patterning.

Soft lithography

Soft lithography consists of using a substrate (usually silicon or photo patternable polymer) as a mold in order to pattern a polymer such as PDMS [18, 19]. The

mold once fabricated is most often silanized to make the surface hydrophobic and to allow peeling off the polymer (Figure 5.8). Lind *et al.* reported the manufacture of grooves in order to induce alignment of cardiomyocytes on their MTF using soft lithography. The tissue growing anisotropically was able to displace the cantilever once mature enough [9]. Lind *et al.* reported the use of 5um tall grooves with 25 um-wide ridges and 50um-wide gap. A first attempt to test how cells would react on such a substrate was performed by LUMC colleagues. The mold for soft lithography was manufactured by using a commercial digital micromirror device (DMD)-based setup using light for backside exposure of an epoxy-based negative photoresist (SU-8) on glass coverslips (Primo Alvéole, Chapter 3). The substrate was further silanized and PDMS spin-coated on it to manufacture PDMS grooves. The grooves can be seen in Figure 5.9 as well as the anisotropicity of the cells growing on top (Figure 5.10).

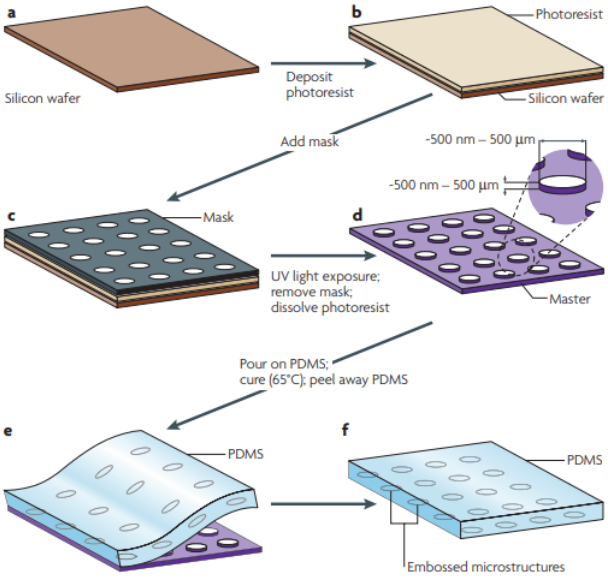

Figure 5.8: Fabrication of a PDMS layer incorporating microstructures. Drawings (a,b,c and d) correspond to the fabrication of a rigid master through standard photolithography. Drawings (e) and (f) can be considered as part of the soft lithography process where soft polymer is peeled off the fabricated mold. Extracted from [19].

Once the design parameters were confirmed by biologists from Leiden Medical center (Dhanesh Kasi) further investigation was performed in order to embed such a patterned substrate on the thin IPMC. As already explained in the previous chapters, the IPMC is very sensitive to the moisture environment, once dry it will be prone to shrinkage while once wet it will expand, this effect is emphasized with thin Nafion. The main approach which has been explored was to perform standard soft lithography and to embed the thin IPMC on the uncured PDMS. The process was similar to the one performed for thick IPMC and membrane manufacturing for

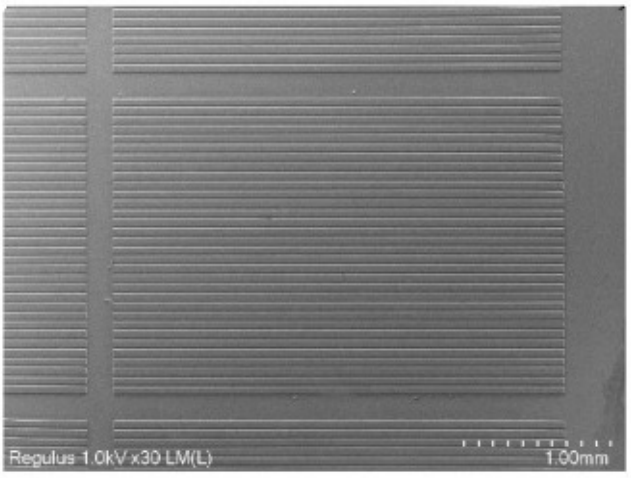

Figure 5.9: SEM pictures of the manufactured SU-8 mold for grooves manufacturing. The 25 um-wide ridges can be seen.

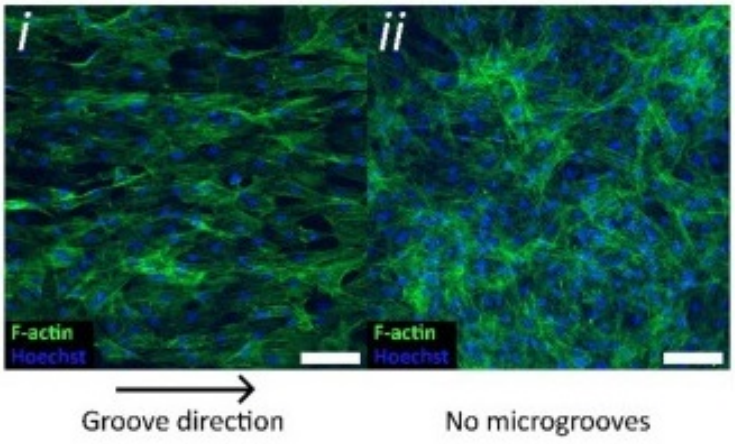

Figure 5.10: Aligned vSMC (i) versus non aligned vSMC (ii) after growing on the patterned substrate (PDMS).

the micropump (Chapter 3). Prior to embedding an IPMC on the PDMS, the Su-8 mold for soft lithography has been manufactured as follows: the SU-8 has been spin-coated on the wafer exposed and developed to obtain the grooves patterns; then the wafer has been silanized prior to spin coating the PDMS. We spin-coated the PDMS at 1000 rpm to deposit approximately 25 um of PDMS on the thin IPMC. The detailed flowchart can be found in the Appendix 7.3. The curing has been

performed in a moisture-rich environment at room temperature for 72h to avoid shrinkage of the delicate thin IPMC. The IPMC-PDMS cantilever has been carefully peeled off from the wafer. The laser reconstruction picture (Figure 5.11) shows that the PDMS stays on the IPMC, even though experimentally we noticed that the layers were prone to detach. We can already start to see the PDMS detaching on the bottom left on the reconstructed picture (Figure 5.11).

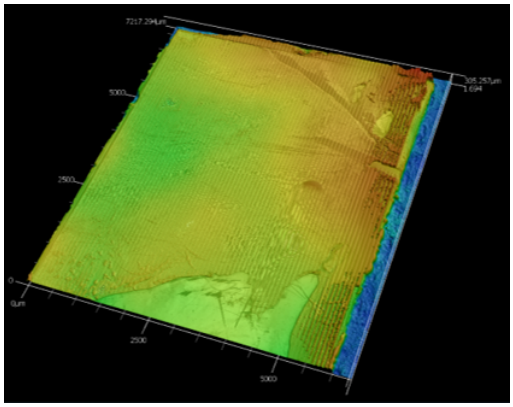

Figure 5.11: Laser reconstruction of the thin IPMC embedded with PDMS. The handling is very delicate because of the inherent thickness of the PDMS and the IPMC. the IPMC has to be kept in water to keep the sample flat. PDMS grooves start to detach (bottom right).)

The partners at the Leiden University Medical center (LUMC) successfully grew vascular smooth muscle cells on the thin IPMC substrate with PDMS grooves (Figure 5.12). Unfortunately, the thin IPMC is not transparent, therefore the final user cannot clearly check the cell culture and need to perform staining and flip the cantilever to check for the cell culture. In addition, we can notice some discontinuities in the tissue with some gaps in between cells. This tissue was ultimately too fragile and not mature enough nor strong enough to be able to displace the thin IPMC.

Membrane release

To overcome the issues of the detachment of PDMS from the thin IPMC we experimented different approaches using negative photoresist and PDMS. The idea was to pattern negative photoresist (AZ10XT) and spin-coat a thin layer of PDMS with embedded IPMC on it (Figure 5.13). Later the photoresist was etched away using dimethylsulfoxide (DMSO), a standardly used solvent, also used in biology to thaw cells.

Laser measurement showed that the photoresist layer reproduces correctly the grooves on the mask (Figure 5.14). The ridges and gap were inverted as the mold is the negative footprint of the final patterned substrate.

This approach despite being promising shows one main drawback, a small part of the PDMS is attached to the wafer as can be seen in Figure 5.13. Therefore when the DMSO is applied there is still some PDMS attached to the wafer leading to delicate detachment, ultimately the PDMS was peeling off from the IPMC. To

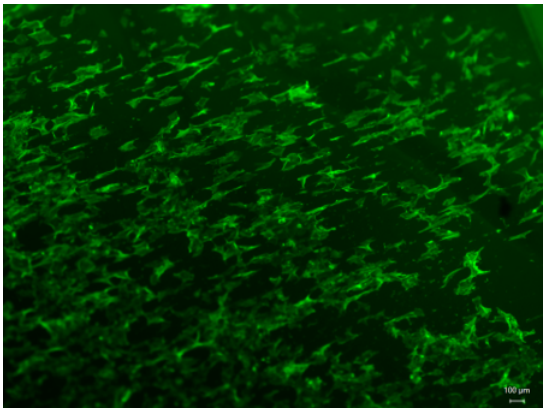

Figure 5.12: Aligned vascular smooth muscle cells on the thin IPMC. The tissue was not mature enough and continuity is lacking in between cells.

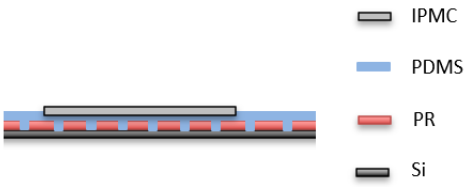

Figure 5.13: Cross-section view of the 1 layer approach for IPMC-PDMS membrane releasing.

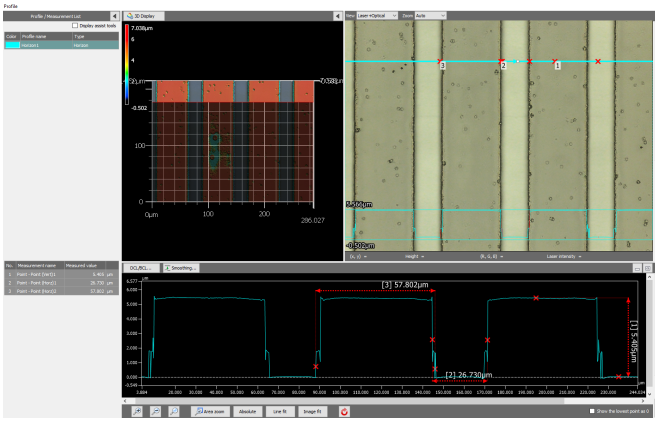

Figure 5.14: Laser measurement of the photoresist. The ridges are 57 μm wide with a 26 μm gap in between.

overcome these issues we experimented the ”2 layers approach” where the first layer of AZ10xt is deposited on the wafer prior to depositing the second layer with the grooves (Figure 5.15).

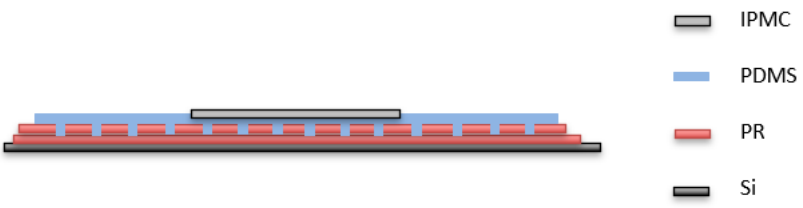

Figure 5.15: Cross-section view of the layers used for releasing the PDMS-IPMC MTF

Also, we noticed that the DMSO is a very strong solvent and if some DMSO gets in contact with the IPMC the IPMC will strongly shrink, most probably because the small molecule of DMSO will rearrange the Nafion backbone. To overcome this issue we proposed to avoid using PDMS and to focus on a different material. One very promising material being hydrogel, a protein-based polymer commonly used in tissue engineering. The hydrogel can be made of different biological-based materials, in our case we used collagen.

5.3.2. Surface chemistry for IPMC-hydrogel bonding

Partners from LUMC also experienced the manufacturing of a thin hydrogel layer meant to be prepared and manufactured before being bonded to the IPMC. The engineered sheet was manufactured as follows. A PEG-based anti-fouling layer was spin-coated on a PDMS mold with grooves as well as on a glass cover slip. The anti-adhesive layer inhibited the adhesion of the protein-based hydrogel to the treated surface. On the contrary, a spin-coated thin PDMS layer (100um) was treated with glutaraldehyde and cut with a blade in a suitable dimension, the glutaraldehyde promoted the adhesion of the hydrogel to the treated surface, and the treated PDMS worked as a spacer to control the height of the hydrogel which will be patterned. The spacer was then deposited on top of the glass coverslip. The hydrogel was then prepared and poured on the glass coverslip within the spacer, then the PDMS-treated mold was used to induce patterns on the hydrogel (microgrooves), PDMS stamp was detached from the hydrogel easily thanks to the antifouling layer. A glass coverslip was then put in the incubator in order to polymerize the hydrogel. After the curing, the hydrogel is slowly detached on the edges thanks to a blade. The advantage of this technique is that the hydrogel can be patterned before and cells seeded directly after the curing. The optical transparency also makes it possible to check for the cell culture during an extended period of time and only detach the tissue mature enough to be bonded to the IPMC. Preliminary tests have been performed to check the bonding of the hydrogel to the IPMC. The surface of the IPMC (platinum) can be treated with oxygen plasma and functionalized with glutaraldehyde. Preliminary tests showed that the bonding of hydrogel to the IPMC was excellent, however, we noticed that the hydrogel sheet is extremely fragile and is prone to destruction while handling.

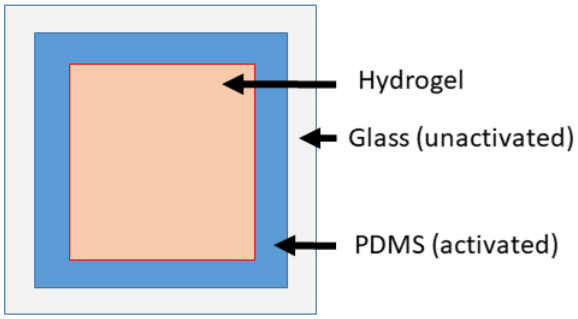

Figure 5.16: Surface chemistry for thin sheet hydrogel tissue engineering. Glass is unactivated with anti-fouling layer, to avoid hydrogel bonding while a PDMS spacer is manufactured with the edges covered with glutarladehyde: to promote hydrogel bonding. Hydrogel is inserted in the center and patterned with a second PDMS stamp having negative grooves (unactivated). The final hydrogel will have the thickness of the spacer and the patterns of the stamp, thus sheet can be engineered and embedded later on the thin IPMC.

5.4. Conclusion

In this chapter, attempts of manufacturing a platform to explore thin IPMC as a sensor for muscular thin film have been presented. We showed that the electronics is of crucial importance in order to be able to measure, filter, and amplify the low-voltage output of the thin IPMC. We also explored tissue engineering on top of the thin IPMC. Despite the ease of manufacturing soft lithography seems to be a very difficult approach as it requires very careful handling from the user. In addition, the inherent properties of the IPMC (moisture sensitive) makes the manufacturing with PDMS extremely difficult, as the PDMS is more stable to solvent and shows lower Young's modulus than Nafion. Tentatives have been performed using a more adapted material such as hydrogel. Despite the inherent properties of hydrogel which makes it a perfect candidate for tissue engineering, we showed that the handling and bonding to the thin IPMC is still user dependent and a fragile procedure. Overall, the tissue needs to be mature enough and grown on an adequate substrate with sufficient bonding and flexibility. Ultimately the MTF model might not be the most adapted to sensing with thin IPMC. In the future, one could consider using engineered heart tissue (EHT)in a device with mciropillars that could give a better anchor point and could be easier to integrate into the IPMC than MTF, delicate to culture and fabricate.

In the next chapter, another application of the thin IPMC developed in Chapter 4 is presented. The smart material with relevant properties for OoC is used as the core material of a microfluidic flow sensor.

References

[1] A. Bass, L. Kinter, and P. Williams, *Origins, practices and future of safety pharmacology,* Journal of Pharmacological and Toxicological Methods First Annual Focus on Safety Pharmacology, **49**, 145 (2004).

[2] M. Mastrangeli, S. Millet, t. O. Partners, and J. v. d. E.-v. Raaij, *Organ-on-Chip In Development:Towards a roadmap for Organs-on-Chip,* (2019), 10.20944/preprints201903.0031.v1.

[3] G. A. Clarke, B. X. Hartse, A. E. Niaraki Asli, M. Taghavimehr, N. Hashemi, M. Abbasi Shirsavar, R. Montazami, N. Alimoradi, V. Nasirian, L. J. Ouedraogo, and N. N. Hashemi, *Advancement of Sensor Integrated Organ-on-Chip Devices,* Sensors **21**, 1367 (2021), number: 4 Publisher: Multidisciplinary Digital Publishing Institute.

[4] O. T. Guenat and F. Berthiaume, *Incorporating mechanical strain in organs-on-a-chip: Lung and skin,* Biomicrofluidics **12**, 042207 (2018).

[5] M. J. Kocica, A. F. Corno, F. Carreras-Costa, M. Ballester-Rodes, M. C. Moghbel, C. N. C. Cueva, V. Lackovic, V. I. Kanjuh, and F. Torrent-Guasp, *The helical ventricular myocardial band: global, three-dimensional, functional architecture of the ventricular myocardium,* European Journal of Cardio-Thoracic Surgery: Official Journal of the European Association for Cardio-Thoracic Surgery **29 Suppl 1**, S21 (2006).

[6] R. J. Laird and S. Irwin, *Chapter 1 - Cardiovascular Structure and Function,* in *Cardiopulmonary Physical Therapy (Fourth Edition)*, edited by S. Irwin and J. S. Tecklin (Mosby, Saint Louis, 2004) pp. 3–38.

[7] C. Franzini-Armstrong and A. G. Engel, *Chapter 53 - Skeletal Muscle: Architecture of Membrane Systems,* in *Muscle*, edited by J. A. Hill and E. N. Olson (Academic Press, Boston/Waltham, 2012) pp. 763–774.

[8] D. Hu, C. Yin, S. Luo, A. J. R. Habenicht, and S. K. Mohanta, *Vascular Smooth Muscle Cells Contribute to Atherosclerosis Immunity,* Frontiers in Immunology **10** (2019).

[9] J. U. Lind, M. Yadid, I. Perkins, B. B. O'Connor, F. Eweje, C. O. Chantre, M. A. Hemphill, H. Yuan, P. H. Campbell, J. J. Vlassak, and K. K. Parker, *Cardiac Microphysiological Devices with Flexible Thin-Film Sensors for Higher-Throughput Drug Screening,* Lab on a chip **17**, 3692 (2017).

[10] A. Grosberg, A. P. Nesmith, J. A. Goss, M. D. Brigham, M. L. McCain, and K. K. Parker, *Muscle on a chip: In vitro contractility assays for smooth and striated muscle,* Journal of Pharmacological and Toxicological Methods **65**, 126 (2012).

[11] L. Vannozzi, T. Mazzocchi, A. Hasebe, S. Takeoka, T. Fujie, and L. Ricotti, *A Coupled FEM-SPH Modeling Technique to Investigate the Contractility*

of Biohybrid Thin Films, Advanced Biosystems **4**, 1900306 (2020), _eprint: https://onlinelibrary.wiley.com/doi/pdf/10.1002/adbi.201900306.

[12] Y. Sun, R. Duffy, A. Lee, and A. W. Feinberg, *Optimizing the structure and contractility of engineered skeletal muscle thin films,* Acta Biomaterialia **9**, 7885 (2013).

[13] Y. Xiang, K. Miller, J. Guan, W. Kiratitanaporn, M. Tang, and S. Chen, *3D bioprinting of complex tissues in vitro: state-of-the-art and future perspectives,* Archives of Toxicology **96**, 691 (2022).

[14] J. U. Lind, T. A. Busbee, A. D. Valentine, F. S. Pasqualini, H. Yuan, M. Yadid, S.-J. Park, A. Kotikian, A. P. Nesmith, P. H. Campbell, J. J. Vlassak, J. A. Lewis, and K. K. Parker, *Instrumented cardiac microphysiological devices via multimaterial 3D printing,* Nature materials **16**, 303 (2017).

[15] O. Araromi, A. Poulin, S. Rosset, M. Favre, M. Giazzon, C. Martin-Olmos, M. Liley, and H. Shea, *Thin-film dielectric elastomer sensors to measure the contraction force of smooth muscle cells,* in *Electroactive Polymer Actuators and Devices (EAPAD) 2015*, Vol. 9430 (International Society for Optics and Photonics, 2015) p. 94300Z.

[16] A. Saberi, S. Ashworth, and M. Shahinpoor, *Ionic Polymer Metal Composites (IPMCs) Substrates as Real Time Sensing Systems to Study Biological Cells Adhesion, Traction and Migration,* (American Society of Mechanical Engineers Digital Collection, 2016).

[17] W. MohdIsa, A. Hunt, and S. H. HosseinNia, *Active Sensing Methods of Ionic Polymer Metal Composite (IPMC): Comparative Study in Frequency Domain,* in *2019 2nd IEEE International Conference on Soft Robotics (RoboSoft)* (2019) pp. 546–551.

[18] Y. Xia and G. M. Whitesides, *Soft Lithography,* Annual Review of Materials Science **28**, 153 (1998), _eprint: https://doi.org/10.1146/annurev.matsci.28.1.153.

[19] D. B. Weibel, W. R. DiLuzio, and G. M. Whitesides, *Microfabrication meets microbiology,* Nature Reviews Microbiology **5**, 209 (2007), number: 3 Publisher: Nature Publishing Group.

6

An IPMC-based microfluidic flow sensor

One day I will find the right words, and they will be simple

Jack Kerouac

Parts of this chapter have been presented at the IEEE Sensors conference, 31st Oct-4 Nov 2022 Dallas, USA.

In this chapter, another application of the thin IPMC developed in Chapter 4 is presented. The smart material with relevant properties for OoC is used as the core material of a microfluidic flow sensor.

6.1. Introduction

As outlined in Chapter 3, since the very beginning of OoC technology, microfluidics has been a cornerstone to control precisely the microenvironment and mechanical cues [1, 2]. Monitoring flow inside microfluidic devices is a crucial need to control the gradients of nutrients, O_2 distribution, and shear stress within an OoC. Precise flow assessment can also help to control the distribution of molecules of interest such as drugs, endocrine and exocrine metabolites. Among the different types of sensors urgently needed in OoC, flow sensors have been reported as one of the most important [3]. We can categorize the flow sensors that can be used for microfluidics applications into different types depending on the sensing mechanisms [4]. One can distinguish active flow measurement, where energy is sent to the sensing system in order to perform the measurement (Figure 6.1), from the passive flow measurement systems, where the probe is fully passive and only records flow displacement, with no energy transfer from the probe toward the liquid (Figure 6.2).

6.1.1. Active flow measurement methods

In the active flow measurement type, we can mention the sensors based on Coriolis force, where a vibration is induced to a microfluidic channel and perpendicular vibration induced by Coriolis effect (inertial force due to the moving liquid) is recorded. The amplitude of the oscillation can be used to measured the flow rate [5, 6]. Similar to Coriolis effect, one can also think of acoustic flow measurement, where acoustic waves are sent and recorded in the channel, and the shift of frequency recorded can be correlated to the flow rate [7]. The second other type of active flow sensing is based on heat transfer, this type is by far the most commonly sensor in microfluidics application [4]. Thermal sensors rely on the difference in temperature between a heating element and a temperature probe induced by the flow of fluid, which provides a measure of flow rate. We can distinguish 3 sub-types. The hot-wire and hot-film anemometry (HFA) measure the heat transfer from a hot body to the flowing fluid. For the calorimetric sensor, two thermal sensors are placed around the heater, therefore it is possible to measure bidirectional flow. Both aforementioned techniques are the most commonly used, though unfortunately, their sensitivity is limited. To solve this issue, time-of-flight (TOF) sensors can be used where heat impulses are induced and recorded downstream to measure the flowrate. Theses systems are however more complex as heat impulses require dedicated design and electronics, and more expensive than the previous ones [8].

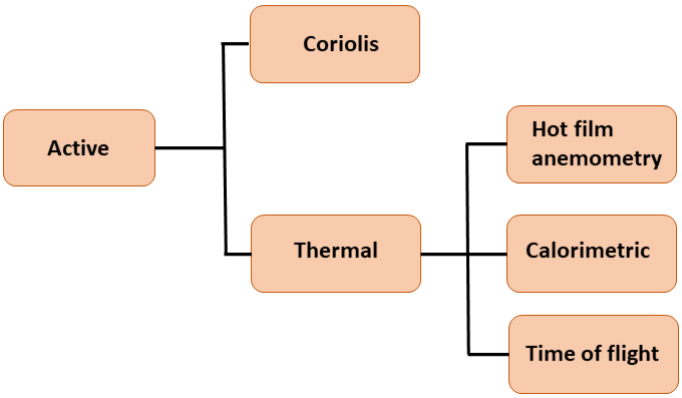

Figure 6.1: Active flow sensing techniques, adapted from [4]. The active flow measurements methods can be distinguished in two parts, either Coriolis or thermal, the first one relies on Coriolis effect to estimate the speed of the liquid while the second one relies on heat transfer and temperature measurement to have an estimation of the fluid's speed.

6.1.2. Passive flow measurement methods

The second category of flow sensors includes passive ones. Passive flow sensors, unlike active ones, don't rely on energy transfer from the sensing device to the liquid to perform the measurement. The first passive flow sensor is the gravimetric one, it simply relies on a miniaturized scale that records the mass of the fluid passing through the microfluidic circuit for a certain amount of time. As the mass of the liquid is known, the flow speed can be calculated [9]. The second type of passive flow sensing method is the fluid-structure interaction. Within this type there are 3 other subtypes: the cantilever, the pressure difference and the particle seeding [4]. The first one is simply a cantilever embedded in the microfluidc channel, the bending of the cantilever can easily be recorded through optical tracking or integrated piezoresistive sensor. The curvature of the cantilever is proportional to the force applied to the cantilever and ultimately to the flow rate [10, 11]. The second is the pressure difference measurement and relies on Hagen-Poisseuille law, by measuring the pressure difference between the inlet and outlet of a microchannel of known dimensions, it is possible to obtain the flow rate measurement. The last passive flow measurement method is the particle seeding. Briefly, particles are seeded within the channel, the displacement of the particles is measured through optical tracking (PIV) or laser Doppler velocimetry (LDV). For PIV, the speed of the liquid is estimated through the calculated particle speed recorded on the videos and extracted through image processing. For the LDV, an interference fringe system is used, When the particles pass, it creates scattered light. The scattered light signal shows amplitude modulation with a Doppler frequency, correlated to the speed of the particles.

Among the different types mentioned earlier, some flow sensors can actually

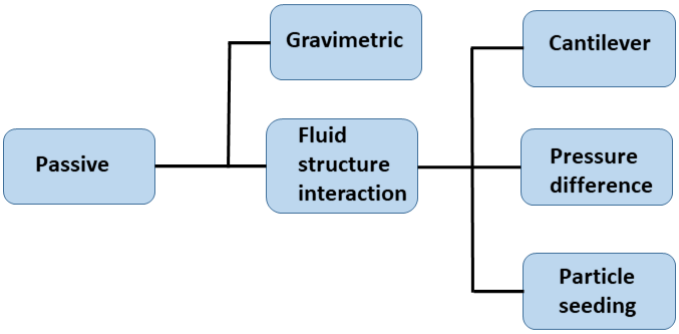

Figure 6.2: Passive flow sensing techniques, adapted from [4]. Passive methods for flow sensing can be separated in two parts: gravimetric, where measurement of a mass of liquid can be used to estimate the speed, and fluid-structure interaction, where the liquid interacts with either a cantilever, particles or a channel of known dimensions to estimate the speed of the liquid.

be manufactured using wafer-scale microfabrication, providing the possibility to scale production and meet the need of scalable sensors for OoC. Ejeian *et al.* [12] reviewed the different materials and techniques used to measure flowrate within microfabricated devices. Out of the different approaches that exist, MEMS thermal sensors, piezoresistive sensors and MEMS piezoelectric flow sensors are commonly used in MEMS industry. Interestingly, when looking at MEMS flow sensor devices one can see that for water-based measurement the most commonly manufactured one is piezoresistive, most probably for ease of manufacturing and ease of measurement (Figure 6.3). The active and passive sensors are summed up in Table 6.1, including the range of detection, relative uncertainty response time, and estimated price. The sensors present very different ranges and response times depending on their mode of sensing (Table 6.1).

The different techniques mentioned present however some limitations in the context of OoC implementation. For instance, heat transfer-based systems might deteriorate the biological molecules of interest and disturb cell phenotype if used above 37°in addition to not being able to record backflow easily (unless using TOF thermal sensor) which is essential for vasculature modeling in OoC [13]. In addition, acoustic flow measurement and Coriolis flow measurement are complex, costly, bulky, and might be hampered by the presence of circulating cells in an OoC such as blood cells or immune cells. The optical approach is not integrated in the microfluidic device, while the piezo material characteristics get altered over time by temperature and liquid exposure, in addition to showing potential cytotoxicity [12]. Finally, the particle seeding approaches can hardly be integrated within a functional OoC with real-time tracking. The tracking of particles can however be used for the characterization of microfluidic devices prior to their actual use (Chapter 3).

Table 6.1: Main features of liquid flow sensors for microfluidics. Adapted from [4].

Flowmeter	Range ($\mu l.min^{-1}$)	Relative uncertainty (%)	Response time (s)	Estimated price (euros)
Calorimetric	0.07-1.5	10	0.04	100-1000
HFA	3-176	5	0.01	100-1000
TOF	10-1000	6	0.012	100-1000
Coriolis	0.84-3300	0.2	0.2	2000-4000
Cantilever	2-35	0.1	NA	1000-5000
Pressure difference	1.1-1100	10	0.1	250-1000
Particle seeding	0.001-54	2-5	1	10000
Gravimetric	0.1-1000	0.6-01	2	10000

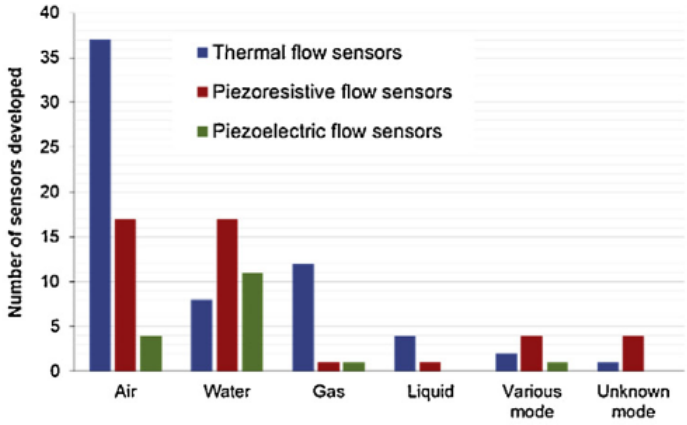

Figure 6.3: Types of liquids and sensing used with MEMS flow sensing technology. Extracted from [12].

6.1.3. IPMC Sensing principles

One can distinguish passive sensing from active sensing when dealing with IPMC [14]. When performing passive sensing with IPMC, we consider the IPMC as an inert component such as a resistance, when the IPMC is displaced by fluid flow, the resistance of the IPMC might change, the resistivity shift is then correlated to the displacement (no energy is delivered by the IPMC). On the other hand, active sensing with IPMC considers the material as an energy source: upon displacement induced by external forces, the IPMC develops charge unbalance measurable as a voltage drop (Figure 6.4).

6.2. Flowrate sensing plateform

IPMC presents inherent attractive properties, making this material promising for microfluidic applications and life sciences (Chapter 2, Chapter 3, Chapter 5). IPMC

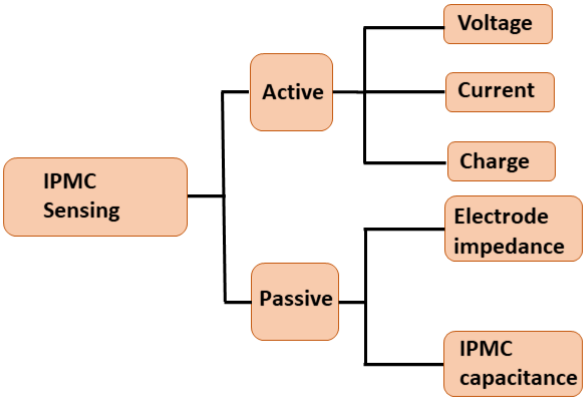

Figure 6.4: Classification of IPMC sensing principles. Active sensing uses the voltage, current or charge imbalance due to the displacement of the IPMC, the IPMC is seen as an active device delivering energy. In passive sensing, capacitance or resistance changes of the IPMC due to the displacement are measured, the IPMC is therefore seen as a passive element.

is water compatible and doped with cations (Na+) naturally present in most of the cell media used for OoC. Because of the inherent properties of IPMC we believed that an IPMC-based flow sensor could outperform the existing solutions for flow measurement in an OoC. Interesingly, researchers already used IPMC for sensing flow [15, 16]. However Zhong *et al.* and Yang *et al.* used standard IPMC, 180 μm-thick for macro-scale application (underwater robots), not flexible enough for microscale applications such as microfluidic flow sensing. In this chapter, we will depict the conception and characterization of a microfluidic flow sensor based on a cantilever-shaped thin IPMC. The material used is the one developed in Chapter 4, that exhibits lower flexural rigidity than standard IPMC (46 times). The IPMC material is water-permeable and absorbs cations, which can freely move in the polymer backbone. The induced displacement due to incoming flow at a certain speed will trigger IPMC deformation. The mechanical deformation of the IPMC will induce a displacement of the cations, leading to a voltage drop across the electrodes that can be used as a readout signal (Figure 6.5). In this chapter we have explored 2 different types of sensing, passive sensing where the IPMC is considered as a resistance and active sensing where the energy delivered by the IPMC cantilever is directly measured.

The proposed platform hosting the IPMC-based sensor is represented in Figure 6.6. The platform is composed of the microfluidic structure, in which the IPMC cantilever, working as flow sensor, is embedded, and an electronic board connected to a PC.

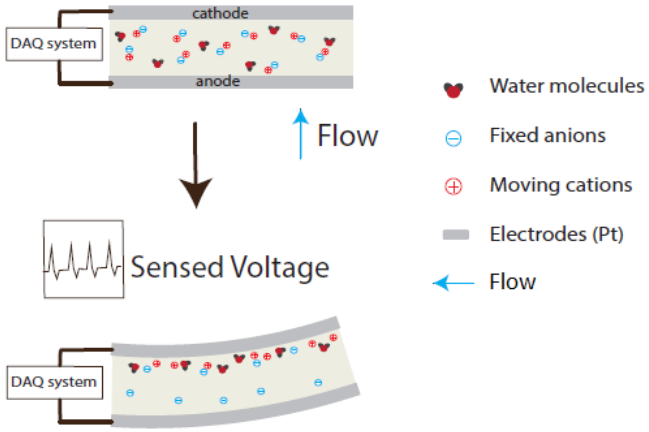

Figure 6.5: IPMC sensing principle. The displacement of the ionic electroactive material (top) triggers cations migration, causing a charge imbalance, measurable as a voltage difference output across the electrodes (bottom) through the data acquisition system (DAQ).

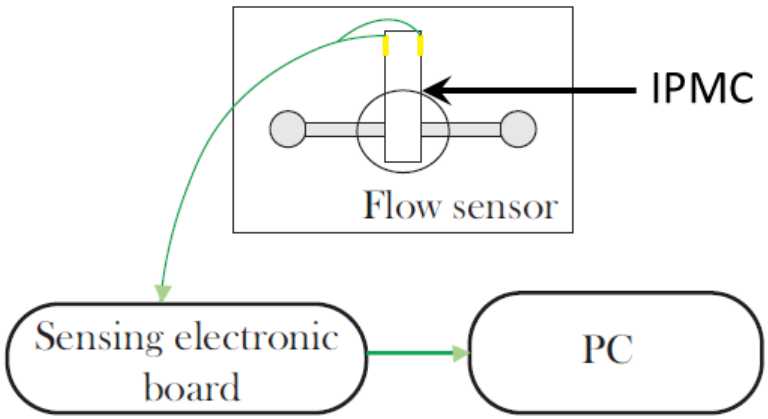

Figure 6.6: Schematic of the sensing platform. IPMC is connected to the electronic board through gold electrodes. A computer can be connected to the electronic board for real-time presentation or data can be saved on an SD card for off-grid measurement.

6.2.1. IPMC-based flow sensor

The microfluidic structure hosting the flow sensor has been designed using computer-aided design software (SolidWorks). The structure is made of two parts printed through high-resolution stereolithography (Asiga MAX X27 UV, Moiin Tech clear

resin) (Figure 6.7). The microfluidic circuit is 0.5 mm-high and 1 mm-wide. In the center of the structure a 4 mm-wide chamber hosts the IPMC cantilever. The 50 μm-thick IPMC cantilever has been laser-cut (Optec) with the dimensions of 2.5 mm x 7.5 mm and clamped in between two laser-cut gold electrodes. The bottom and top part of the flow sensor have been bonded using laser-cut pressure sensitive adhesive (PSA, 81 μm-thick, Adhesive research). The IPMC has been manufactured as previously described in Chapter 4.

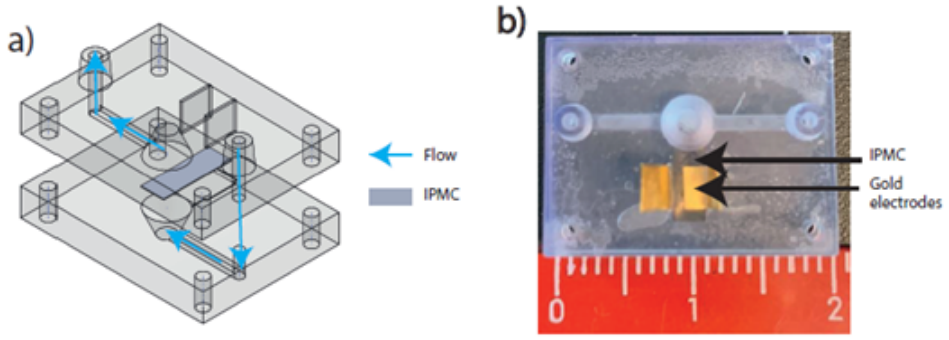

Figure 6.7: IPMC-based flow sensor. a) CAD view of the flow sensor, with the IPMC cantilever embedded in the center, and direction of the flow. b) Close view of the flow sensor, gold electrodes can be seen.

6.2.2. Passive sensing

The considered approach for passive sensing made use of a Wheatstone bridge. Such a bridge consists of a measured sensor of resistance Rx, two resistors R1 and R3 and a potentiometer R2, arranged as in Figure 6.8. In this setup, the two arms of the bridge act like voltage divider circuits. When the arms are balanced, the difference in voltage between points B and D is zero. Thus, balance is achieved by tuning the value of the potentiometer to match the resistance of the device under test (DUT). For R1 = R3 and the condition of balance, Vg = 0V attained, we can read the value of the potentiometer as the value of the sensor resistance. Thus, any change in Vg after balancing the bridge can be attributed to a change in the resistance of our IPMC. By attaching points D and B to the terminals of a differential amplifier and balancing the bridge, we can accurately measure our sensor response. Full schematic can be found in the Appendix 7.6.

In practice, the IPMC sensor does not exhibit pure resistive behavior due to the generation of charges and internal capacitance. To perform passive resistive sensing with IPMC, a voltage needs to be applied at the IPMC's electrodes and the changing resistivity of the IPMC can be further correlated to the displacement induced by the flow. Measurements were recorded with the Arduino Nano board

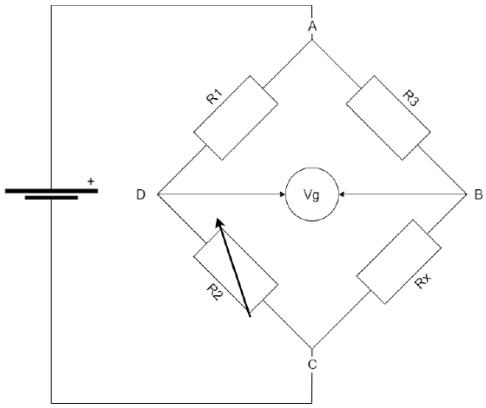

Figure 6.8: Schematic of the Wheatstone bridge. The unknown resistance Rx is to be measured; resistances R1 and R3 are known, where R2 is adjustable. When the measured voltage V_g is 0, both arms have equal voltage ratios.

and saved on an SD card in real-time (Figure 6.9). The protocol to estimate the sensitivity of the flow sensor is the following: pipetting is performed with a fixed volume at 1Hz, and as the volume and time are known the volumetric flowrate is also known, therefore the voltage drop due to the deformation of the IPMC can be correlated to the flowrate. The capacity of the pipette was set to 60µL, and phosphate buffered saline solution (PBS) was administered by manual pipetting, at approximately 1s intervals, in short bursts. The bridge was balanced with 100kΩ resistances while the trimmer was used to adjust the resistance of the Wheatstone bridge in order to maximize the output signal. The amplifier gain was set to 100. The induced flow was calculated to be approximately 80.13 µL/s, obtained by taking into account the internal channel capacity and the duration of a pulse. A sensing signal of 50Hz with an amplitude of 50mVpp was applied as input voltage. The adjustable trimmer was rotated until the bridge was balanced, after which flow was administered and the signal recorded. Measurements were further processed with Python 3.6.

The induced liquid pipetting could be successfully recorded with the passive sensing based on Wheatstone bridge (Figure 6.10). This proof of concept however was not optimal and we noticed that it was extremely difficult to match the value of the IPMC resistance with the trimmer. In addition the IPMC resistance value was prone to change over time leading to delicate measurement, it was possible to measure the pipetting only for a short period of time before the IPMC resistance was changing too much and the recorded signal was saturating. We hypothesize that the value of resistance of the IPMC was changing significantly over a short period of time because of current and ions concentration in electrode proximity affecting electrode effective resistance. Therefore the active sensing method was implemented on the exact same platform, in order to verify that measurement could be performed for a longer period of time. As explained in the next section,

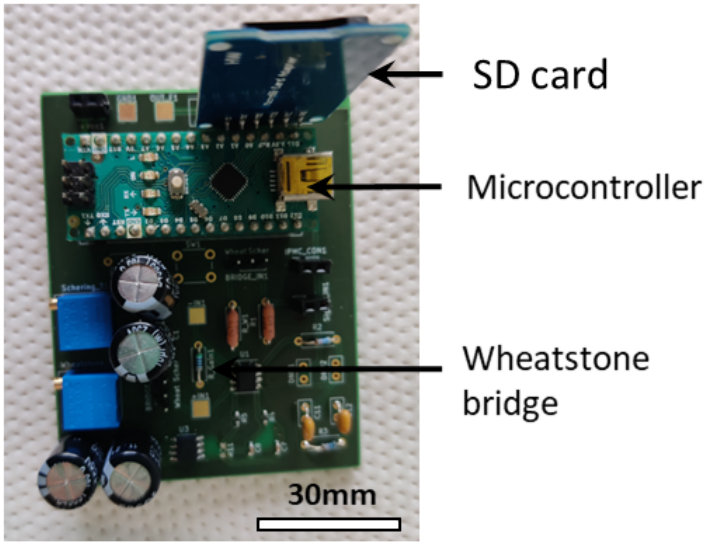

Figure 6.9: Wheatstone bridge implemented on a PCB used for passive sensing. Data can be saved in real-time using SD card.

we noticed improved stability and sensitivity calculation has been performed on the active flow sensing platform.

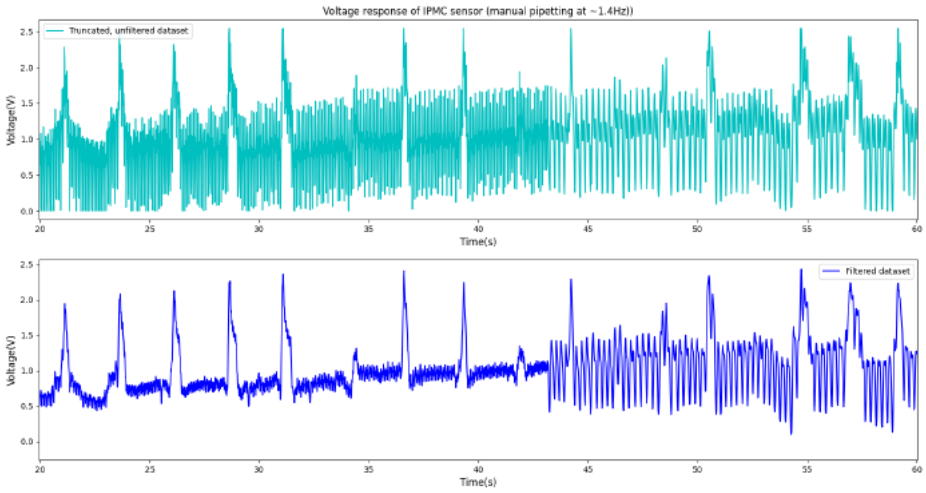

Figure 6.10: Result of passive sensing of 1 Hz pipetting. The peaks of detection are due to the pipetting. The dataset has been filtered using Python 3.6.

6.2.3. Active sensing

We have developed an electronic board for sensing the charge produced on the IPMC electrodes [14] (Figure 6.11). The electronics have been described in more detail in Chapter 5. Briefly, IPMC electrodes are connected to the board input. The first stage of the board is made of a charge amplifier circuit with gain G=100. The signal is sent to an instrument amplifier (G=1), then a second-order passive low-pass filter with a cut-off frequency of 1125 Hz is used to filter out high-frequency noise. Data are saved in real-time on a memory card. The schematic can be found in Appendix 7.6.

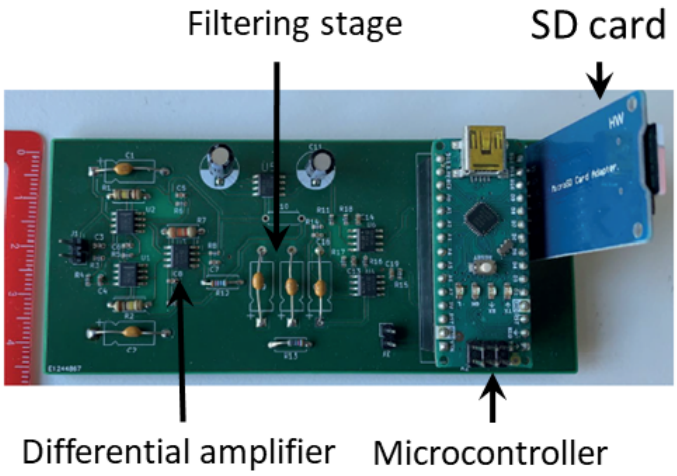

Figure 6.11: Close view of the active charge-based electronic board. The active sensing electronics circuit is made of a differential amplifier (G=1), a filtering stage, a microcontroller, and an SD card for real-time data saving.

6.3. Flowrate characterization

To characterize the active IPMC-based flow sensor (charge sensing), phosphate buffered saline solution (PBS) has been used. PBS was injected using a micropipette (Gilson), and pipette tips have been connected to the input and output of the flow sensor. Manual pipetting with a cadence of 1 s has been performed with volumes increasing from 10 μL to 40 μL. The recorded data have been processed using Python 3.6. The signal has been filtered using Savitzky–Golay filter method to filter out potential noise (Figure 6.12 a) [17]. For each pipetted volume, 12 flow peaks have been detected and used to calculate the voltage amplitude corresponding to the volume used (Figure 6.12 a). The mean and standard deviation of the volumetric flow rate have been calculated using the pipetted volume divided by the time recorded between each peak. The voltage measured against the volumetric flow rate was used to obtain the responsivity curve (Figure 6.12 b).

Flowrate measurement data for 3 different volumes show a good fit ($R^2 = 0.998$) with a first-order polynomial in the linear range ($4.78\ x + 116.92$). The offset is most probably due to charges already present on the IPMC when the measurement was starting. The sensitivity extracted from the slope of the first-order polymer is 4.78 mV/(μL/s). We noticed output signal saturation starting at a high flowrate (Figure 6.12).

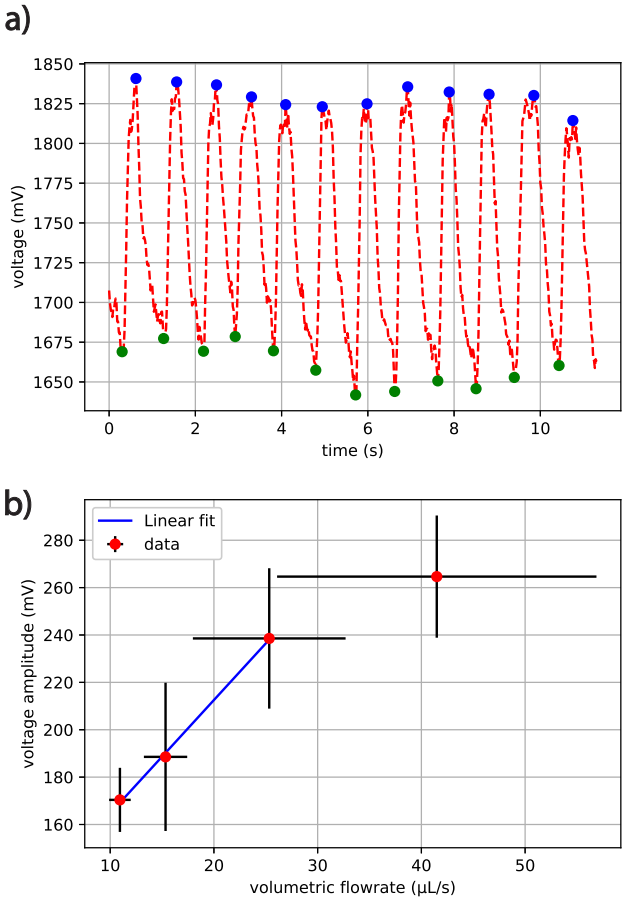

Figure 6.12: Flowrate detection and responsivity of the IPMC-based microfluidic flowsensor. a) Peaks detected for 10μl pipetting. Blue, top of the peak used to calculate the voltage amplitude. Green, points used to estimate time for each peak. b) Responsivity plot. Linear fit used to calculate the sensitivity (blue), R^2 = 0.998. The offset is most probably due to charges already present on the IPMC when the measurement was starting. Sensitivity is 4.78 mV/(μL/s).

Values can be compared to the flow measured with standard IPMC or cantilever-based design. Mohammadamini *et al.*, who used an optical cantilever-based flow sensor, were able to obtain a sensitivity of 0.126 µm/(μL/min) in the range of measured flow rates (0-100 μL/min) [10]. Lei *et al.* who used a thick IPMC sensor

(254μm thick) could detect flow velocity in the cm/s range in the vicinity of their IPMC sensor for flow detection in an open environment [18]. Comparing the performances of our thin active IPMC flow sensor is challenging as the design, units, and dimensions are different from one author to the others. However, our sensor could detect as small as 10ul passing by the channel every second. This result suggests that the superior flexibility of the thin IPMC makes the final flow-sensor a very good candidate for small-volume detection. In addition, we can compare the sensing performance to the work of Zhang *et al.* who achieved sense flow in 0–0.23 m/s range with a cantilever-based piezo sensor [11]. Unlike IPMC, the performance of piezoresistive material can be influenced by temperature and humidity over time. Thus, aging of the materials used for piezo-sensitive flow sensors has adverse effects on sensor performance, limiting its use in wet, warm environments such as in OoC.

6.4. Conclusion

We have presented a novel, simple, inexpensive, and easy-to-use flow sensor device that could be used for OoC applications. The inherent properties of the thin ionic electroactive polymer make the device a good candidate to monitor flow in sensitive microenvironments such as lab-on-chip LOC and OoC devices, sensitive to heat and high voltage. This sensor could compete with already existing systems such as other cantilever-based sensors and thermal sensors and was able to detect flow rates as small as 10μL/s. The proposed thin ionic polymer-based flow sensor allows to the measurement of pulsatile flowrate in a range from 10 to 40μL/s with a sensitivity of 4.78 mV/(μL/s). We hypothesize that the saturation of our sensor comes from the relative dimension of the ionic-electroactive cantilever and the chamber where it is inserted. A bigger chamber and longer cantilever could achieve detection in a wider range of flowrates. In addition, a longer microfluidic circuit would allow using of higher liquid volumes. Performing further experiments under a wider flow range, and calibration with precise thermal flow sensors to further quantify the sensor sensitivity are suggested for future work. One might also consider characterizing the sensor with fluids of different viscosity (e.g., blood). Future improvements and characterization should aim at increasing the range of detection and calibrating the measurement for further comparison. The proposed device could be tailored to many other uses such as Point-of-care (POT) and micro total analysis system (uTAS) applications as well as lab-on-chip devices using pulsatile flow patterns.

References

[1] M. L. Coluccio, G. Perozziello, N. Malara, E. Parrotta, P. Zhang, F. Gentile, T. Limongi, P. M. Raj, G. Cuda, P. Candeloro, and E. Di Fabrizio, *Microfluidic platforms for cell cultures and investigations,* Microelectronic Engineering **208**, 14 (2019).

[2] C. L. Thompson, S. Fu, H. K. Heywood, M. M. Knight, and S. D. Thorpe,

Mechanical Stimulation: A Crucial Element of Organ-on-Chip Models, Frontiers in Bioengineering and Biotechnology **8**, 1426 (2020).

[3] F. Kurth, E. Györvary, S. Heub, D. Ledroit, S. Paoletti, K. Renggli, V. Revol, M. Verhulsel, G. Weder, and F. Loizeau, *Chapter 3 - Organs-on-a-chip engineering,* in *Organ-on-a-chip*, edited by J. Hoeng, D. Bovard, and M. C. Peitsch (Academic Press, 2020) pp. 47–130.

[4] C. Cavaniol, W. Cesar, S. Descroix, and J.-L. Viovy, *Flowmetering for microfluidics,* Lab on a Chip **22**, 3603 (2022), publisher: The Royal Society of Chemistry.

[5] R. Monge, J. Groenesteijn, D. Alveringh, R. J. Wiegerink, J. Lötters, and L. J. Fernandez, *SU–8 micro coriolis mass flow sensor,* Sensors and Actuators B: Chemical **241**, 744 (2017).

[6] J. Haneveld, T. Lammerink, M. de Boer, and R. Wiegerink, *Micro Coriolis Mass Flow Sensor with Integrated Capacitive Readout,* in *2009 IEEE 22nd International Conference on Micro Electro Mechanical Systems* (2009) pp. 463–466, iSSN: 1084-6999.

[7] A. F. Quelennec, J. J. Gorman, and D. Reyes-Hernandez, *FREQUENCY TUNABLE LABEL-FREE SURFACE ACOUSTIC WAVE-BASED FLOW SENSOR,* NIST (2020), last Modified: 2021-10-14T05:10-04:00 Publisher: Aurore F. Quelennec, Jason J. Gorman, Darwin Reyes-Hernandez.

[8] L. Huang, *Micromachined Thermal Time-of-Flight Flow Sensors and Their Applications,* Micromachines **13**, 1729 (2022), number: 10 Publisher: Multidisciplinary Digital Publishing Institute.

[9] H. Bissig, H. T. Petter, P. Lucas, E. Batista, E. Filipe, N. Almeida, L. F. Ribeiro, J. Gala, R. Martins, B. Savanier, F. Ogheard, A. K. Niemann, J. Lötters, and W. Sparreboom, *Primary standards for measuring flow rates from 100 nl/min to 1 ml/min – gravimetric principle,* Biomedical Engineering / Biomedizinische Technik **60**, 301 (2015), publisher: De Gruyter.

[10] F. Mohammadamini, J. Rahbar Shahrouzi, and M. Samadi, *A suspended polymeric microfluidic sensor for liquid flow rate measurement in microchannels,* Scientific Reports **12**, 2642 (2022), number: 1 Publisher: Nature Publishing Group.

[11] Q. Zhang, W. Ruan, H. Wang, Y. Zhou, Z. Wang, and L. Liu, *A self-bended piezoresistive microcantilever flow sensor for low flow rate measurement,* (2010), 10.1016/J.SNA.2010.02.002.

[12] F. Ejeian, S. Azadi, A. Razmjou, Y. Orooji, A. Kottapalli, M. Ebrahimi Warkiani, and M. Asadnia, *Design and applications of MEMS flow sensors: A review,* Sensors and Actuators A: Physical **295**, 483 (2019).

[13] K. Kaarj and J.-Y. Yoon, *Methods of Delivering Mechanical Stimuli to Organ-on-a-Chip,* Micromachines **10**, 700 (2019).

[14] W. MohdIsa, A. Hunt, and S. H. HosseinNia, *Active Sensing Methods of Ionic Polymer Metal Composite (IPMC): Comparative Study in Frequency Domain,* in *2019 2nd IEEE International Conference on Soft Robotics (RoboSoft)* (2019) pp. 546–551.

[15] J. Zhong, D. L. S. Hung, G. Zhu, and X. Tan, *Cycle-to-cycle response of ionic polymer-metal composite materials subject to pulsing flow-induced stimulus,* in *2012 IEEE/ASME International Conference on Advanced Intelligent Mechatronics (AIM)* (2012) pp. 432–437, iSSN: 2159-6255.

[16] Q. Yang, Q. Hu, Y. Liu, Y. Li, S. Li, and Z. Zhu, *Enhanced water flow sensing performance based on multi-ciliated structure of ionic polymer–metal composite,* AIP Advances **11**, 105320 (2021), publisher: American Institute of Physics.

[17] S. R. Krishnan and C. S. Seelamantula, *On the Selection of Optimum Savitzky-Golay Filters,* IEEE Transactions on Signal Processing **61**, 380 (2013), conference Name: IEEE Transactions on Signal Processing.

[18] H. Lei, M. A. Sharif, D. A. Paley, M. J. McHenry, and X. Tan, *Performance improvement of IPMC flow sensors with a biologically-inspired cupula structure,* in *Electroactive Polymer Actuators and Devices (EAPAD) 2016*, Vol. 9798 (SPIE, 2016) pp. 418–426.

7

Conclusion and recommendations

The best thing about graduating from university was that I finally had time to sit on a log and read a good book.

Edward Abbey

7.1. Conclusions

In this thesis the use of an electroactive material, namely ionic polymer metal composite (IPMC) has been explored in the context of organ-on-chip applications. The work outlined a few contributions, summarized below.

Contribution 1: implementation of IPMC in wafer-level processing

Integration of IPMC within a wafer-level process flow has been investigated in order to explore the potential of integrating smart materials for the mass production of OoC. IPMC was successfully integrated into a silicon-based micropump using state-of-the-art microfabrication techniques. The use of encapsulation within polymer-based resin in a moisture-controlled environment in order to stabilize the material is a good approach to embedding the material. This technique of encapsulation, together with standard soft lithography, has been proven to lead to the fabrication of robust PDMS-IPMC-based membranes. However, the handling of IPMC is very dependent on the tendency of the material to absorb water and different type of solvents, therefore the integration of such material requires carefully designing the process flow in order to avoid the use of a solvent or to integrate the material at the last step of the process flow.

Contribution 2: characterization of thin IPMC manufacturing for sensors application

The fabrication of a thin IPMC for sensing in the context of OoC has been investigated. The fabrication of a thin IPMC has been successfully conducted and the dynamics of the electroless deposition recipe has been proven to be different for thin PFSA membranes compared to thick ones. A recipe based on the dilution factor has been used (suggested in the literature). A comparative study has been performed between thick IPMC and thin IPMC. The resulting thin IPMC delivered superior sensing capability because of the inherent lower thickness leading to lower flexural rigidity. The diluted recipe leads to thinner electrodes with higher conductivity. This thin material however shows an increased sensitivity to moisture, making the integration of polymers and different materials on top of the thin IPMC more difficult than for the thicker IPMC. An electronic circuit has been specifically developed to filter and amplify the signal coming from the delicate thin IPMC.

Contribution 3: Development of an IPMC-based microfluidic pump for organ-on-chip applications

The manufacturing of an IPMC-based micropump for OoC applications has been explored. A micropump embedding a membrane made of IPMC together with PDMS and non-moving part valves has been manufactured. The pump also endows a 3D hydrogel-based channel to better reproduce a biological microenvironment such as a micro-vessel. The pump achieved relevant shear stress values for organ-on-chip. This proof-of-concept device integrates for the first time an electroactive polymer-based membrane together with a relevant 3D microenvironment for tissue engineering. This device may pave the way to electronically controllable smart materials-based OoC integrating 3D relevant microstructure.

Contribution 4: Lumped model of IPMC-PDMS-based micropump

For the first time, a lumped model based on an analogy between the electric domain and the fluidic domain has been proposed for an electroactive polymer-based micropump for OoC applications. This work offers the possibility to understand the frequency response of the developed micropump including the inherent flexibility due to the mechanical properties of the electronically controllable membrane.

Contribution 5: Development of an IPMC-based microfluidic flow sensor for organ-on-chip applications

A flow sensor has been manufactured based on the developed thin IPMC and its sensing capabilities proven. A sensitivity of 4.78 mV/(μL/s) has been achieved for pulsatile flow rates. Passive as well as active sensing have been investigated, and active flow sensing has been chosen because of the improved stability in comparison to the passive sensing approach. The sensor shows good potential for monitoring flow in the context of organ-on-chip applications because of the inherent properties of the thin IPMC.

7.2. Recommendations for future work

Manufacturing thin IPMC for organ-on-chip applications

In this thesis, a recipe for platinum electroless deposition has been characterized for thinner IPMC in organ-on-chip applications. In the future, further optimization of the recipe by using different dilution factors could be considered as well as targeting different thicknesses. We believe that the optimal IPMC, showing good actuation capabilities with enough thickness and thin enough for sensing applications, could be detrmined and manufactured by using an electroless deposition recipe with the appropriate concentration depending on the targeted application. Also, in the context of industrialization, the electroless deposition recipe should be better controlled and understood especially to enhance reproducibility during manufacturing.

Integrating IPMC in wafer-level processing

Integrating IPMC in a wafer-level process flow has been found to be difficult because of the inherent properties of IPMC. However, the integration was made possible by encapsulation in resins and careful design of the flow process. In the future, reversible chemical treatment of IPMC to limit its ability to swell upon solvent absorption could be a good axis of research in order to better stabilize the material and process it further at wafer-level with solvent-based steps.

IPMC-based micropump for organ-on-chip applications

A prototype of a micropump has been manufactured using an IPMC-PDMS-based membrane and NMP valve by using stereolithography. In the future, further investigation of NMP valve micropump could be considered by using different techniques for manufacturing the chip itself. One could think of injection molding, hot embossing, or even UV-sensitive polymer foil, already known in the lab-on-chip community as lab-on-foil devices. One could consider the integration of electroactive smart material together with the microfluidic foil while stacking the layers to make a functional device. Also, the flowrate achieved by the micropump has been found to be relevant for specific applications such as endocrines releasing organs, but too small for models that require high shear stress. Thus, we could imagine creating IPMC-based micropumping solutions to electronically control the gradient of oxygen within gut-on-chip models or endocrine release within the organoids model. In the future, one could consider developing pumps with different designs in order to achieve higher flowrate for other applications. It could also be considered to integrate on the same board different pumping membranes with different microfluidic channels in order to create complex microfluidics for multi-organ-on-chip on the same board. Hydrogel material has been successfully integrated and patterned in the micropump, and injection of living cells has been found to be difficult and could be improved in the future. The integration of patterned hydrogel within microfluidic chips could be further explored for different applications in organ-on-chip, we could mention for instance organoids or more complex structures such as villi of a gut.

IPMC-based microfluidic flow sensor

Thin IPMC has been successfully investigated for microfluidic flow sensing applications and showed good sensing capabilities in the studied range. Both passive and active sensing have been investigated, and active sensing has been found to be more stable than passive sensing. However, in the future one could imagine using real-time resistance value adjustments for the Wheatstone bridge (for instance with the use of a microcontroller) in order to use the passive sensing. Passive sensing has been reported to be correlated to the curvature of the IPMC, which would allow measuring steady flow, while active sensing was more efficient for pulsatile flow.

Muscular thin film platform and integration of hydrogel on thin IPMC

Patterned hydrogel has been explored on top of the thin IPMC to establish a muscular thin film. Surface chemistry has been found to be the best approach to bond the material to the platinum-based surface of the IPMC. In the end, the organ-on-chip field relies heavily on material science, and the choice of the material for the manufacturing, as well as the substrate for cells to be cultured on, are crucial. In the future, the integration of different types of materials (ionic electroactive material, hydrogel, matrigel...), as well as topographical cues within the same chip, could be a way to obtain physiologically relevant 3D models with built-in electro responsive actuators or sensors. One could for instance imagine integrating ionic electroactive material in PDMS membrane within engineered heart tissue (EHT) in order to induce electronic mechanical cues to the heart tissue.

Appendix

7.3. SU-8 flowchart for soft lithography

- Surface dehydration
  - Bake the wafer at 200 °C for 5 mins in order to remove any water
  - Let the wafer cool down a few minutes
- Preparing SU8
  - Leave the SU8 at room temperature for at least 24h
  - Pour the required amount of SU8 in a cup and degas it several time
- Spin coating
  - Pour slowly on the wafer the SU8 in order to avoid bubbles formation
  - spin coat using the following process
    1. 10 rpm for 180s, distribute the SU8 all over the wafer
    2. 3500 rpm for 30 determined the final thickness (<5um)
    3. 10 rpm for 300s, manual edge bead removal
- Soft bake
  - soft bake for 2mins at 95 °C for 2mins
- Exposure
  - Load the mask in the contact aligner and use approximatively 100mw/cm2
- Post-exposure bake
  - bake at 95 °C for 3min
- Development
  - Use PGMEA to develop the SU8, rinse with IPA, and dry
- Hard bake
  - Increase the temperature from 65 °C to 150 °C with a ramp of 5°C every minute
- Silanization
  - place the wafer in the vacuum chamber with a few droplets of perifluorosilane

7.4. Flowchart for the fabrication of the silicon-based IPMC-driven micropump

The different steps of the fabrication process for manufacturing of the micropump are summarized below:

1. Silicon wafer, 400μm-thick double side polished
   - Pattern the alignment marks on the wafer (zero layer)
2. Silicon oxide hardmask
   - Deposit 12 μm of plasma enhanced chemical vapor deposition (PECVD) on the front side of the wafer
   - Spin coat, expose and develop positive resist
   - Etch the silicon oxide hard mask using RIE
3. Photoresist mask
   - Spin coat 10μm of positive photoresist AZ10XT, expose and develop
4. DRIE 1
   - Perform frist DRIE for 150 μm (pumping chamber etch)
5. Remove Photoresist using oxygen plasma
6. DRIE 2
   - Perform second DRIE for 150 μm (microfluidic channel etch), leave 100μm for the silicon membrane
7. Remove the PECVD oxide using BHF
8. Deposit thermal oxide (10μm)
9. Deposit photoresist at the bottom of the microfluidics using spray coating
10. Perform RIE (anisotropic) on the front side of the wafer to thin down the thermal oxide
11. Perform RIE (anisotropic) on the backside of the wafer to thin down the thermal oxide
12. Perform silicon oxide wet etching to remove the remaining thermal silicon oxide on the front side and backside (silicon oxide should remain on the sidewalls of the microfluidics circuitry)
13. Perform anodic bonding with glass wafer to close the microfluidics circuitry
14. Spin coat PDMS and embed the IPMC in between positive resist and the PDMS membrane

15. poke the inlet and outlet of the microfluidics circuitry and perform XeF2 etch to etch away the remaining silicon below the PDMS membrane
16. remove the photoresist using acetone and ultrasonic bath

7.5. Electronics for actuation and sensing

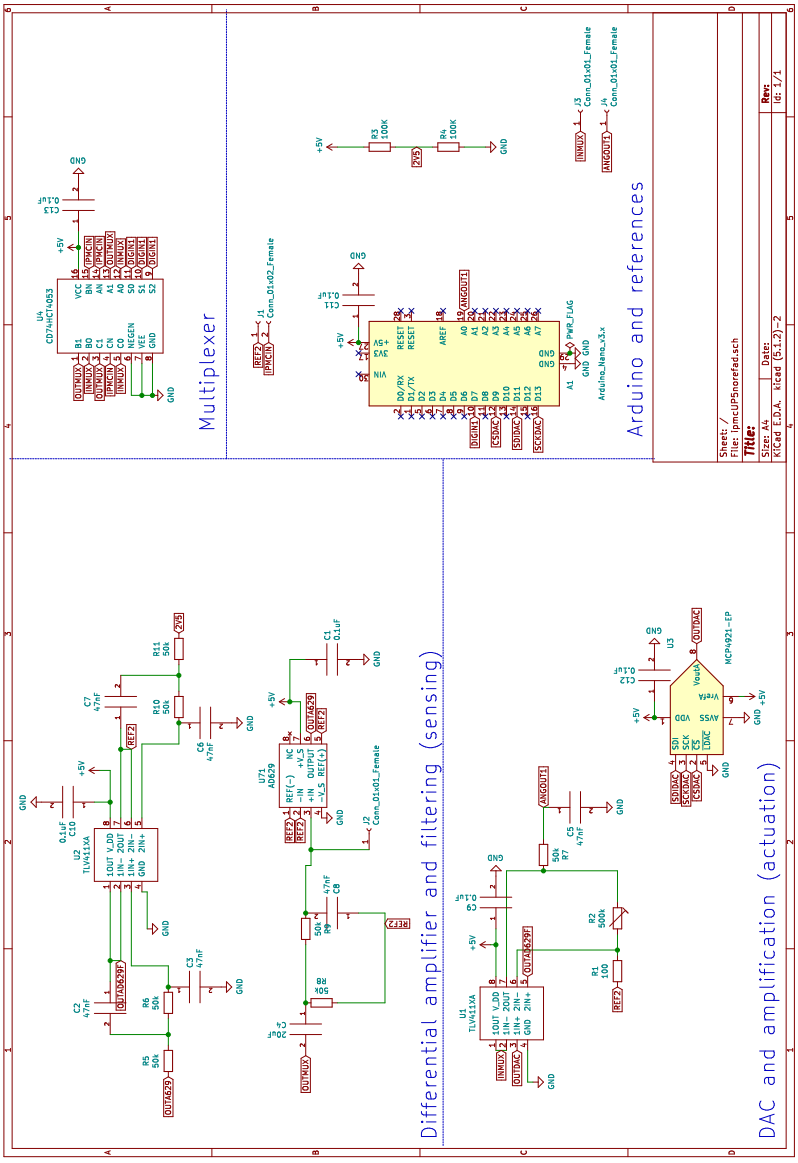

Figure 7.1: Schematic of the circuit used for actuation and sensing with standard IPMC.

7.6. Electronics for sensing

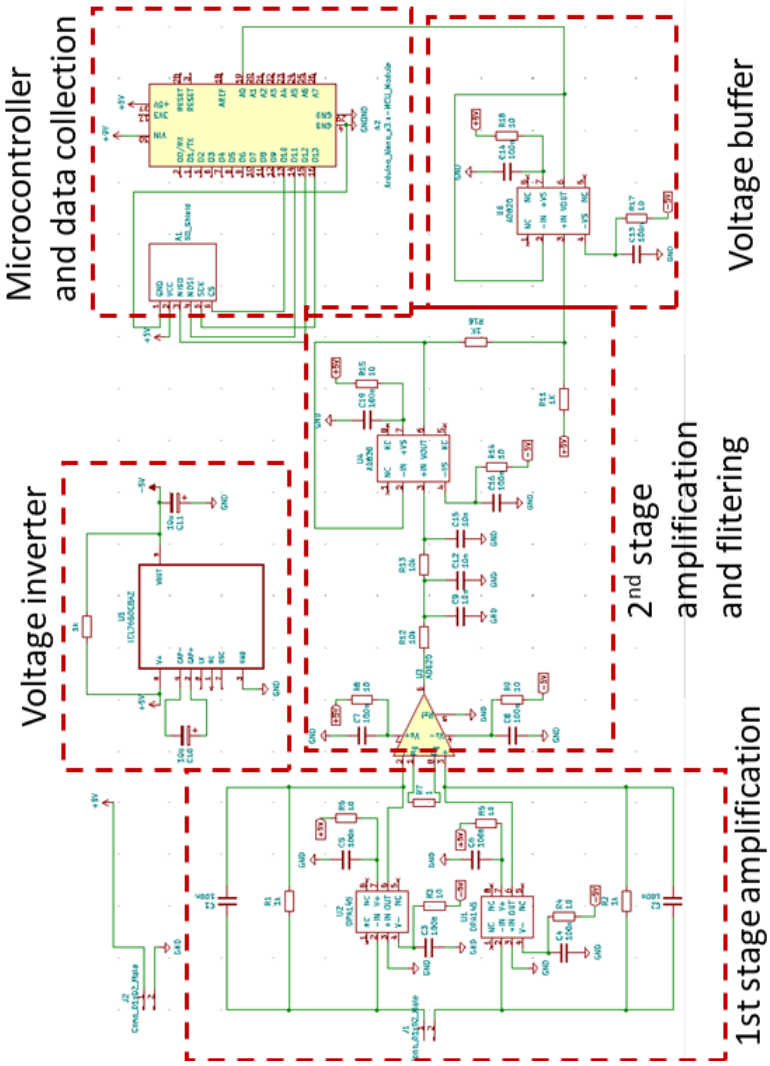

Figure 7.2: Schematic of the final circuit used for active sensing with thin IPMC.

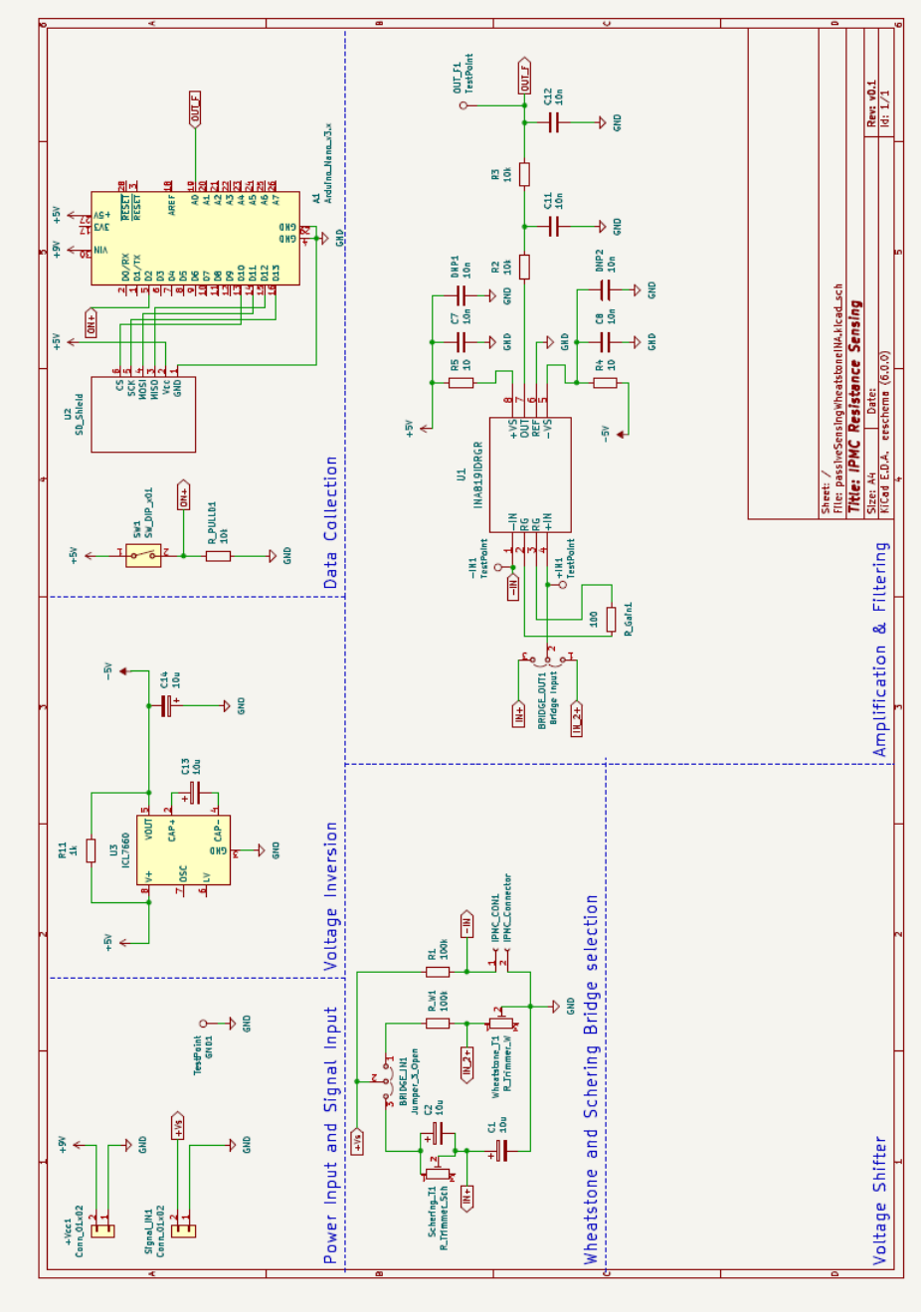

Figure 7.3: Schematic of the final Wheatstone bridge circuit used for passive sensing with thin IPMC.

7.7. Peak Flowrate

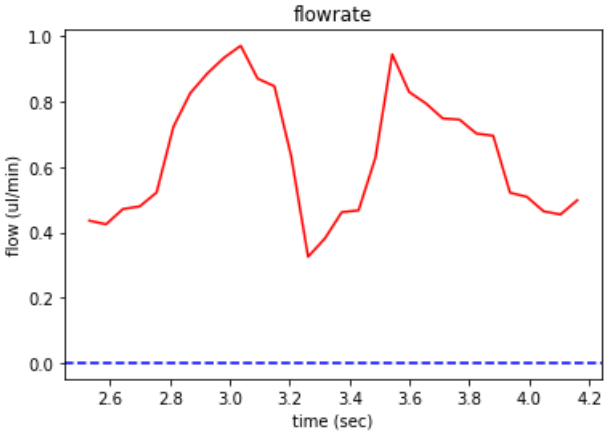

Figure 7.4: Close-up view of the peak flowrate achieved with a 3Vpp at 1hz actuation scheme, the peak flowrate has been used to estimate the maximum shear stress.

Acknowledgements

First of all, I would like to thank my supervisor and my promotor, Dr. Massimo Mastrangeli and Prof. Dr. Pasqualina Sarro, thank you for the opportunity that you offered to me. I was able to work in a very fruitful and diverse environment, thank you for your support throughout the past years as well as for the liberty that you gave to me in exploring different approaches and materials.

I would like to thank all the committee members: Prof. Gidrol, Dr. Boukany, Prof. Odijk, Dr. Hunt, Prof. French, and Prof. Dekker, for accepting to be part of the promotion committee and for taking the time to read my thesis.

It was a very special experience exploiting the Else Koi facilities and learning how to work in the cleanroom. I would like to thank the people who help me in this environment through guidance and advice in order to cope with this challenging environment. Mario, Johannes, Silvana, Joost, Robert, Hitham, Koos, Tom, Jord, Gregory, Sten, Paolo, Bruno, Violeta, Aleksandar, Lovro, Juan, Sten, Henk, Shriya, Dominic, Nikolas. I appreciated working with all of you, for both the technical and scientific support. Also, a big thank you to the rest of the ECTM colleagues, working inside and outside of the cleanroom, for the many coffees, lunches, and birthday cakes we shared. I am very grateful for all the students I had the pleasure to guide and to get support from: Ishaan, Bruno, Suzanne and Sudiksh. I learned a lot from each one of you, I think that you teached me care and patience and this is a great life lesson.

I would like to thank all the people from the 3me department and Kavli who could help me exploring other facilities and machines, your help was priceless throughout this long journey of PhD, in particular, thank you Wan, Sadeh, Peter, Prof. Caneva, Charles and Gideon. Nele, thank you very much for the time we spent together. Unfortunately, we just spend about a year together. You are a young woman, full of life and energy and it was a real pleasure to be a teammate for a while. I really enjoyed our drives to Belgium, I want to thank you for dropping me in Noorderkempen so many times, it was so kind of you. Roberto, Ernesto, Shin, Marco, and Michele thank you for the friendship that we build and the moment we spent together in the Netherlands it makes beautiful memories. I would also like to thank the Bioelectronics group, for all the good times we spent together: Ronaldo, Nasim, Gandhi, Cesc, and the Berlin part: Andra, Konstantina, and Raphael. Thank you all for the great times in Delft, Berlin, and Tirol!

Merci beaucoup à mes nouveaux collègues du CEA et tout particulièrement à Joris, merci d'avoir fait la traduction de mon résumé.

Andres, thank you very much for the kind help from the very beginning. You have been an amazing mentor and I am sure that I would have not been able to start or finish my PhD without you. You were always available to guide me through the secrets of the IPMC, electronics, articles, and of course writing. I enjoyed very much

the science I was doing thanks to you. I really appreciated your professionalism, time, guidance, care, and support during the past years. I am sure you will be a great supervisor for future PhDs and I wish you all the best for the future!

I also would like to thank all the crazy NOCI people and the beautiful moments we spent together, in addition to the very interesting talks that we shared I think that the thing I enjoyed the most was the cheerful and supportive moments we spent together. The NOCI retreats were much-needed time made of joy, monkey shots, and happy moments. I want to thank you all for these beautiful memories.

Bjorn, thank you for being my dear office mate and postdoc-engineer-wizard in chief! It was a real pleasure to work with you and to share talks, experiences, knowledge and tips about everything going from coding to manufacturing until politics and travelling. I think that you are an very smart and skilled scientist, I learned so much from you! Thank you for putting me back on track and save me huge amounts of time with your precious guidance in addition of being a great office mate showing everyday support.

Augustin, Arthur, Alex merci beaucoup à vous trois, le gang des papas, merci de me remettre les idées en place de temps en temps et de toujours me faire marrer, la semaine au US avec Arthur et Augustin était juste top, un super souvenir de fin de thèse. Merci à toi Augustin pour ton amitié, je pense que tu es vraiment une belle personne et je suis très heureux de faire parti de tes amis. Merci à mes potes de sarthe, le gang du terre-terre, Laura Tom Ronan Sammy Romane Clém et Damien, vous êtes la base vers qui je reviens toujours, on a une amitié tellement ancienne, je suis vraiment reconnaissant de votre soutien inconditionelle à travers les années. Chachou, merci d'avoir été un super soutient et merci de ton honnêté et ton amitié sans faille ! Merci au gang des copains avec qui on a organisé de super week-ends en France et ailleurs ! Merci à mes potes de Grenoble, Tibault, Christophe, Julie Aleks et Melissa !

Yves, Meriem, ma chère "safe zone", je suis sincerement heureux de m'être reconnecter à vous au cours des derniers mois, je crois que c'est un très bel accomplissement de fin de thèse. J'aime beaucoup notre relation et vous m'êtes très chers. Yves, je te remercie de ton soutien indéfectible, de ta douceur et de ta patience, et evidemment de ta présence dans les moments difficiles, je crois sincérement que les plus belles personnalités se révèlent dans ces moments là, j'ai beaucoup aimé le temps qu'on a passé que tout les 2 et j'espère que l'on continuera à le faire. Mémé, je te remercie d'avoir fait un retour fracassant dans ma vie, je pense qu'on a un lien particulier, qu'on se comprend assez bien l'un l'autre, je pense que tu as une très belle personnalité, je suis vraiment heureux du magnifique voyage que l'on a fait ensemble en Israel et en Jordanie et des "deep talks" qu'on a eu. J'espère qu'on pourra continuer ces aventures ensemble dans le futur!

Dhanesh, thank you for being my super precious support during the past years. I enjoyed my PhD so much thanks to you, I think that we both had fun trying weird stuff with IPMC, hydrogel, photoresist, cells, weird chemicals crazy machines, and so on. I really think that you deeply help me to go through this PhD not only through technical help but more importantly through friendship. I am really sorry that I was a bit short in time in the end, I wish we could have spent more time

working together in a peaceful and stress-free environment. I think that you can make beautiful articles of the things we tried together (you should publish this super cool engineered hydrogel sheet with an antifouling layer!). I think that you have a beautiful personality with a very trustful, honest and kind nature, you are so willing to help people! I am glad and honored that you decided to be part of my PhD and to choose to work with me on those crazy ideas. I wish you the best for the future, you are a super smart scientist (or engineer doing biology.... ?) and I am sure that you will continue to enjoy doing bold projects and helping people.

Leandro, je vais écrire en français, parce que j'ai la chance d'avoir un ami argentin à qui je peux parler dans ma langue maternelle. Merci du fond du coeur pour tout, je pense qu'on a construit une relation forte, tu m'as enormément aidé pendant ma thèse, evidemment d'un point de vue académique mais aussi et surtout en me prenant sous ton aile. Je crois que tu es l'une des plus belles rencontre que j'ai eu la chance de faire au cours des dernières années et je suis heureux que nos chemins se soient croisés. J'ai enormément apprecié le temps qu'on a passé ensemble, les longues soirées à refaire le monde avec du campari ou du fernet, je pense qu'on a un lien profond et qu'on partage une certaine vision du monde et de la vie. Evidemment notre voyage aux Etats Unis restera toujours comme un des plus beaux souvenirs ensemble. Merci aussi evidemment à Léa et Roxanne, à nous quatre on a formé un petit noyau dur pendant ces dernières années, on faisait presque partie de la même famille, je sais que ça vous rend triste que je quitte Delft et nos petites habitudes du mardi soir, mais comme tu le sais, la vida es una milonga y hay que saberla bailar! Je suis sûr qu'on se reverra très vite pour de longues soirées à refaire le monde!

Kelly, je te remercie tellement d'avoir été là depuis le tout début et jusqu'a la fin, tu as été un soutien, un pillier et un point d'ancrage essentiel pendant tout ce temps, j'ai beaucoup aimé faire cette aventure ensemble aux Pays Bas avec toi, je crois que j'ai eu beaucoup de chance de t'avoir pendant tout ce temps. J'ai beaucoup aimé passer tout ce temps ensemble et être là l'un pour l'autre, je crois que je me souviendrais toujours de la semaine qu'on a passé ensemble dans mon appartemant quand il y avait de la neige, c'était tellement gezellig! On a passé tellement de soirées ensemble à Delft ou à Utrecht à se soutenir pendant nos thèses respectives, ça a été un réel plaisir de te voir évouler au cours des dernières années et d'avoir été le témoin privilégié de cette évolution. Avec Simon on a formé un petit noyau à Bruxelles, je vous vous remercie sincèrement pour tout le soutien que vous avez montré pendant ces années. Je sais bien qu'on pourra plus se voir autant qu'avant et cela me rend quelque peu triste, mais je sais qu'on continuera à se voir, quoi qu'il arrive.

Of course, I would like to thank my dear paranymphs, Hande, thank you for being part of this adventure, I am really glad being by your side during the past years, as for Milica I am happy that life push our respective paths to meet each other. I think that you have a very kind and sweet personality, and you really take care of others, I really appreciated this attentive part of you during the past years. I really enjoyed coming back from wild parties in the Hague on this awful night bus together with you. Every time on the way back to Papenstraat I even didn't need

to talk and you could still understand me. I think that you are a very strong person with a very careful, selfless and magnanimous nature. I want to thank you also for being so honest with me and reminding me how lucky and privileged I am, I think that this is the best lesson I learned during this PhD. Milica, thank you for always standing next to me and helping me despite all the misery we went through. I think that we learned a lot from each other during the past years and I really appreciated this journey along your side (Perhaps I learned more from you than you from me, you are so wise, caring, and smart...). As I already told you, I came for sciences but I stay for the people and you are definitely one of those involved. I really appreciated our long talks about many different topics, I love the way you look at things and I think that I deeply share the same vision of the world with you. I wish you happiness and the best for the future. I am certain that you will find your path, whatever happens, you have this strength and energy in you. After this beautiful trip to Serbia and weekends let's organize some trips to Africa in the coming months so you could see girafe, you know that I am always into those kinds of adventures. The last word will be in your mother tongue: Заиста волим да проводим време са тобом. Прича коју заједно почињемо да градимо је заиста лепа и једва чекам да видим шта следи.

Finalement j'aimerais remercier mes parents sans qui cette aventure n'aurait pas été possible, vous m'avez toujours soutenu dans mes choix et dans les moments difficiles je vous remercie sincèrement pour tout ce que vous m'apportez.

List of Publications

Journal Papers

1. **P. Motreuil Ragot**, A. Hunt, L. N. Sacco, P. M. Sarro and M. Mastrangeli "Manufacturing thin ionic polymer metal composite for sensing at the microscale", *Smart materials and structures*, 32, 3, IOP publishing (2023).

2. **P. Motreuil Ragot,** D. Kasi, B. de Wagenaar, A. Hunt, V. Orlova, A. van den Maagdenberg, P. M. Sarro and M. Mastrangeli, "Ionic polymer metal composites (IPMC) based 3D printed micropump for Organ-on-chips", in preparation *Lab on chip*, RSC publishing (2023).

3. D. Nahon*, R. Moerkens*, H. Aydogmus**, B. Lendemeijer**, A. Martinez-Silgado**, J.M. Stein**, M. Dostanić, J.P. Frimat, C. Gontan, M. de Graaf, M. Hu, D. Kasi, L.S. Koch, K. Le, S. Lim, H. Middelkamp, J. Mooiweer, **P. Motreuil-Ragot**, E. Niggl, C. Pleguezuelos, J. Puschhof, N. Revyn, J.M. Rivera-Arbelaez, J. Slager, L.M. Windt, M. Zakharova, B.J. van Meer, V. Orlova, F. de Vrij, S. WIthoff, M. Mastrangeli, A.D. van der Meer, C.L. Mummery, *Taking microphysiological systems to the next level: Why quantification of physiological features is essential*, Submitted to Nature Biomedical Engineering.

4. D. Kasi, M. De Graaf, **P. Motreuil Ragot,** , J.P M. S. Frimat, M. D. Ferrari, P. M. Sarro, M. Mastrangeli, A. M. J. M. van den Maagdenberg, C. L. Mummery and V. V. Orlova, "Rapid Prototyping of Organ-on-a-Chip Devices Using Maskless Photolithography", *Micromachines 2022, 13, 49*

Conference Papers

1. **P. Motreuil Ragot,** G. Turcan, B. de Wagenaar, A. Hunt, P. M. Sarro and M. Mastrangeli "Ionic polymer metal composites-based microfluidics flow sensor for bio-MEMS applications" in *Proceedings of the 2022 IEEE Sensors conference, 30 Oct-2 Nov 2022, Dallas, USA*..

2. **P. Motreuil Ragot,** A. Hunt, L. N. Sacco, P. M. Sarro and M. Mastrangeli "Analysis of Platinum Distribution within a Nafion 212 Membrane during Electroless Deposition " in *Electrochemical Society Meeting Abstracts 242 (No. 23, pp. 986-986), 9-13 October 2022, Atlanta, USA.*

3. M. Mastrangeli, H. Aydogmus, M. Dostanic, **P. Motreuil Ragot,** N. Revyn, B. de Wagenaar, R. Dekker, and P. M. Sarro. "Microelectronmechanical Organs-on-Chip". *Proceeedings of the 21st Int. Conf. on Solid-State Sensors, Actuators and Microsystems (Transducers 2021), online, 20-25 June, 2021.*

4. **P. Motreuil Ragot,** A. Hunt, D. Kasi, B. Brajon, A. van den Maagdenberg, V. Orlova, M. Mastrangeli and P. M. Sarro. "Enabling actuation and sensing in Organ-on-chip using electroactive polymer". *Proceedings of the 3rd Int. Conf. on Soft Robotics (Robosoft 2020), May 2020, Yale, USA.*

Conference Presentations and Posters

1. **P. Motreuil Ragot,** D. Kasi, B. de Wagenaar, A. Hunt, V. Orlova, A. van den Maagdenberg, P. M. Sarro and M. Mastrangeli. "Ionic polymer metal composite (IPMC)-based micropump for organs-on-chip " in *EurOoCs, European society on organ on chips, Grenoble, France, 4-5 July 2022*.

2. **P. Motreuil Ragot,** D. Kasi, A. Hunt, A. van den Maagdenberg, V. Orlova, P. M. Sarro, M. Mastrangeli "Ionic electroactive polymer for Organ-on-Chip applications" In: *BIOEL, International Winterschool on Bioelectronics, Kirchberg in tirol, Austria, 12-19 March 2022*..

3. **P. Motreuil Ragot,** A. Hunt, D. Kasi, B. Brajon, A. van den Maagdenberg, V. Orlova, M. Mastrangeli and P. M. Sarro. "Enabling actuation and sensing in Organ-on-chip using electroactive polymer",In International MicroNanoConference, Utrecht (NL), December 10-11, 2019.